Fall 11-18-2016

Measurement and Analysis of III-V & II-VI Infrared Detectors: Radiometric, Noise Spectrum, and Radiation Tolerance Performance

Vincent M. Cowan

Follow this and additional works at: https://digitalrepository.unm.edu/nsms_etds

Part of the Electrical and Electronics Commons, Electronic Devices and Semiconductor Manufacturing Commons, Nanoscience and Nanotechnology Commons, and the Nuclear Engineering Commons

<u>   Vincent M. Cowan   </u>

Candidate

<u>   Nanoscience & Microsystems   </u>

Department

This dissertation is approved, and it is acceptable in quality and form for publication:

Approved by the Dissertation Committee:

<u> Prof. Sanjay Krishna   , Chairperson   </u>

<u> Prof. Ganesh Balakrishnan   </u>

<u> Prof. Danhong Huang   </u>

<u> Dr. John Hubbs   </u>

<u>   </u>

<u>   </u>

<u>   </u>

<u>   </u>

Measurement and Analysis of III-V & II-VI Infrared Detectors: Radiometric, Noise Spectrum, and Radiation Tolerance Performance

by

VINCENT M. COWAN

B.S., OREGON INSTITUTE OF TECHNOLOGY, 2006
M.S., UNIVERSITY OF DAYTON, 2008

COMMITTEE CHAIR: PROF. SANJAY KRISHNA

DISSERTATION

Submitted in Partial Fulfillment of the
Requirements for the Degree of

DOCTOR OF PHILOSOPHY
NANOSCIENCE & MICROSYSTEMS

The University of New Mexico
Albuquerque, New Mexico

December 2016

Acknowledgments

I would like to thank my advisors, mentors, and colleagues at the Air Force Research Laboratory. Specifically I would like to thank Dr. Chris Morath and Dr. John Hubbs. The countless weekends and late night evenings we have spent together at radiation sources over the years has provided immense insights into visible through long-wave infrared detector technology and the underlying semiconductor physics present in clear and radiation environments. Likewise I would like to thank the entire Infrared Radiation Effects Laboratory team and members of Advanced E/O Space Sensors group past and present. I would like to thank Prof Sanjay Krishna for the flexibility in this research and helping to define a research project that was of academic interest to the University of New Mexico and applicable to the technology needs of the United States Air Force. Finally I would like to thank my parents for believing in me and promoting science and engineering from a young age. I am forever grateful for the assistance of all those mentioned above and those that I have failed to include. Without all of these individuals support over the years this contribution to science and associated technology advancement would never been accomplished.

Measurement and Analysis of III-V & II-VI Infrared Detectors: Radiometric, Noise Spectrum, and Radiation Tolerance Performance

by

Vincent M. Cowan

Master of Science, University of Dayton,

Dayton, Ohio, 2008

Doctor of Philosophy, Nanoscience & Microsystems, University of New Mexico,

Albuquerque New Mexico, 2016

Abstract

Infrared (IR) hybrid detector arrays and discrete detectors operated in the space environment may be subjected to a variety of sources of natural radiation while in orbit. This means IR detectors intended for applications such as space-based intelligence, surveillance, and reconnaissance (ISR) or space-situational awareness (SSA) must not only have high performance (high quantum efficiency, η and low dark-current density, J_D, and preferably minimal 1/f noise content), but also their *radiation tolerance* or ability to withstand the effects of the radiation they would expect to encounter in space must be characterized and well understood. As the effects of proton interactions with hybrid detector arrays can dominate in space, a specific detector's radiation tolerance is typically

characterized by measuring its performance degradation as a function of proton fluence, Φ_P, up to a total ionizing dose (TID) of typically 100 krad(Si), which is 3-5 times the maximum expected on-orbit TID value for typical space-based E/O applications. Now for other applications such as astronomy, planetary science, and imaging associated with nuclear medicine applications, the TID requirement can be much higher. When comparing the performance of novel IR detector technologies, it has also proven valuable to determine the rate of performance degradation induced by radiation, referred to as a damage factor. It has also proven valuable to perform temperature-dependent measurements of J_D, which are used to determine the dark current limiting mechanism via an Arrhenius-analysis, and the degree to which any thermal annealing of the irradiation induced defects may occur have provided unique insights. Finally, given the potential sensor/system impact it is of the upmost importance to understand the frequency dependent contributions to the overall noise in IR detectors. This body of work contains in-depth measurements and analysis of these performance metrics for both III-V- and II-VI-based IR detectors of various detector architectures.

In this dissertation, the results of IR III-V-based InAs/GaSb and InAs/InAsSb type-II strained layer superlattice (T2SLS) and bulk detectors that employ unipolar barriers in their detector architecture and II-VI-based HgCdTe IR detectors are characterized in both clear and radiation environments. III-V-based IR detectors that employ unipolar barriers are now being considered for space applications due to their relative advantage in manufacturability as compared with conventional HgCdTe IR detectors that dominant space-based IR E/O imaging. T2SLS detectors are theoretically predicted to have lower Auger-limited dark currents compared with HgCdTe. However, this advantage is yet to be

realized due to the lack of reliable passivation schemes and higher bulk defect densities in these materials, which lead to surface- and Shockley-Read-Hall (SRH)-limited dark currents, respectively. Unipolar-barrier architecture detectors, including the nBn, pBp, pBiBn, etc. detectors reported on here, have been introduced in an effort to mitigate these dark current limiting mechanisms. By deliberate choices of the absorber materials and device structure, the potential barriers in these detectors appear only in either the conduction or valence band to block the majority-carrier bulk and surface currents (e.g. in a nBn detector the potential barrier appears only in the conduction band). This results in an elegant detector architecture in which the ideal barrier layer limits the depletion by an external bias to itself so that the absorbing layer remains in the flatband condition, which eliminates Generation Recombination currents due to SRH defects that may be present in the absorbing layer that ultimately limit the diffusion length.

Subjecting IR detectors to proton irradiation may lead to both TID and displacement damage effects, both of which occur on orbit. TID effects occur as incoming protons lose their kinetic energy to ionization of the detector material's constituent atoms and the additional charges become trapped in oxide layers or surface traps. This additional charging may result in flat-band voltage shifts and increased surface leakage currents. TID effects generally are more visible at lower device temperatures, where charges generated in oxide layers are less mobile, and tend to anneal out at higher temperatures. Displacement damage effects result from the occasional non-ionizing energy loss of an incoming proton due to elastic or inelastic scattering with an atomic nucleus that is sufficient to knock the atom from its lattice site and generate vacancy-interstitial pairs, anti-sites, and defect complexes. In this work these defects were shown to manifest in lower η, due to the

consequent reduction in minority carrier lifetime τ, and higher J_D, due to the SRH mechanism. The proton fluence required to alter the background doping levels, such that the fundamental Auger mechanism is enhanced, when using protons with an energy of 63 MeV is expected to be order's of magnitude higher than the fluence levels used in this work. Thus, a vital step to characterizing a detector's radiation tolerance is measuring η and J_D as a function of Φ_P, with all irradiation and measurements conducted in-situ stepwise at the detector's expected operating temperature and bias. In this research, it was found that rate of degradation in quantum efficiency when irradiated with 63 MeV protons for a family of Sb-based MWIR detectors that employed unipolar barrier architectures was greater than 3 times that of conventional p-on-n HgCdTe photodiodes with similar cut-off wavelengths. Likewise, it was found that the rate of degradation in the lateral optical collection length for these same devices was greater than 20 times that of the equivalent MWIR HgCdTe photodiodes. This has been attributed to a degradation in minority carrier lifetime leading to a reduction in the diffusion length. This body of research provides unique insights into the radiation susceptibility and fundamental mechanisms taking place that directly contribute to performance degradation of III-V- and II-V-based IR detectors of various detector architectures.

Contents

List of Figures

List of Tables

1 Introduction

Photons are emitted from all matter with a temperature above absolute zero. Planck's law in Equation 1.1 dictates the spectra as

$$L_q = \frac{2\pi c}{\lambda^4} \frac{1}{e^{\frac{hc}{\lambda k_B T}} - 1} \left(\frac{photons}{s\,m^2\,m} \right),$$ 1.1

where L_q is the spectral radiance, λ is the wavelength of light, h is Planck's constant, c is the speed of light in vacuum, and k_B is Boltzmann's constant, T is temp. This function is plotted in Fig. 1.1 for blackbodies at several different temperatures. Notice from the traces in this figure that a majority of the blackbody emission occurs in the infrared region of the spectrum, greater than 1 µm. All hot objects, including the universe itself, emit approximately like the ideal blackbody governed by Equation (1.1); and the degree to which they do so is described by the object's spectral emissivity $\varepsilon(\lambda)$ function. This makes detection of IR light of fundamental importance for a variety of applications ranging all the way from mid-flight detection of inter-continental nuclear missiles to the simple homeowner attemps to eliminate heat leaks in window casements. [1, 2]

The IR region of the electromagnetic spectrum includes wavelengths ranging from 900 nm to 1 mm, of which there are several sub-bands. Roughly speaking, as their definitions vary across the communities that use IR, the IR sub-bands typically include the near-infrared (NIR) ranging from 700 nm to 1 µm, shortwave infrared (SWIR) ranging from 1 µm to 2.5µm, midwave infrared (MWIR) ranging from 3 µm to 5.2 µm, longwave infrared

(LWIR) ranging from 8 µm to 14 µm, very longwave infrared (VLWIR) ranging from 14 µm to 30 µm, and, finally, at yet even longer wavelengths the far-infrared (FIR) or terahertz (THz) covering the spectral range from 30 µm all the way up to 1 mm. Beyond this point is the microwave range of the electromagnetic spectrum. The majority of objects of interest for … have temperatures in the 200 – 1000 K range, which correspond to having peak radiance in the SWIR, MWIR, and LWIR bands as shown in Fig. 1.1. One of the distinct advantages of SWIR, MWIR, and LWIR bands is that obstructions present to prevent imaging objects of interest through the earth's atmosphere are limited. This is of particular interest to the astronomy community and a variety of military applications where imaging of the earth from space takes place. The work described in this dissertation focuses on detectors designed to absorb light in the MWIR regime, although the ideas discussed here apply to IR detectors designed for the other sub-bands as well. [3]
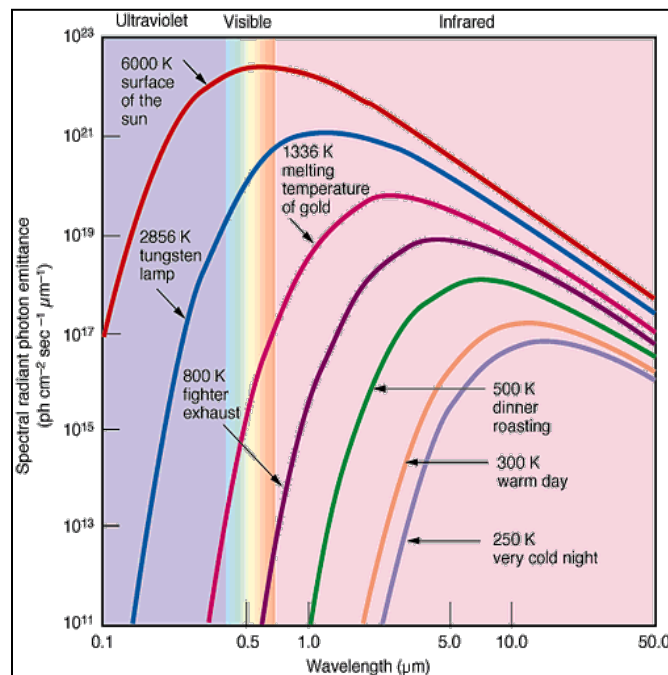
Fig. 1.1 : Spectral radiant photon emittance as a function of wavelength for different object temperatures. [4]

1.1   Infrared Detectors

In general there are two categories of infrared detectors, namely thermal detectors and photon detectors. Thermal detectors, including pyrometers, thermocouples, and bolometers, all operate on the same principle of detecting the integrated power of incident infrared radiation as 'heat' and thereby experiencing a change in temperature, which manifests in some fashion as the measured 'signal' (e.g. bolometer temperature change results in a change in electrical resistance). A thermal detector's response is proportional to the total power of the IR radiation it absorbs in watts, and its associated response time is dependent on its thermal time constant, which equals the product of its thermal capacity and thermal resistance. Typically these detectors are operated at room temperature and have a very wide absorption spectrum and a low cost point. The biggest detriment of this technology is thermal detectors typically exhibit very low sensitivity due their inherently high noise which places a large constraint on the application space for this technology. [1]

In comparison to thermal detectors, the fundamental physics of a photon detector are very different as the change in its electrical properties that results from the incident infrared radiation is a direct measure of the actual number of incoming photons that it is sensitive to, not the total incoming power. So photon detectors experience a single response element per incoming photon, while thermal detectors see the same response level from 1 W of UV photons as they see from 1 W of 10 μm photons. This is the fundamental distinction between thermal and photon detectors and why it is appropriate that they not share the same units (although this often done for historical reasons).

There are primarily two types of infrared semiconductor photon detectors in common use today, namely photoconductors and photodiodes. In the case of a photoconductor, the conductivity of the semiconductor is increased in the presence of optically generated carriers, and the output signal is generated by monitoring the conductance by external means. In the case of a photodiode, an additional current is generated when incoming photons are detected and this photo-current is measured by some external means. Both of these photon detectors are in part composed of a layer of semiconductor material where photons are absorbed creating electron-hole pairs. This layer of absorbing material typically has a direct bandgap where the bandgap energy, E_g, is equal to the smallest photon energy, $E = h\nu = {hc}/{\lambda}$, where $\nu = {c}/{\lambda}$ is the photon frequency, in the particular infrared band of interest (i.e. for photon energy in eV and λ in μm, the energy expression simplifies to $E[eV] = {1.24}/{\lambda[\mu m]}$). In this work, the minimum photon energy associated with the MWIR band, which is typically about 250 meV, or equivalently, it is $\lesssim$ 5 μm, is of interest.

There are two prominent material systems used for photon detectors in the IR, specifically semiconductor compounds formed from the combination of elements from the periodic table in Groups II and VI and in Groups III and V. The only II-VI material of interest for photon detectors is the ternary compound HgCdTe. The III-V materials of interest for photon detectors include InSb, InAs, InGaAs, and strained layer superlattice (SLS) InAs/(In)GaSb and other III-V variants.

There are several different types of photon detector architectures in common use today, the most popular still being the standard photodiode in which a p-n junction is formed with a

photon absorbing layer. One of the more popular IR materials and architectures for MWIR space applications is HgCdTe p-on-n photodiodes. A newer detector architecture, which contains semiconductor layers that form unipolar potential barriers and share attributes of both photoconductors and photodiodes, has recently become more popular and is increasing its performance with time. In these detectors, the barrier layer suppresses the majority carrier current while allowing the minority carriers to flow through unimpeded. An example of this architecture is the nBn detector, wherein *nBn* refers to the juxtaposition of the conduction-band (CB) barrier layer. *B.* that blocks the majority carrier electrons between an n-type top contact layer and an n-type absorbing layer. This standard nBn IR detector architecture is basically material systems agnostic, so both III-V and II-VI semiconductors have been used to fabricate them. In this work, we will be focusing on MWIR photodetectors, specifically, both bulk and SLS Sb-based nBn and alike barrier architecture detectors as well as HgCdTe photodiodes. [2, 3]

Infrared photodetectors being used for strategic applications have diverse design requirements placed on their performance parameters, such as the required sensitivity, operating temperature, physical size, absorption range, radiation hardness, and cost, depending upon the application. In low volume, high cost applications typical of strategic applications, where highly sensitive and extremely low noise detectors are required, HgCdTe-based (MCT) detectors are currently the dominant technology in the MWIR regime due to their high performance in all of the areas mentioned above. Small state-side manufacturing base, lack of availability of large format CdZnTe substrates, and cost are some of the critical problems associated with HgCdTe detectors, which makes research on detectors based on the III–V material system attractive. The III-V material system,

specifically Sb-based, is used for a relatively large technology portfolio including optical devices such as quantum cascade lasers where as in comparison the II-VI material system is only used for HgCdTe infrared detectors which from a technology sustainability perspective creates an extremely difficult problem.

1.2   Comparison between unipolar barrier detector architectures with conventional photodiodes

An nBn detector consists of two n-type regions separated by a barrier (B) located in the conduction band plus electrical contacts on either end as illustrated in Figure 1.2. [5, 6] Within the relatively wide n-type absorber region photons are absorbed. In order to tune the maximum wavelength that the nBn detector absorbs the bandgap is altered. Minority carrier holes diffuse in the valance band to the barrier region, where an electric field induced by the applied bias voltage sweeps the minority carrier past the barrier region. Unlike the photodiode, the nBn detector relies on this external bias to induce charge separation. Given research content that will be discussed in chapters to come in this dissertation, please note this device's dependence on diffusion. Once past the barrier the minority carriers flow and recombine in the n-type contact layer. The majority carriers (electrons) move in the opposite direction towards the highly doped n-type bottom contact layer which is a common back-plane to all of the nBn photodiodes in a detector array. The applied voltage is the offset of the Fermi level and labeled as E_F in the diagram. The top contact of the device is tied low so that holes are attracted to it.

A great deal of engineering goes into the barrier used in nBn and alike unipolar barrier architecture devices. The purpose of the barrier in an nBn is simple, namely block the flow

of electrons. That said it must have sufficient thermal energy (kT) to block thermally

induced electrons and be thick enough to prevent tunneling. It has been found that barriers

with thicknesses greater than 100 nm are sufficient to accomplish this. It is imperative that

the entire field is applied only across the barrier region, which in turns requires the barrier

to be minimally doped. The barrier ends up occupying the entire depletion region. It is of

the upmost importance that the barrier doesn't extend into the valence band otherwise a

reduction in the hole current could result which interrupts the photo-signal.
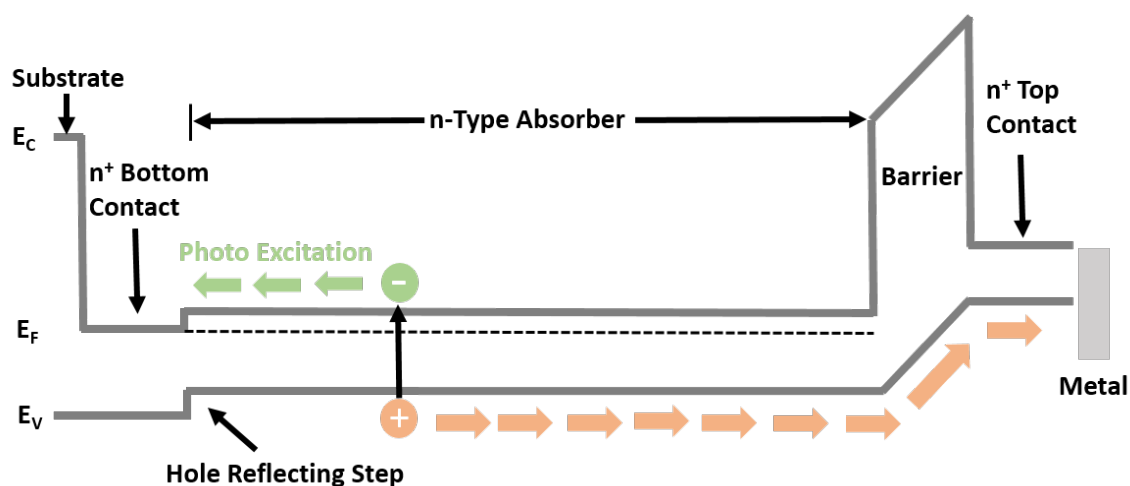
Fig. 1.2: Band diagram of the nBn unipolar barrier detector architecture. The barrier blocks the flow of majority electrons while allowing minority holes to flow through unimpeded to the opposite contact.

A great deal of engineering and optimization gone into barrier designs but, the bottom

contact layer is more complicated than what one may realize. It is of the upmost

importance that the bottom contact layer is highly doped for low resistivity to ensure that

the electrons flow unimpeded from all of the pixels in the detector array. The bandgap of

the bottom contact layer is wider than that of the absorber such that a hole-reflecting step

is created in the valence band. As a result, holes view the area between the absorber and the bottom contact layer as a plane of zero surface recombination velocity and are not generated or consumed there.

Within a conventional MWIR photodiode operated in reverse bias there are three main sources of noise that are of concern. The first being diffusion current of minority carriers diffusing toward the junction and being swept across the depletion region to the other contact. The second being the Shockley-Read-Hall generation current that results from the presence of defects in the depletion region within the p-n junction. And the third contributing noise source being the current that is originating from defects at the surfaces and interfaces in the junction. One of the foreseen advantages of nBn and alike unipolar barrier architecture detectors in comparison to a standard p-n junction is the nature of the device and inherent use of a barrier is it essentially eliminates the Shockley-Read-Hall generation current in the depletion region. Likewise the barrier prevents or greatly suppresses the majority carrier electrons from reaching the top contact layer. The generation recombination current is suppressed and the surface current is blocked.

1.3 Motivation and Approach

Although T2SLS and bulk-based nBn and alike unipolar barrier IR detectors have theoretically been shown to have superior dark current performance over that of conventional HgCdTe IR photodiodes, the reality is that their dark current densities and quantum efficiencies are not at the level required to displace the incumbent technology. [7-10] HgCdTe IR detectors exhibit extremely high spectral quantum efficiencies and dark current densities at present date three orders of magnitude lower than that of Sb based nBn

and alike IR detectors. For photon starved applications, this performance is often a hard requirement. Furthermore, for strategic applications such as space based imaging where natural and man-made radiation are a concern, up until this body of work had been conducted very little was understood on their radiation susceptibilities. This body of work was aimed at thoroughly characterizing the III-V based nBn and unipolar barrier detector family's performance when subjected to both gamma irradiation and displacement damage induced by protons. This includes exhaustive characterization of unipolar barrier detectors of various cut-off wavelengths in clear environments, to include dark current density as a function of perimeter (P) to area (A) ratios, quantum efficiency (QE), lateral optical collection length (L_d), and noise currents as a function of frequency. All of which were characterized in-situ stepwise at radiation sources reflective of natural space providing unique insights on the degradation mechanisms present and overarching performance of the technology when compared to the incumbent, namely HgCdTe. The approach for this research can be divided into two distinct paths as shown in Figure 1.3. Both of these paths marry at the end when aggregate rates of radiation induced performance degradation are compared across material systems and detector architectures. Within Figure 1.3, all of the research that is colored in green was conducted and reported on for the first time as a result of this body of research.
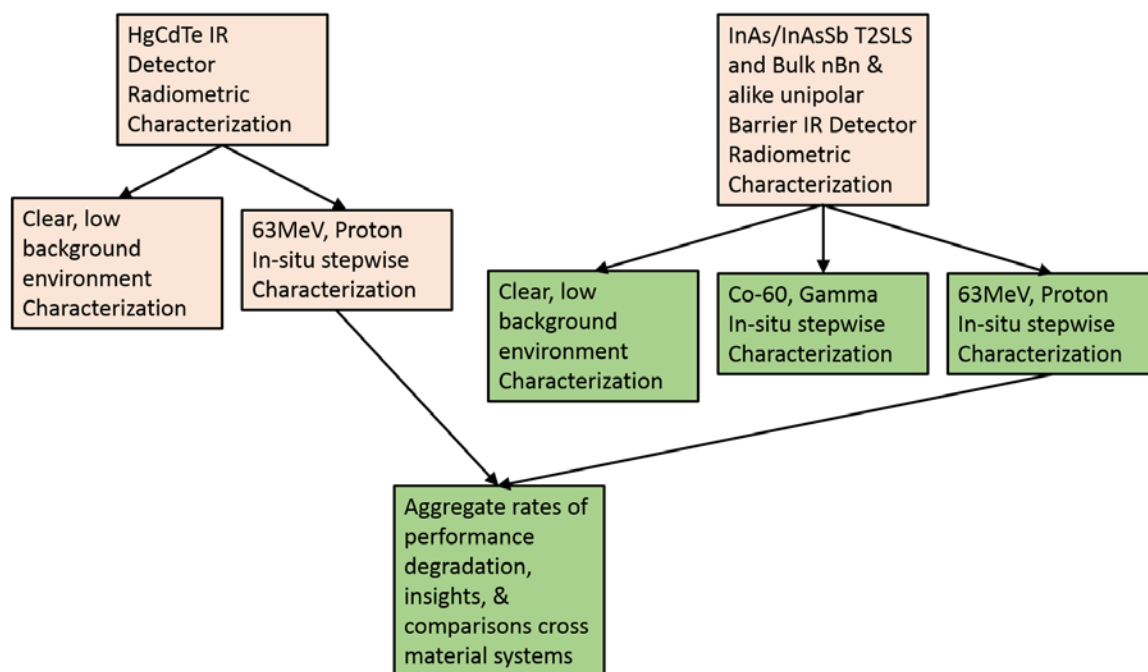
Fig. 1.3: Research approach and novel research results brought to the table as a result of this body of research being conducted (green boxes).

This dissertation is based on a significant amount of research that has been both peer-reviewed and published as well as presented at multiple conferences in this field of study, including three invited conference presentations that I provided. This research to date has resulted in the following publications listed in Table 1.1 including the first ever refereed publication on the proton induced radiation degradation of a unipolar barrier infrared detector that utilized a T2SLS absorber and the first ever aggregate analysis of the radiation induced performance degradation of III-V based unipolar detectors as a function of wavelength. [11-13] A total of 12 refereed publications and 28 conference proceedings have resulted from this work as shown in Table 1.1.

Carrier lifetime vs proton irradiation of III-V & II-VI based MWIR space detectors	MSS	11/2016
More accurate quantum efficiency damage factor for proton-irradiated, III-V-based unipolar barrier infrared detectors	IEEE TNS	11/2016
HOT MWIR Interband Cascade Detectors Based on Strained Layer Superlattices	QSIP	7/2016
MWIR pBn unipolar barrier photodetectors based on strained layer superlattices	QSIP	7/2016
Radiation effects on Yb:YLF crystals using cryogenic optical refrigerators	SPIE	9/2015

Proton irradiation of MWIR HgCdTe/CdZnTe	SPIE	9/2015
MWIR unipolar barrier photodetectors based on strained layer superlattices	SPIE	9/2015
Low-frequency, noise spectrum measurements of mid-wave infrared nBn detectors with superlattice absorbers	SPIE	9/2015
Empirical trends of minority carrier recombination lifetime vs proton radiation for rad-hard IR detector materials	SPIE	9/2015
Microscopic model for studying radiation degradation of electron transport and photodetection devices	SPIE	9/2015
Proton-irradiated InAs/GaSb T2SLS materials for space-based infrared detectors using magnetoresistance measurements	SPIE	9/2015
High-operating temperature MWIR unipolar barrier photodetectors based on strained layer superlattices	SPIE	6/2015
Diffusion current characteristics of defect-limited nBn mid-wave infrared detectors	APL	4/2015
Multi-timescale microscopic theory for radiation degradation of electronic and optoelectronic devices	AJSS	4/2015
Proton irradiation effects on the performance of III-V-based, unipolar barrier infrared detectors	IEEE TNS	12/2014
Comparison of the proton radiation response of a MWIR HgCdTe focal plane array to an III-V nBn MWIR focal plane array	MSS	10/2014
Mid and long wavelength infrared HgCdTe photodetectors exposed to proton radiation	SPIE	9/2014
Effect of defects on III-V MWIR nBn detector performance	SPIE	9/2014
High operating temperature midwave Infrared (MWIR) photodetectors based on T2SLS InAs/GaSb	SPIE	9/2014
In-situ minority carrier recombination lifetime measurements at radiation sources for rad-hard IR detector materials	SPIE	9/2014
Gallium-free type-II InAs/InAsSb mid-wave infrared superlattice photodetectors	II-VI	9/2013
Defect related dark currents of nBn and pn detectors	II-VI	9/2013
Noise spectrum measurements of interband cascade IR photodetector w/ 33 nm wide electron barrier	SPIE	9/2013
Two color high operating temperature HgCdTe photodetectors grown by MBE on silicon substates	SPIE	9/2013
Proton radiation effects on the photoluminescence of infrared InAs/InAsSb superlattices	SPIE	9/2013
Radiation tolerance of type-II strained layer superlattice based interband cascade infrared photodetectors	SPIE	9/2013
Radiation tolerance characterization of dual band InAs/GaSb T2SLS pBp detectors using 63 MeV Protons	APL	12/2012
InAs/GaSb-based nBn MWIR detector noise measurements	II-VI	11/2012
Proton radiation characterization of MWIR HgCdTe p-on-n photodiodes grown via LPE & MBE	MSS	10/2012
Photoconductive gain in barrier heterostructure infrared detectors	SPIE	5/2012
Radiation tolerance of a dual-band IR detector based on a pBp architecture	SPIE	5/2012
Radiometric characterization of a MWIR Type II SLS FPA from Teledyne Imaging Systems STEPS program	MSS	3/2012
Proton fluence characterization of TIS large format focal plane arrays from the High Stare Program	MSS	3/2012
I-V and differential conduction characteristics of AlGaAs/GaAs lateral quantum dot IR photodetector	II-VI	10/2011
Comparison of superlattice based dual color nBn and pBp infrared detectors	SPIE	9/2011
Low temperature noise measurement of an InAs/GaSb-based nBn MWIR detector	SPIE	5/2011
Radiometric characterization of LWIR focal plane array developed by SELEX sensors	MSS	3/2011
Radiometric and radiation characterization of scanning time delay integrate (TDI) SWIR focal plane array	MSS	3/2011
Gamma-ray irradiation effects on InAs/GaSb-based nBn IR detector	SPIE	1/2011
Electrical & optical characterization of InAs/GaSb-based nBn IR detector	SPIE	8/2010
Infrared detectors for space applications	QSIP	8/2010

1.5   Outline of the Dissertation

The dissertation is organized into three major sections. The first section is 'Infrared Detectors', namely II-VI- and III-V-based infrared detectors and underlying detector

architectures. In Chapter 2, different methods that are employed to characterize the radiometric and radiation tolerance of infrared detectors are discussed. Specifically, an in-depth discussion of measurement methodologies associated with thoroughly characterizing an infrared detector's dark current, quantum efficiency, CV, and noise spectrum are discussed. This chapter also covers radiation sources that can and are utilized in this body of work to deliberately introduce both surface and internal defects in the crystalline lattice of the detector. These radiation sources are used to mimic what the detector material will experience when operating in the radiation environment of natural space.

Section II, including Chapters 3 and 4, focus on the characterization results. Chapter 3 presents results collected on HgCdTe diodes using the characterization methodologies outlined in Section I. Detailed discussion on the characterization of HgCdTe photodiodes of various wavelengths in both clear, gamma, and proton irradiation is included. In Chapter 4, a systematic study of radiation induced degradation of various unipolar barrier infrared detector designs utilizing both bulk and T2SLS absorbers with various cut-off wavelengths is discussed. Both Chapters 3 and 4 include a thorough discussion of annealing observed through controlled annealing experiments on II-VI- and III-V-based IR photodiodes.

Section III is focused on aggregate results. Chapter 6 introduces damage factor analysis across all devices characterized and trends within both the II-VI photodiodes and III-V-based unipolar barrier IR detector architectures. Experimental investigation of the nature of these performance degradation trends are discussed in detail in this chapter. Finally, Chapter 7 is devoted to discussions about conclusions from this work and identifying the key areas for future work, including recommendations on methods of engineering around the radiation induced performance degradation observed.

2. IR Detector Radiometric Performance and Radiation Tolerance Characterization Methodologies

This chapter will give an overview of the methods used to radiometrically characterize the performance and radiation tolerance of IR detectors. Radiometry is generally most often defined as the science of measuring light or the flow of radiant energy through space. Here, *radiometric performance characterization* refers to using radiometric techniques to accurately account for the amount of electromagnetic energy, in terms of amplitude and wavelength, emitted from a well-established IR source that becomes incident on an IR detector under test by using a simple geometry. In such circumstances, the detector's ability to respond electrically to incident optical energy can thus be established by measuring its electrical output under illumination and dividing that by the known radiant input. This response measurement along with a measurement of the detector's electrical output without any illumination, or its inherent noise level, are used to calculate detector sensitivity or the minimum amount of incident optical energy that produces a measurable detector output. Thus, response and noise are the main elements of detector performance. To characterize the radiation tolerance of the detector, the same radiometric performance characterization is done whilst, or directly after, the detector is exposed to a known amount of high energy

radiation (rays or particles), which may cause ionizing and non-ionizing damage to the detector.

The relationship between radiometric characterization of detector performance and irradiation is quite complicated and the importance of conducting this experimental work in this manner can't be stressed enough. Failure to complete characterization with respect to radiation exposure often results in irrelevant results not reflective of operation of an IR detector in a space or other environment in which radiation is present. For all of the characterization work in this dissertation the IR detectors were held at their operating temperatures the entire time they were being irradiated such that no thermal annealing would occur and systematically in a step-dose they were characterized from a radiometric perspective, irradiated while under detector bias, and once again characterized from a radiometric perspective. This cycle was repeated until the desired total ionizing dose or proton fluence was achieved. In this body of research significant effort was put into executing controlled annealing experiments to extract surface from bulk effects of performance degradation for the detectors under test. The top level experimental procedure is summarized in **Error! Reference source not found.** below. Each of the section identified below contain a sub-experimental effort to gather the desired data. In this work, we have sought significant improvements in all the five aspects (colored in peach in Figure 2.1) of the radiometric characterization, in order to improve the understanding and performance of nBn and alike unipolar barrier IR detectors for strategic applications. To the best of my knowledge this is the first time that in-situ stepwise radiometric characterization of unipolar barrier IR detectors as a function of gamma and proton irradiation has ever been completed and resulted in the first authorship of the Applied

Physics Letter in 2012. [11-13] Post 2012 significant research findings have been realized and published on this body of work by author and collaborators. In this chapter, the main aspects or radiometric characterization and radiation exposure will be briefly discussed.
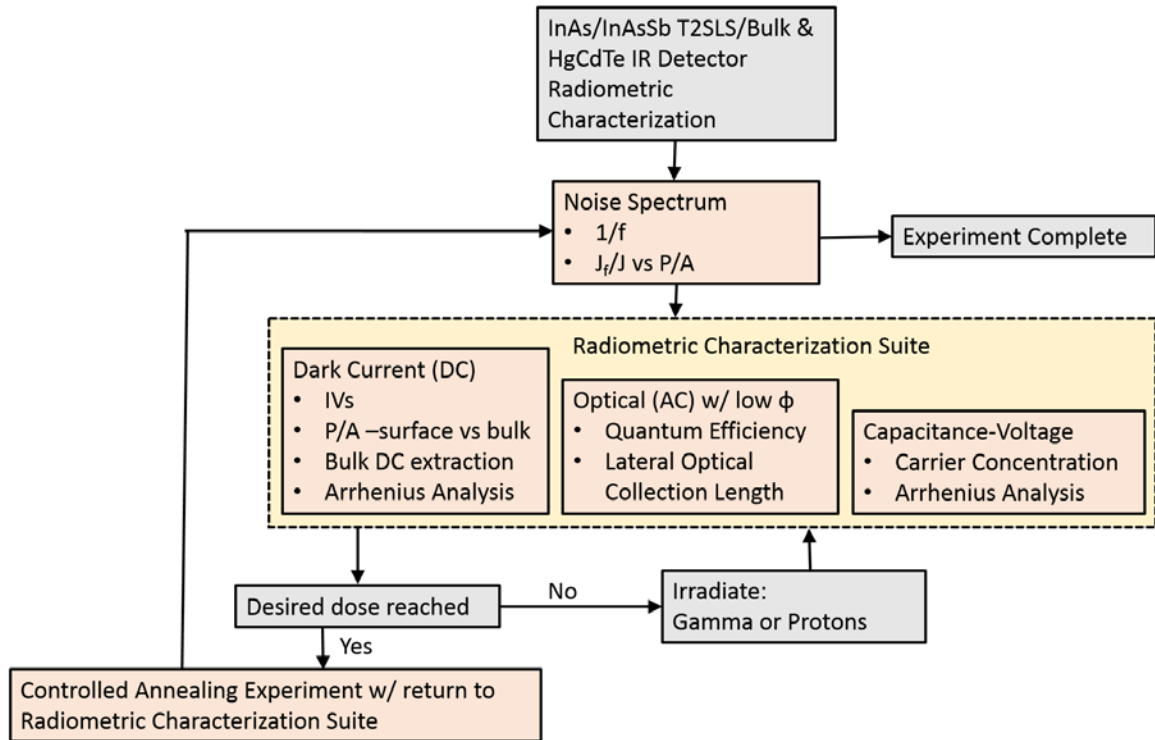
Fig. 2.1: IR detector radiometric and radiation tolerance characterization sub experimental efforts and sequence.

2.1 Radiometric Characterization

2.1.1 Dark-current

Dark-current measurements were then performed using dual standard dc source measurement units to verify that the current flowing into and out of the detector were equal such that no additional leakage paths were present. These measurements are taken with a 77 K shutter blocking light from entering the Dewar. The noise floor associated with this test system is on the order 10^{-12} Amps, which is a function of the phosphor bronze wire and

lengthy cables running between the detector under test and measurement system, which includes a low noise switch to provide characterization throughput. As it is typically more sensitive to irradiation, dark-current is always measured following the photo-current I_{photo} measurements when step-dosing the detector under test, to allow for any transient effects to fully diminish. Temperature-dependent measurements of the dark-current density J_D were performed from temperature T from 77 to 300 K at the detector's operating bias and an Arrhenius-analysis is performed to determine the dark-current activation energy E_A and thus, gain some insight regarding the dark-current limiting mechanism present in the detector under test.

Nearly always the detectors that were characterized in this body of work were processed such that they have variable area diodes that allow a large Perimeter (P) to Area (A) ratio space to be explored. The advantage of this is the type of analysis is that bulk and surface or lateral components of the dark-current and photo-current can be accounted for and most fundamentally comparted as a function of irradiation. It is very common to plot the dark-current density (J) at the detectors operating bias V_B which is determined by analyzing a plot of the detectors signal to noise ratio (SNR) specifically determining where the local maximum occurs which is deemed as V_B for the photodetector.
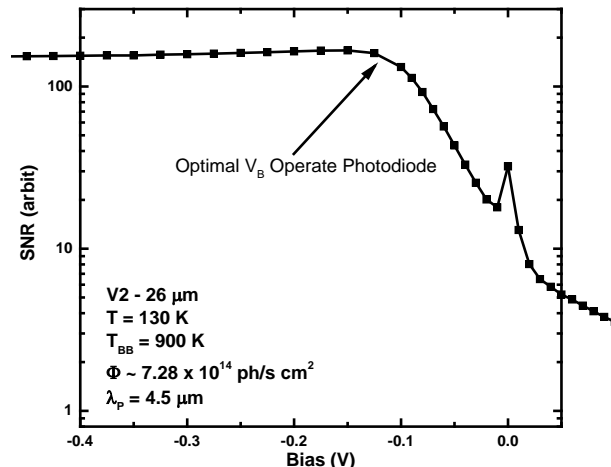
Fig. 2.2: Signal to noise ratio for typical variable area MWIR photodiode.

The dark-current density at this optimal point of operation is then plotted as function of irradiation such that one can track the degradation in detector performance. The slope of this increase in J as a function of irradiation is later defined as a damage factor which will be discussed later in this work in detail. It should be noted that that equation 2.1 doesn't account neglects random telegraph signal, 1/f, tunneling and other noise characteristics present.

$$SNR = \frac{I_{photo}}{\sqrt{J_{dark}}}$$
(2.1)

Significant effort was put in taking dark-current density measurements as a function of temperature such that an Arrhenius analysis could be performed such that the fundamental mechanisms in the novel nBn and alike unipolar barrier architecture detectors could be explored. Examples of this are looking at the diffusion limited, generation recombination, and in some cases trap assisted tunneling regimes of each photodiode. This includes

extracting activation energies and observing how the photodetector behavior changes when subjected to controlled annealing experiments post irradiation.

2.1.2 Optical measurements

Photo-current measurements were taken with the variable area detectors held at the operating bias as calculated in equation 2.1, where it is applied to the top of each mesa, using standard AC lock-in technique with a f/#~40 and a blackbody source. The blackbody output is passed through a room-temperature IR band-pass filter and a KRS5 Dewar window, followed by a 4mm pinhole held at 77 K within the dewar, leading to an incident photon flux which can be computed using equation 2.2 below. The radiometry for all of the characterization work was such that the limiting aperture was the cooled pinhole and large f#s such that low irradiance conditions could be created such that this work was reflective of strategic sensing needs. The characterization system that was constructed for this research was deliberately designed to be mobile such that it could transported to radiation sources around the country in which this research was conducted and is shown in Figure 2.3.
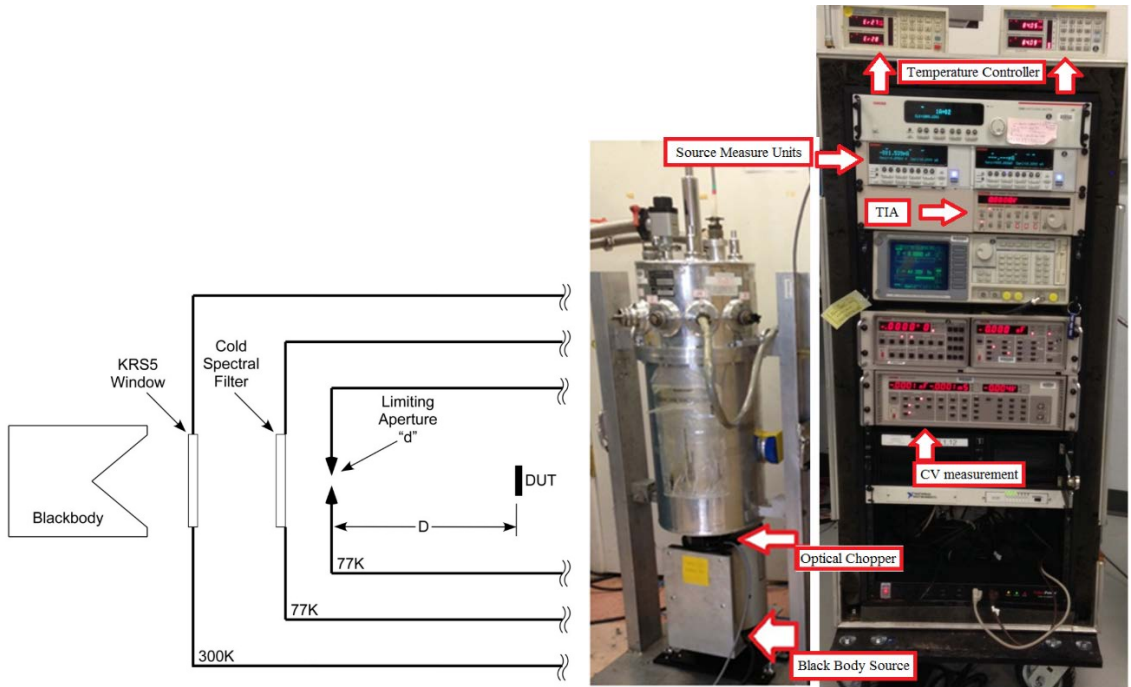
Fig. 2.3: (Left) Dewar radiometry, cooled pinhole is limiting aperture and f#~40. (Right) Mobile IR detector radiometric performance characterization system.

$$\tag{2.2}$$

For mesa detectors, the photo-current is given by:

$$I_{photo} = q\eta E_Q(L + 2L_{oc})^2 \tag{2.3}$$

where q is the charge of an electron, L is the drawn length an L_{oc} is the lateral optical collection length of the messa of the photodetector. By plotting $\sqrt{I_{photo}}$ as a function of L and applying a weighted, least squares linear fit the fitting's slope parameter m can be determined and used to was then used to determine the quantum efficiency η according to the expression:

$$\eta = {m^2}/{qE_q} \tag{2.4}$$

From this same weighted least squares linear fit the Lateral optical collection (L$_{oc}$) can be determined which corresponds to the intercept on the Y-axis. Both η and L$_D$ are plotted as a function of irradiation, once again when one performs and empirical fit of these data's a damage factor can and is determined. This will be discussed in detail later. Figure 2.4 shows a typical plot of photo-current as a function of mess size of the variable area photodetectors along with quantities described that were extracted.
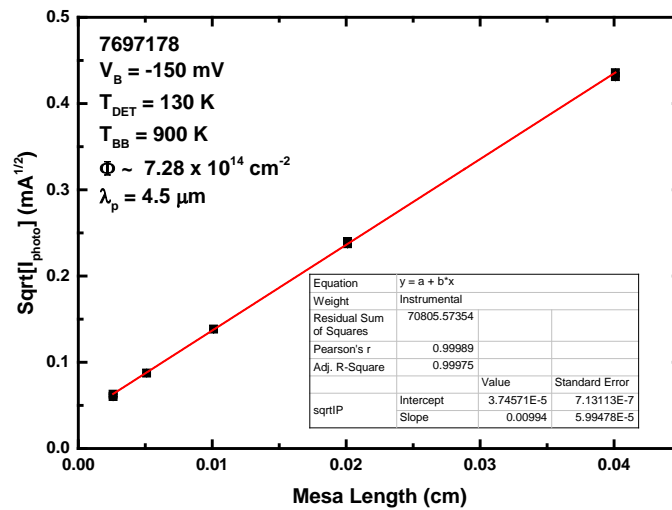
Fig. 2.4: Photo-current plotted as a function of mesa length, in which through modeled fit η and Loc are determined.

For select characterizations included in this manuscript where variable area diodes were not available instead of using quantum efficiency peak responsivity was used

$$R_{peack} = \frac{I_{photo}}{MFxA_D x\left(\dfrac{\Omega}{\pi}\right) x \displaystyle\int_{\lambda_1}^{\lambda_2} R^1(\lambda)\left[M_b(\lambda T_{BB}) - M_c(\lambda T_Q)\right]T_W(\lambda)T_f(\lambda)d\lambda} \quad (2.5)$$

where I_{ph} is the current measured through the detector, MF is the modulation factor of the optical chopper, A_D is the area of the detector, Ω is the projected solid angle of incident

radiation on the detector, R^l is the relative spectral response, M_b is the spectral exitance of the black body source, M_c is the spectral exitance of the chopper wheel, T_f is the transmission of the band pass filter, T_{BB} is the blackbody temperature, T_a is the ambient temperature, and T_w is the transmission of the window on the front of the Dewar.

2.1.3 Capacitance Voltage

Utilizing a Keithley CV suite with automated software capacitance-voltage relationships are recorded which can be used to extract doping and carrier concentration as function of irradiation. Typically, this measurement suite was employed on the largest variable area photodetectors available. An example CV plot is show below in Figure 2.5. As expected the carrier concentration didn't change appreciably as a function of dose and is still being explored for utility but interesting results from an annealing perspective were observed and will be discussed in a later chapter.
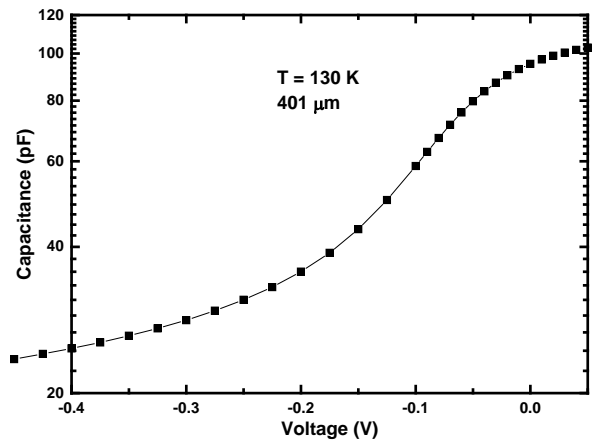
Fig. 2.5: Example Capacitance-Voltage sweep for typical InAs/InAsSb T2SLS nBn detector

2.2   Noise Current Measurements

For these measurements noise was measured using a transimpedance amplifier incorporating a dewar-mounted feedback resistor R_F and source-follower MOSFET, both held at 77 K. This configuration confines high detector impedance issues to the dewar, minimizes Johnson noise due to the electronics, and enhances bandwidth by reducing stray capacitance. In the detector community the importance of obtaining reliable yet timely performance results for single element detectors in growth-characterization campaigns is widely recognized. The method described here allows timely yet accurate noise spectrums for photodetectors to be produced while not having to invest the time or capital required to build a full focal plane array. When performing a literature search of the methods used to measure noise of single element detectors it quickly becomes apparent that a common method of indirectly estimating the detector noise exists. In this method the detector noise is computed using the data collected from a conventional I-V measurement. [14,15] The expression for noise that has recently become more common in the literature is

$$j_N = \sqrt{2qJ + (4k_B T)/R_d A_d} \qquad\qquad (2.6)$$

where q is the electronic charge, J is the current density, k_B is Boltzman's constant, T is temperature, R_d is the dynamic resistance, and A_d is the diode area. Given that the noise j_N expressed here is in units of A/Hz$^{1/2}$cm, equation 2.6 is convenient for estimating detectivity $D^* = R_{Peak} / j_N$, where R_{Peak} is the peak responsivity. However, this expression

also assumes thermal noise and shot-noise with a photodiode-like unity gain G are the only noise sources, an assumption which may not necessarily always be valid. For example, evidence that barrier-style detectors may have $G > 1$ was observed in [16].

The other significant issue with this noise expression is that it obviously does not account for $1/f$ noise or other potential noise sources, which may manifest in the signal-to-noise ratio at lower light levels. Focal plane arrays often run at frequencies ranging between 10-1000 Hz, making $1/f$ noise a distinct possibility. So while a cursory inspection of detectors is possible using standard dark-current measurements to estimate noise, it is nonetheless vital to understand how noise varies as a function of frequency to ultimately determine the minimum resolvable signal of the detector and thus its overall performance. The simplest alternative, method to measure noise, rather than estimating it via dark-current measurements, would be to use a commercially built TIA external to the Dewar in conjunction with a standard dynamic signal or network analyzer. The difficulty encountered with this approach is that the noise generated by the combination of the amplifier, Dewar, cabling and analyzer, is often much greater than that of the detector under test itself, the so-called *system-* or *amplifier*-limited scenario. The high noise floor can usually be attributed to a combination of thermal noise, electromagnetic interference (EMI), ground-loops, etc. Reducing each of these is key to measuring the detector noise. For example, the thermal noise current of the amplifier's feedback resistor i_j is given by

$$i_j = \sqrt{4k_B T \Delta f / R_f}, \tag{2.7}$$

where k_B is Boltzmann's constant, T is absolute temperature, Δf is bandwidth, and R_f is the feedback resistance. The only variables in equation (2) are T and R_f. The feedback resistance is determined by balancing considerations of noise and dynamic range; a larger R_f. reduces i_j, while a smaller R_f increases the amplifier's dynamic range and bandwidth ($\tau \sim C_f R_f$). Thus, a larger R_f is typically more ideal for noise measurements. The second variable T can only be reduced by cooling the feedback resistor. Cooling R_f from 300 K down to 77 K reduces i_j by the fraction $\sqrt{77/300} \sim 0.5$, which may be necessary if the detector noise is particularly small. Reducing other potential noise sources (i.e. EMI, ground-loops, etc.) requires a combination of proper shielding and grounding techniques.

Figure 2.6 below shows a block diagram representation of the test bed used to acquire data presented in this paper. A TIA that includes a source-follower MOSFET input-stage and feedback resistor mounted inside the dewar was used to convert the detector noise current to an output voltage. The TIA was battery-powered by a 12V battery to reduce 60Hz noise contribution. The noise spectrums from 1-10 kHz of the nBn detector under test were measured using a Stanford Research Systems model SR770 FFT network analyzer using the output of the TIA. The analyzer was read-out and controlled remotely via computer. A detector bias was applied using a Stanford Research Systems model SR570 low noise pre-amplifier.
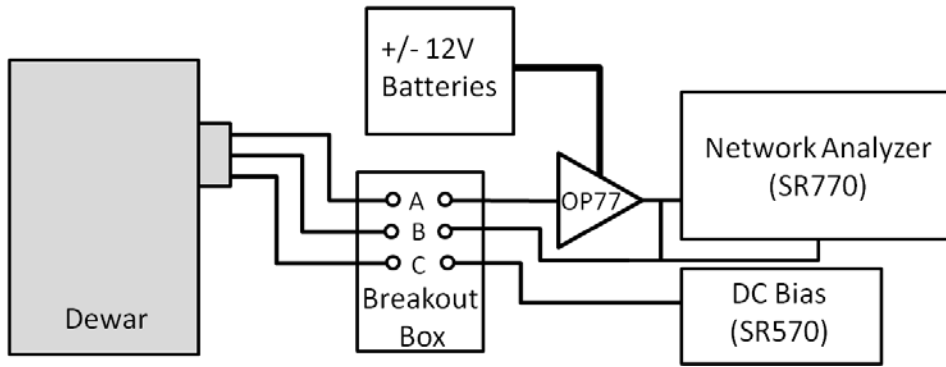
Fig. 2.6: Block diagram representation of noise measurement instrumentation. The letters A, B, and C are cross-referenced in following figure.

The TIA circuit used to characterize the detectors under test is shown in Figure 2.7. This circuit is fundamentally the same as that used by others performing noise measurements in this fashion with exception of the size of the feedback resistor. [17, 18, 19] The MOSFET-based input-stage is a source-follower circuit, which serves to help match the high impedance of the detector to the low input impedance of the OP77 op-amp that is external to the dewar and to provide significant current gain to drive the dewar cabling connected to the op-amp's inverting input.

This method of noise measurements affords several advantages. First, the virtual ground of the I-TIA is now within the dewar itself and closer to the detector and feedback resistor. The conventional long lead which traditionally brings a small current to the TIA's inverting input (required for traditional TIA configurations) and is prone to EMI is effectively eliminated here. Additionally, the thermal noise discussed in equation (1) can be reduced significantly by cooling the feedback resistor and MOSFET, which are both anchored to the liquid nitrogen bath. Furthermore, stray RC coupling can be minimized resulting in a reduction of the current leakage in cabling. The available current paths are reduced to just

those shunting the detector under test. The commensurate reduction in input capacitance

also reduces the "boosting" effect to amplifier voltage noise.
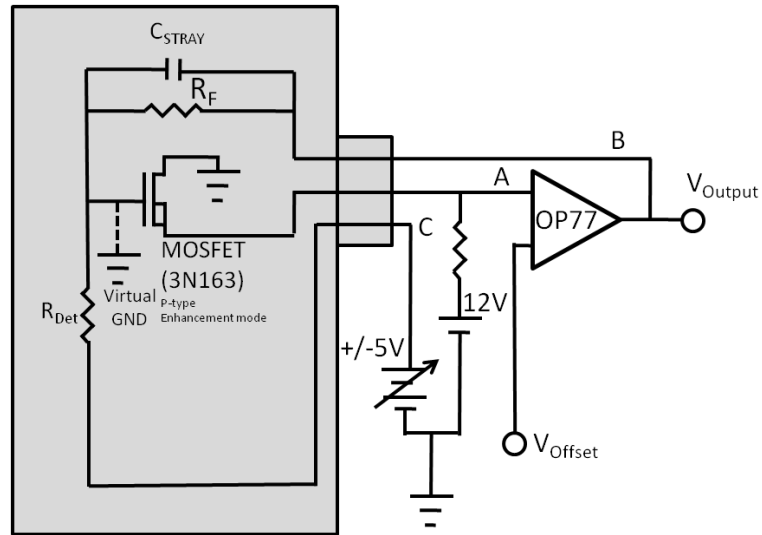
Fig. 2.7: Dewar mounted Trans-Impedance Amplifier circuit layout

In this TIA circuit a bias is applied across one end of the detector under test and earth

ground. However, the current measured through the detector is in reference to a virtual

ground that is isolated from earth ground. With this circuit layout only the current flowing

through the detector under test and therefore due to the summing point constraint through

the feedback resistor, R_F is measured.

The baseline noise of the measurement setup is shown by the black trace in Figure 2.8

below. This is the noise spectrum measured while the opposite end of the detector is left

open (disconnecting the bias source), which eliminates the detector as a noise source and

eliminates the current through R_F as a potential noise source. This was also the

configuration that was used to set the $V_{Offset,}$ such that $V_{Output} = 0$ V, which we refer to

herein as "balancing the circuit." In this case, the noise includes the thermal noise of R_F,

the MOSFET and the op-amp.

When the detector is under bias there will be additional noise sources present. In addition to the actual noise present from the sample under test there are several other noise sources associated with the measurement setup that needed to be measured to establish the baseline noise. These additional noise sources include the following; noise in fluctuations in the gate voltage of the MOSFET, op-amp noise, noise caused from current flowing through the feedback resistor. The combined noise from all of the noise sources mentioned results in the baseline noise spectrum shown in Figure 2.8 which is an order of magnitude lower than that of which is capable of being produced using an external Keithly 428 capacitance trans-impedance amplifier a standard instrument used in reporting by the detector community.
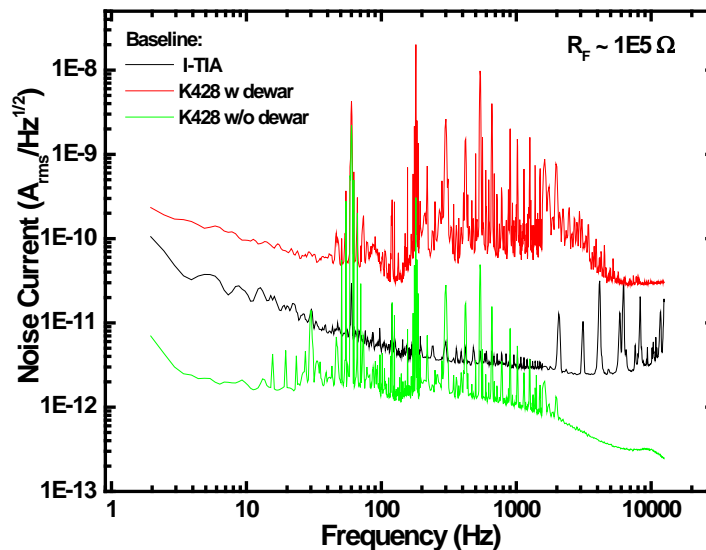
Fig. 2.8: Baseline noise current spectra from internal and external TIAs

The other two plots, shown for comparison purposes, are of the minimum noise floor spectrums of a conventional external Kiethley model 428 TIA, when both connected to the dewar (red trace) and completely disconnected (green trace). The gain setting on the external TIA for these plots was 10^5 V/A, similar to the $R_F \sim 10^5$ Ω of the internal TIA.

The green trace is very close to the manufacturer's expectation for the amplifier noise current. Comparing the green and red traces, it appeared that simply attaching the external TIA to the dewar itself leads to a dramatic increase in the noise floor of roughly 2-orders of magnitude and additional EMI. The black trace illustrates the advantage of using the internal-TIA setup. Here, both the noise floor and the EMI, indicated by the spikes at 60 Hz and its higher harmonics, are vastly reduced. The measured output noise for the I-TIA (black trace) most likely reflects the 1/f noise of the source-follower MOSFET. The noise amplitude, however, was above the expected level based on previous work, which may reflect the difference in the feedback resistor or be related to the MOSFET. [18]

Features of both HgCdTe and InAs/InAsSb unipolar barrier IR detector's noise spectrums at different bias are examined in this dissertation and will be presented in detail in another chapter.

2.3   In-situ Stepwise Irradiation & Characterization

Once all of the characterization suites described above are completed in a clear environment if the detectors performance was deemed sufficient to merit characterization in a radiation environment it was then in-situ stepwise irradiated in which after each dose the dark-current and optical measurement methodologies described above were repeated. The noise current measurements due to the requirement of having to conduct these measurements in another Dewar were only complete pre-irradiation and post the annealing experimental suite being executed. For all of the characterization work presented in this dissertation the detector under test was held at its desired operating temperature and

operating bias when it was irradiated to both eliminate annealing as well as mimic exactly what the IR detectors would experience on orbit.

2.3.1 AFRL Kirtland Air Force Base Co-60 Gamma Source

In exploring the utility of III-V based unipolar barrier detectors for potential space-based imaging applications, it's paramount to understand the total dose effects for this detector architecture. The ideal source to perform this surface limited radiation study is a Co-60 source that produces gamma rays with an energy of 1.17 MeV. The beauty of using this source is it doesn't have enough energy to displace atoms within the crystalline lattice of the detector instead the gamma rays that actually reach the detector cause ionizing damage. This generates excess electrons and holes in the detector some which get trapped on the surface or in passivating films that may be deposited. The Co-60 source behaves as a point source, such that all of the radiometric characterization electronics were located behind a lead brick wall to ensure that they were not subjected to any TID. It is anticipated that with the nBn and alike detector architectures that there will not be a passivation issue. This additional surface charging induced from the Co-60 source may result in flat-band voltage shifts and increased surface leakage currents. TID effects generally are more visible at lower device temperatures, where charges generated in oxide layers are less mobile, and tend to anneal out at higher temperatures. This dissertation explores this in detail, and results will be reported on later.

In order to understand the dose rates that the detector under test would be subjected to dosimetry was required. Dosimetry was performed by placing a dosimeter that measures dose rate in the plane inside the Dewar which the detector under test would sit. The Dewar was configured such that all of the shielding that was needed to conduct the nBn radiation

tolerance study was in place while the dosimetry was performed. The distance between the plane in which the dosimeter was located and where the cobalt source would be located, once raised, was recorded. The Cobalt-60 source was then raised for a fixed period of time and the dose rate was recorded independently three times. This procedure was repeated for a total of four different distances between the dosimeter and the source and the results were plotted on a log-log scale, as shown in Figure 2.9

Using this data a mathematical relationship was determined that describes the dose rate as a function of the distance between part under test and the Cobalt-60 source. Using that relationship the appropriate exposure times needed to build up to the desired total ionizing doses for this research presented later in this work was determined.
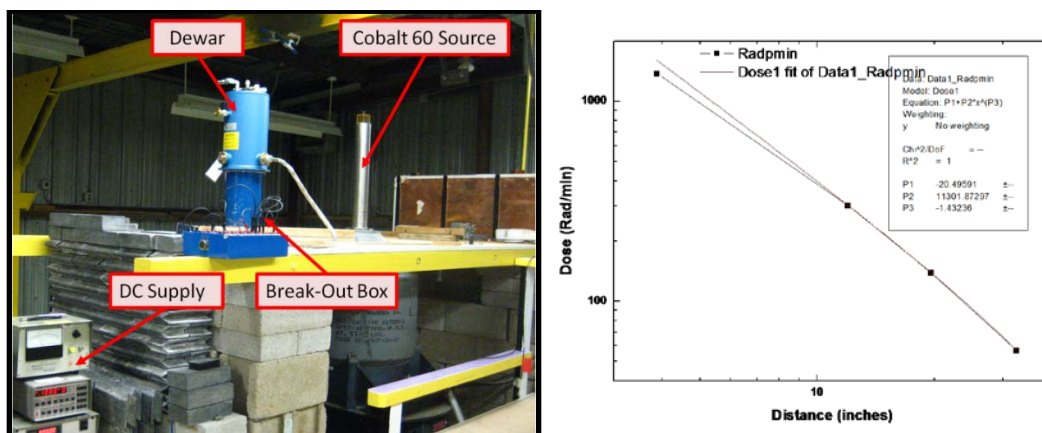
Fig. 2.9: Dose rate (rad/min) as a function of distance between detector under test and Co-60 source.

2.3.2   Crocker Nuclear Laboratory Cyclotron

The proton irradiation was performed at the Crocker Nuclear Laboratory at the University of California, Davis, using their 76" isochronous cyclotron, which can provide protons with energies up to 68 MeV. [20] The detectors were at their nominal operating conditions and

held under bias during proton irradiation. Photo-current and dark-current measurements were performed on devices at TID = 0, 2, 5, 10, 20, 50, 100 kRad(Si). Given the brag curve and elastic and inelastic bending it was decided for this body of research to use 63MeV protons as this would uniformly damage the detector material under test. Unlike the electon surface charging that the Co-60 source is capable of producing subjecting IR detectors to proton irradiation is expected to lead to both surface charging (in poorly passivated detectors) and displacement damage effects, both of which occur on orbit. This in turns leads to the introduction of mid-gap states within the valence and conduction bands. Displacement damage effects result from the occasional non-ionizing energy loss of an incoming proton due to elastic or inelastic scattering with an atomic nucleus that is sufficient to knock the atom from its lattice site and generate vacancy-interstitial pair, anti-sites, and defect complexes. These defects may manifest in lower η, due to the consequent reduction in minority carrier lifetimes τ, and higher J_D, due to the Shockley-Read-Hall mechanism. The proton fluence at 63 MeV required to alter the background doping levels, such that the fundamental Auger mechanism is enhanced, is expected to be order's higher than the fluence levels used here.

The profile of the beam at the Crocker Nuclear lab is such that it uniformity irradiated all of the devices under test and can be viewed in figure 2.10. The Dewar itself was carefully designed such that thin aluminum foils were in place to allow the detector under test to be irradiated from the side and preserve a light tight Dewar for optical measurements yet it can be interfaced with the end of the cyclotron using a kapton window for radiation experiments.
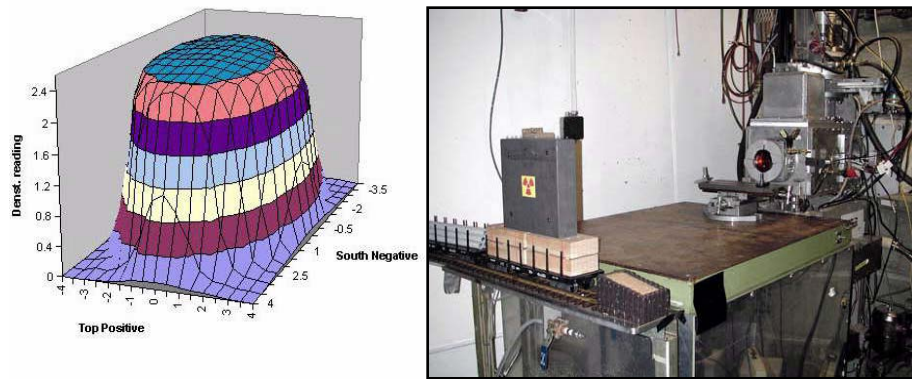
Fig. 2.10: Uniform top hat profile of cyclotron beam (left), end of cyclotron (right)

2.4   Annealing Studies

One of the more time consuming experiments but provides tremendous insights are the controlled annealing studies that are performed immediately after radiometric characterization of the infrared detector is completed post the final dose. For all of the research reported on here immediately once post final dose characterization is complete the detector is lowered to 80K and dark-current density measurements are collected on several photodetectors as function a temperature.   Once a detector temperature of 240K is reached the detector is warmed up to 300 K and held at this temperature for one hour followed by cooling all the way back down to the detectors operating temperature in which the full radiometric suite is taken. At this time a large portion of the surface charging effects and in research to be described in Section II of this dissertation and what would be deemed bulk effects associated with the detector anneal out and or partially recover at 300K. Following this the detector is lowered back down to 80K and systematically J is

measured again for the same devices that were measured pre-radiation exposure. Ultimately an Arrhenius-analysis is completed on these data and we are able to compare shifts in the diffusion limited regime of the detector as well as any onsets of trap assisted tunneling or less friendly dark current mechanisms. An example of this is shown in Figure 2.11 below:
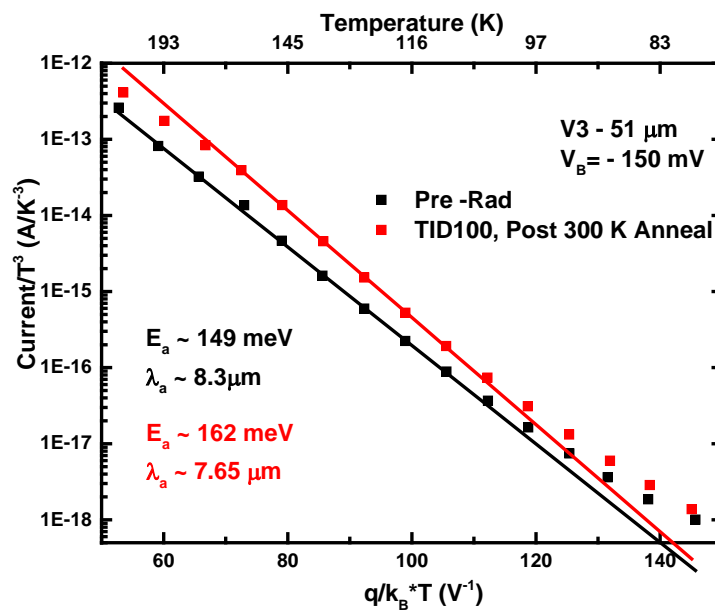
Fig. 2.11: Arrhenius analysis of IR detector pre and post irradiation

Now that all of the top level infrared detector radiometric characterization methodologies and radiation test infrastructure have been described in detail we will now move into the second portion of this dissertation, namely results.

3   HgCdTe IR Detector Radiometric and Radiation Tolerance Characterization

The last five decades have been dominated with investments in HgCdTe for the use in VIS through VLWIR applications. Tremendous progress has been made in driving the dark-current density and spectral QE to where it is now currently performing. It is of the upmost importance to understand where the current baseline HgCdTe IR technology is performing from a radiometric and radiation tolerance perspective in order to understand how T2SLS and bulk III-V alternatives compare.

3.1   Introduction and Motivation

There are multiple flavors of HgCdTe photodetectors being used for tactical and strategic applications. There are two growth techniques 1) Molecular Beam Epitaxy (MBE) and 2) Liquid Phase Epitaxy (LPE). These growth techniques will not be covered in detail, but should be mentioned at the top level as they are each capable of growing on CdZnTe Substrates and MBE can also grow on Si substrates. Each growth method has advantages and limiting attributes associated with them. Currently HgCdTe can be grown on lattice-matched on CdZnTe substrates using both techniques and results in some of the highest performance IR detector material available. A drawback of growing on CdZnTe substrates is they are limited to 7.5cm on a side for MBE and even smaller for LPE growth given required crystalline orientation. Ultimately this limits the size of the HgCdTe detector

array that can be fabricated. HgCdTe has also been grown on Si via MBE. In this case a buffer layer of CdTe is first deposited on top of the Si substrate to help lattice match to the HgCdTe layer. Even with the CdTe buffer layer, the dark-current, spectral QE, and radiation tolerance performance has been found to be degraded for HgCdTe grown on Si via MBE in comparison to growth on CdZnTe via MBE or LPE. Growth of HgCdTe via LPE similarly shares a maximum area limitation in the sense the LPE rockers that are available are only capable of fitting a maximum substrate that allows for a rectangle detector array to be produced with <4 cm on the shortest side.

All of the major permutation of HgCdTe detectors with several different cut-off wavelengths were characterized in a clear and radiation environment and results will be discussed in the following

3.2 Dark Current, Noise Current Characterization and Arrhenius-Analysis of MWIR HgCdTe p-on-n Photodiodes Grown Via LPE & MBE on CdZnTe

Figure 3.1 shows a direct comparison of the J_D vs. V curves of LPE and MBE photodiodes. A heuristic referred to as Rule '07 Citations here is often used as a comparison to deem how good the dark-current performance is of a HgCdTe photodiode relative to what was deemed state of the industry by Rule '07. Rule '07 came from an empirical fit of J_D versus $1/\lambda T$ for all of the dark-current data that was available at Teledyne/Rockwell over the last five decades. [21] Over the last half decade it has been adopted as an FPA/detector industry standard for comparison purposes especially when comparing new technology that is being

invested in as a competitor with HgCdTe. In this chapter and subsequent chapters, the results will be directly compared with the Rule '07 metric.

26um Device Pre Rad

	J (A/cm^2) Measured	Rule '07 (A/cm^2)
MBE (λ_c = 5.5 µm)	3.57E-6	5.77E-7
LPE (λ_c = 5.6 µm)	2.83E-6	8.769E-7
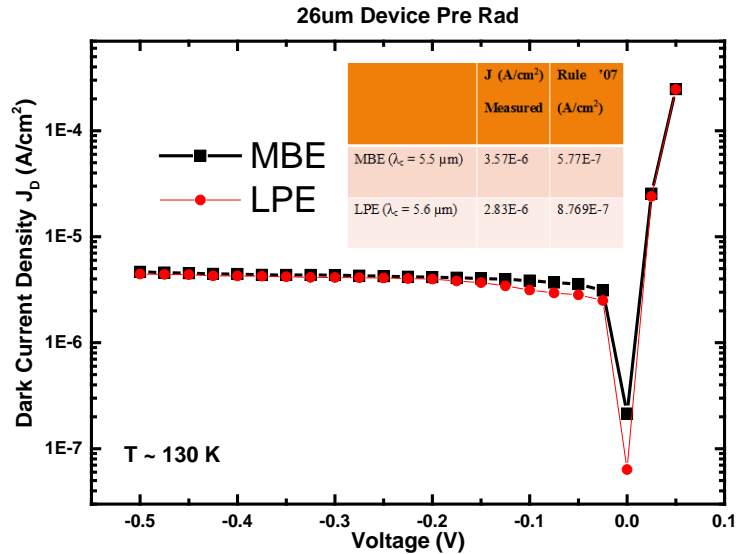
Fig. 3.1: J_D vs V for LPE & MBE grown p-on-n HgCdTe square photodiodes and their comparison with Rule '07.

It is important to point out the features associated with both of the I-Vs in Figure 3.1, they both have a relatively flat region at high reverse bias ($V_B < -.15$ V) and possess a very low turn-on voltage ($V_B \sim -50$ mV). The significance in this is that photodiodes grown by the MBE and LPE methods produced near diffusion-limited material at 130 K and no generation-recombination influence is observable. Later a full Arrhenius-analysis will performed to dive deeper into the different components contributing to the dark-current. It also should be noted that while both of these photodiodes J_D curves are very similar they still are greater than 5X larger than what Rule '07 indicates state of the industry performance would be.

Both the MBE and LPE grown HgCdTe photodiodes were irradiated with 63 MeV protons capable of displacing atoms within the crystalline lattice. Plotting the dark-current density as a function of proton fluence or TID yielded Figure 3.2.
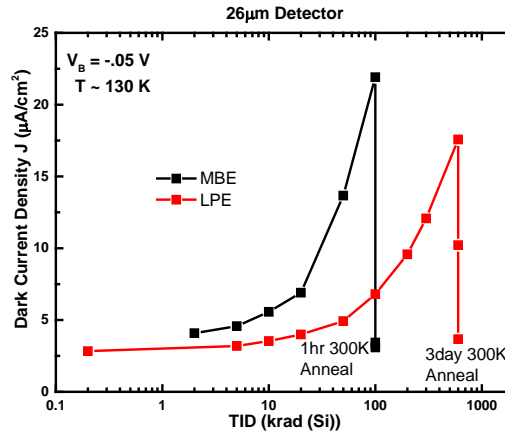
Fig. 3.2: J_D vs proton fluence for LPE and MBE grown p-on-n HgCdTe square photodiodes & thermal annealing results

One can see that the dark-current increased by 4X for the MBE and LPE grown HgCdTe material when irradiated with an equivalent TID of 100 krad(Si) and 500 krad(Si) respectively. After the final dose, a controlled thermal annealing experiment was performed in which it was found that both the detectors' J_D actually went back down to nearly their pre-radiation values. This is indicative of a surface charging effect likely due to poor passivation on each of the detectors and potentially generation-recombination current being present. Additional analysis of variable area diodes ranging in size from 26 - 801μm on a side was performed. The dark-current density for each of the grown materials was evaluated and is shown in Figure 3.3 below. Clearly as a function of perimeter to area ratio J was shown to increase for both materials. This also agrees with surface component being present in the dark-current increase with irradiation.
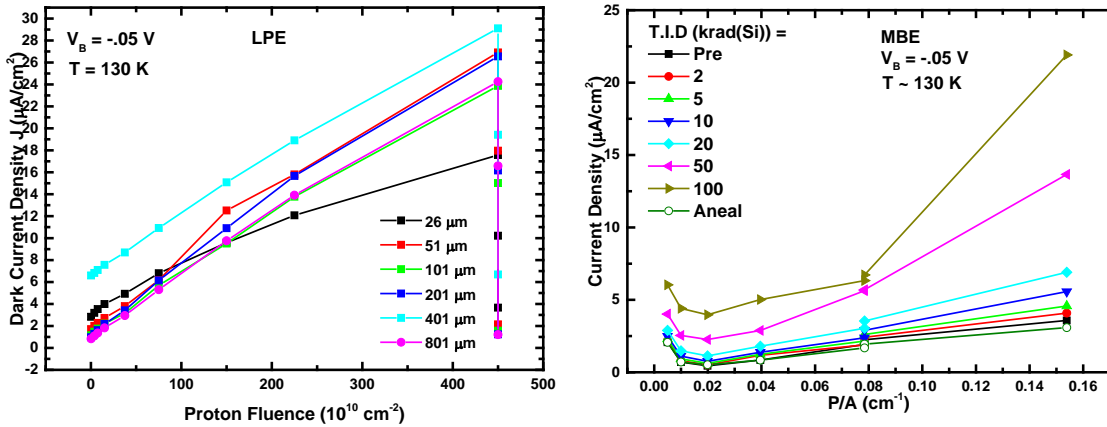
Fig. 3.3: J_D as a function of Proton Fluence/TID for LPE and MBE grown photodiodes ranging from 26 - 801µm on a side.

One of the more useful tools that we have when performing irradiation studies of IR detectors is to take IV's as a function of temperature and use cross section at various biases to perform an Arrhenius analysis. This provides key insights on the behavior of the photodiode. With an ideal photodiode, the Arrhenius plot would look like what is shown in Figure 3.4. In this Arrhenius plot, the detector's dark-current linearly decreases all the way to the background. In reality when working with non-ideal semiconductors where defects are present there can be three regimes in the plot of J_D vs $1/kT$ where k is Boltzmann's constant: a diffusion limited regime, a generation recombination regime, and possible a trap-assisted tunneling dominated regime where cooling the detector further has no impact on the dark-current density.
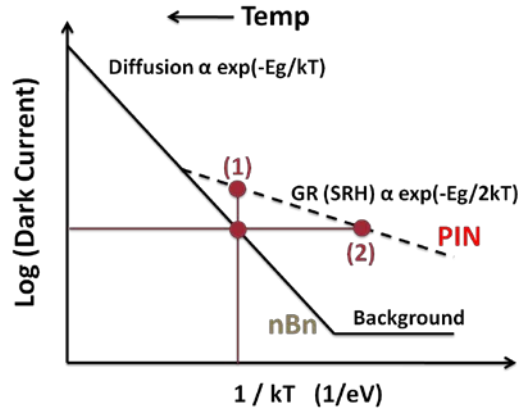
Fig. 3.4: Ideal Arrhenius plot of dark current

In Figure 3.5, the Arrhenius analysis was performed for 100 µm MBE and LPE grown photodiodes pre-radiation, post-radiation, and post 300 K thermal anneal. The diffusion limited regime was shown to be reduced by 20 K for the MBE grown device and by 15K for the LPE grown device after being subjected to a proton fluence equivalent to 100 krads(Si) TID.
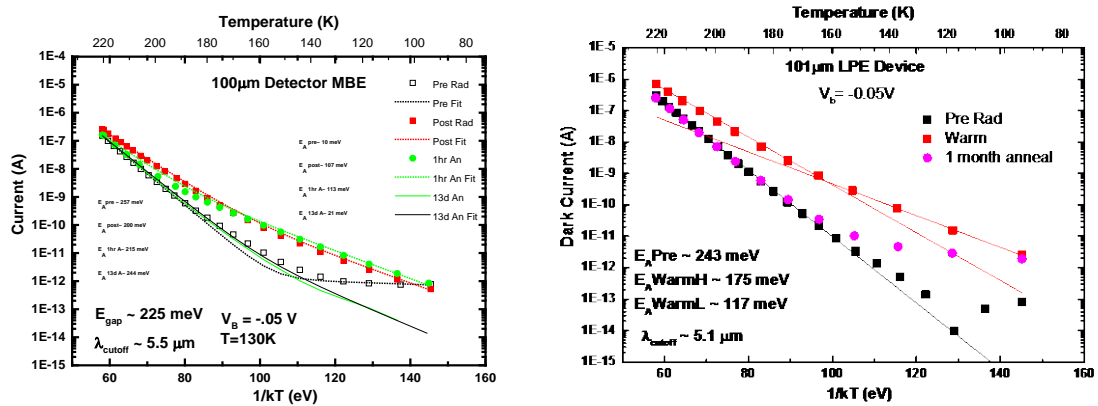
Fig. 3.5: Arrhenius analysis 100µm MBE and LPE MWIR HgCdTe device pre radiation, post radiation, and post 300K anneal.

Noise current measurements were also conducted on a 51 um diameter LPE detector to serve as comparison with III-V technologies. After carefully sizing the feedback resistor for the Dewar housed source follower to match the resistance of the detector at 130K operating temperature and V_{Det} a noise spectrum was collected on several varying size HgCdTe photodiodes. The noise spectrum is shown below in Figure 3.6 and these noise currents are used for later comparisons with III-V nBn and alike family of IR detectors in Chapter 4.

Frequency (Hz)	1	10	100
Noise Current Pre Rad ($A_{RMS}/Hz^{1/2}$)	4.6 E-13	6.1 E-14	4.0 E-14
Noise Current Post Rad 600 KRad (Si) ($A_{RMS}/Hz^{1/2}$)	4.9E-13	6.3 E-14	4.8E-14
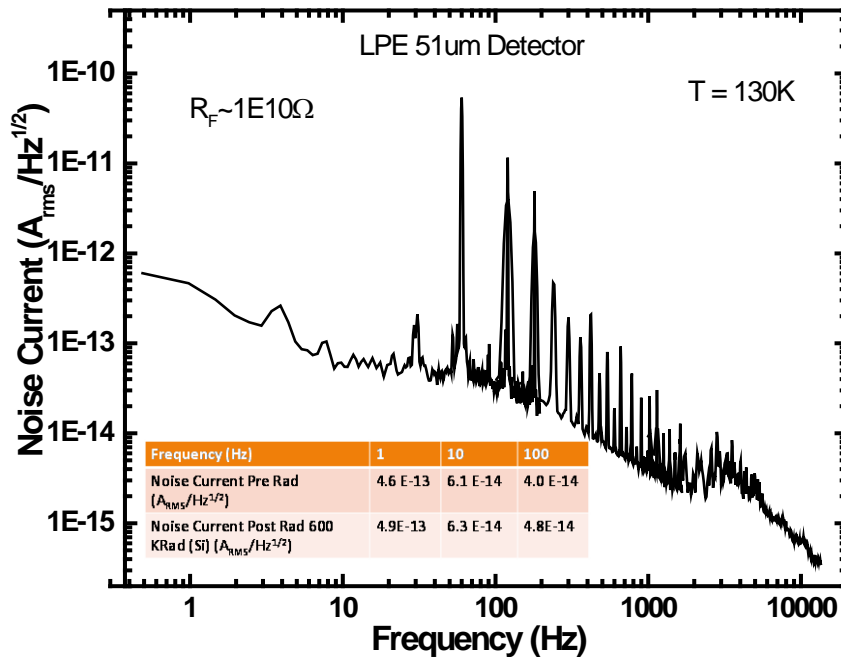
Fig. 3.6: Noise current for MWIR HgCdTe p-on-n photodiode grown via LPE and noise currents at 1, 10, and 100Hz.

The noise current post irradiation with 63MeV protons to equivalent TID of 600 krads(Si) was found to increase the noise current of the HgCdTe detector minimally at lower frequencies but substantially at higher frequencies. Specifically, the noise current 1, 10,

and 100kHz was found to increase by 6, 3, and 20% respectively. This will conclude the section of dark-current, noise current, and Arrhenius analysis as a function of 63MeV proton irradiation of MWIR detectors grown via MBE and LPE. We will now move into the characterization of these detectors quantum efficiency and lateral optical collection length as a function of 63 MeV proton irradiation.

3.3 Quantum Efficiency and Lateral Optical Collection Length Characterization of MWIR HgCdTe p-on-n Photodiodes Grown Via LPE & MBE on CdZnTe

As described in Chapter 2, the detector proton irradiation was performed at the Crocker Nuclear Laboratory (CNL) at the University of California, Davis.

Each experiment was also completed similarly to the J_D characterization using a similar step-wise irradiation-measurement approach (measuring detectors, dosing with protons, re-measuring, re-dosing, etc…) until a TID > 100 kRad(Si) was reached. This step-wise approach allows for degradation rates to be determined. Irradiation was performed with 63 MeV protons across same fluence range (10^9-10^{12} p/cm^2) using roughly similar dose schedules (e.g. 2, 5, 10, 20, 50, 100 kRad(Si)). At 63 MeV, the Bragg peak is expected to be well past the active region of the detectors. Thus, a nearly uniform dose and induced damage across the thickness of the detector's active region is expected.

The quantum efficiency and lateral optical collection length were measured for the LPE- and MBE= grown HgCdTe materials in a step-dose fashion with irradiance reflective of strategic applications. Below Figure 3.7 shows the transmission of the bandpass filter that was selected for these measurements along with the spectral response measured for the

detector under test. Great care went into selecting a band pass filter that had its pass band in a regime that was flat or relatively flat, in the spectral response of the detector. The quantum efficiency measurements that are reported will be at the center of this pass-band.
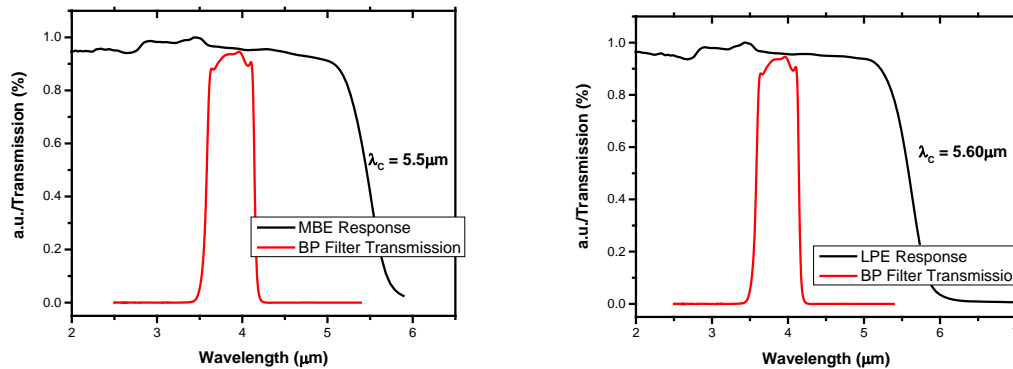
Fig. 3.7: Spectral response for MBE- and LPE- grown HgCdTe p-on-n photodiodes and transmission of theband pass filter selected for optical measurements.

The radiometry was such that with the black body temperature selected, pinhole, band-pass filter, distance from the detector, and limiting aperture, the optical irradiance on the part was 1.6×10^{14} and 2.7×10^{14} photons/cm^2 for the MBE- and LPE- grown detectors respectively. In a step-dose, in-situ fashion, both detectors were irradiated. The MBE-grown detector's quantum efficiency was found to decrease at a faster rate than that of the LPE-grown detector. It is important to recognize that the LPE-grown material was dosed to a proton fluence a factor of 6X higher than that of the MBE-grown detector, but the rate of degradation leading up to 7.5×10^{11} protons/cm^2 or 100 krad(Si) equivalent total ionizing dose was a factor of 6X higher as shown in Figure 3.8.
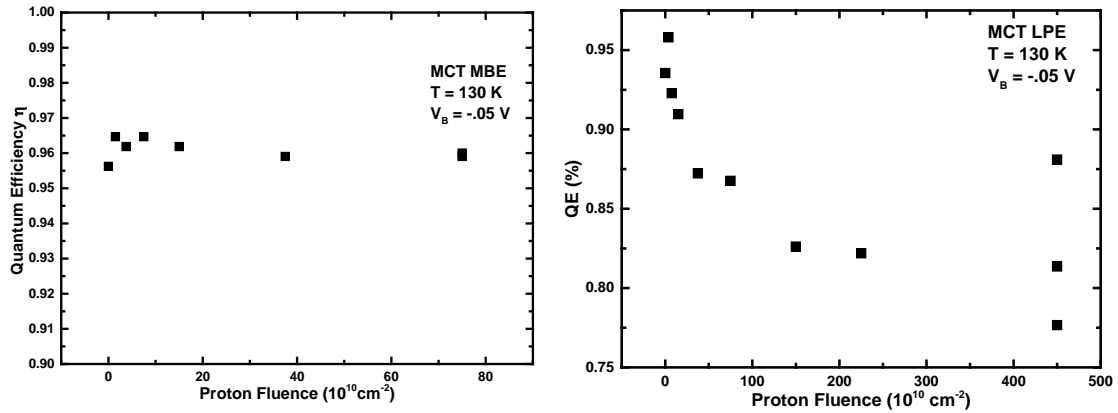
Fig. 3.8: Quantum efficiency vs proton fluence for MBE- and LPE-grown HgCdTe p-on-n photodiodes.

It was hypothesized that this particularly MBE grown HgCdTe had a longer depletion region than that of the LPE-grown detector, and this was the contributing reason to why the QE degraded at such a fast rate.

L_{OC} was characterized as a function of proton fluence and is shown in Figure 3.9.
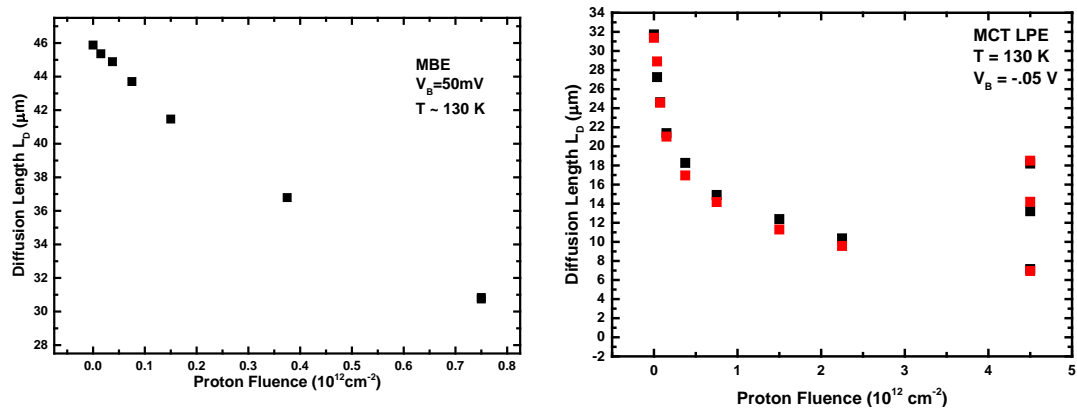
Fig. 3.9: Lateral Optical Collection Length (L_{OC}) vs proton fluence for MBE and LPE grown HgCdTe p-on-n photodiodes.

 Damage factors were extracted by performing an empirical fit of $1/(L_{oc})^2$ as a function of proton fluence as shown in Figure 3.10. As hypothesized, the LPE-grown $1/(L_{oc})^2$ was found to be 3X larger than that of the MBE-grown detector. These damage factors will be used as a comparison with the III-V based nBn and alike detector family in Section III Chapter 6.

	MBE	LPE	Past SWIR work
Damage Factor $(1/\mu m^2)(p/cm^2)$	1.54 E15	4.29 E15	2.5 E15

Equation	y = a + b*x		
Weight	No Weighting		
Residual Sum of Squares	1.85999E-9		
Pearson's r	0.99914		
Adj. R-Square	0.99793		
		Value	Standard Error
invLd2	Intercept	9.4446E-4	9.2838E-6
	Slope	1.54503E-15	2.86918E-17
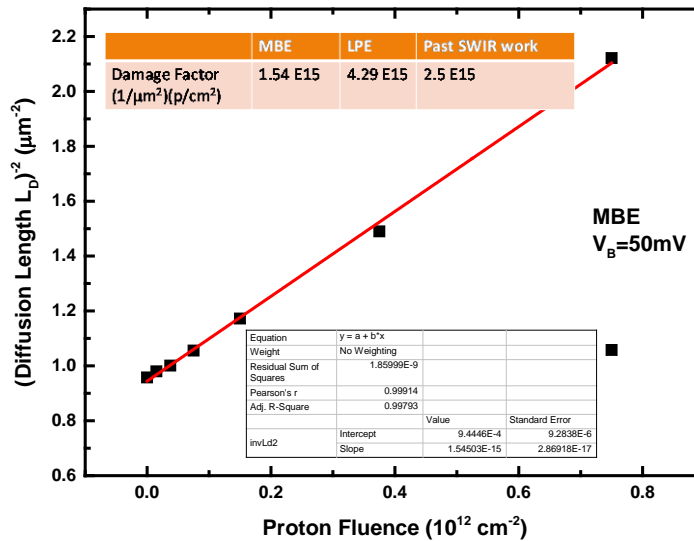
Fig. 3.10: $1/(L_{oc})^2$ damage factor analysis and tabulated damage factors for MBE and LPE grown material along with previously measured LPE grown SWIR HgCdTe on CdZnTe

MWIR MBE- and LPE-grown HgCdTe detectors on CdZnTe were proton-irradiated to 100 and 600 kRads (Si), respectively. Measured dark-current, QE, and L_D were reported as a function of 63MeV proton dose and damage factors were calculated. Significant room temperature annealing effects for both dark-current and QE and L_{oc} in both LPE and MBE grown devices were observed. A shift of 10-20 K was observed from Pre→Post-irradiation Arrhenius data where the dark current behavior transitioned from diffusion limited to generation-recombination dominated.

3.4 63 MeV Proton Radiation Characterization of MWIR HgCdTe p-on-n Photodiodes Grown on Si-Substrates

Given the size constraints associated with growth of large format HgCdTe photodetectors it was relevant to perform a proton radiation-tollerance characterization of HgCdTe p-on-n photodiodes grown on Si. As stated previously the limiting formats for MBE and LPE grown HgCdTe on lattice matched CdZnTe at the time this dissertation is being drafted are 7.5 and 4 cm on side, respectively. Given the desires of E/O instrument builders for larger format IR detectors the IR community has invested significant research into the growth of HgCdTe on large Si substrates. This section is devoted to discussing the characterization of proton-irradiated MWIR HgCdTe detectors grown on Si. At present date, HgCdTe on Si is a competitor to the III-V-based nBn IR detectors that can similarly be grown on highly uniform 6" and larger GaAs substrates.

This section will provide top level radiometric results in attempt to maintain momentum with the reader. The spectral response measured for the HgCdTe on Si is shown in Figure 3.11. In comparison to the HgCdTe grown on CdZnTe presented in the previous section one can immediately observe that the spectral quantum efficiency in the SWIR is degraded for this material. The same optical band pass filer previously used is likewise employed for these samples. The incident photon flux on the detector was calculated to be 3.2 x10^{14} photons/sec cm^2.
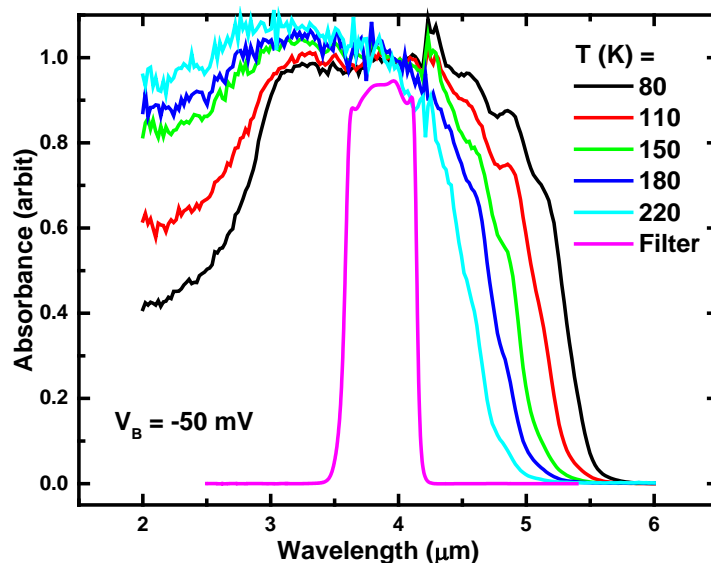
Fig. 3.11: Spectral response and transmission spectra for MWIR HgCdTe grown on Si via MBE and optical band pass filter.

There were issues with the absolute QE in this measurement such that the photocurrents were higher than what was expected and it is believed that the cause of this was edge coupling on the process evaluation chip that was under test that contained the variable area photodiodes. That said it needs to be noted that the following plot of QE shown as a function of proton fluence/TID in Figure 3.12 has been normalized. To date this hasn't been reconciled but is being pursued. This of course doesn't change the relative degradation in QE vs proton fluence which is the underlying motivation for this research anyway. The HgCdTe grown on Si's QE was found to degrade by ~20% when subjected to a TID equivalent of 150 krad (Si). When a 300K anneal was performed the QE was found to recover completely. This correlates well with the dates shown previously for the HgCdTe grown on CdZnTe. A QE damage factor (K_{QE}) was found to be 1.1 x 10^{-13} cm^2 for this rate of QE degradation.
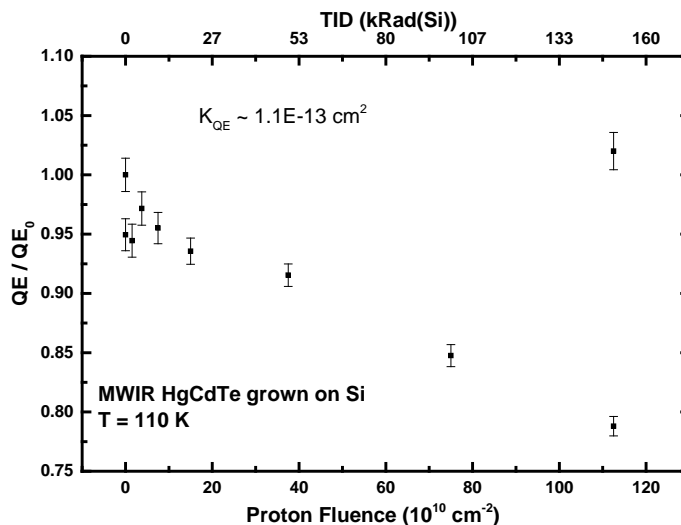
Fig. 3.12: QE vs proton fluence for MWIR HgCdTe grown on Si via MBE and associated damage factor.

It should be noted that this characterization was performed at 110K due to the higher dark-current that the HgCdTe on Si was discovered to have. Just as for the HgCdTe on CdZnTe, the lateral optical collection length was measured and a damage factor was extracted, K_{Loc} ~ 8.5 x 10^{-16} cm^2/µm^2, as shown in Figure 3.13.
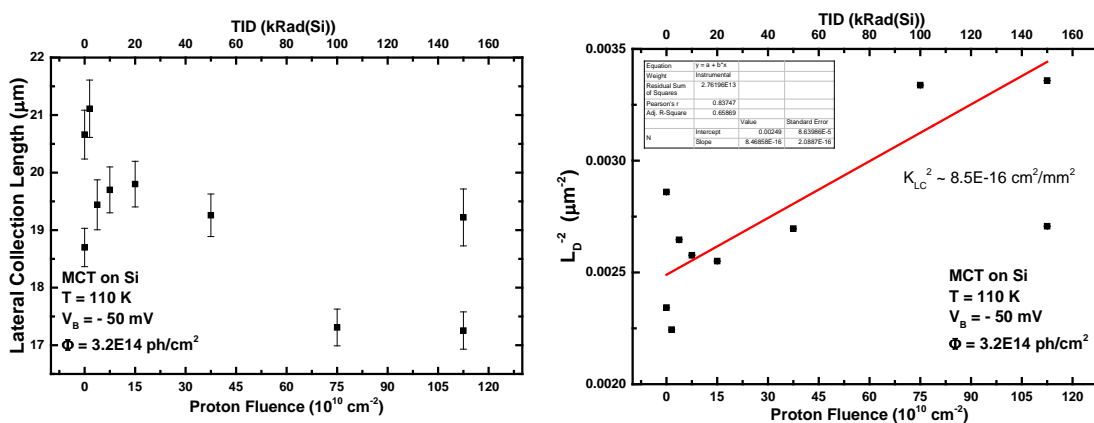
Fig. 3.13: L_{oc} vs proton fluence for MWIR HgCdTe grown on Si via MBE and associated damage factor.

The dark-current IVs for the HgCdTe grown on Si have significant generation recombination at higher reverse bias as compared to the HgCdTe grown on CdZnTe. See Figure 3.14. At higher proton fluences the GR tail increased drastically when compared to growth on CdZnTe. Damage factors were extracted for the J vs proton fluence and KJ_{DARK} was found to be 5.6 x 10^{-20} A/proton which equates to a 2.2X increase in J from TID 0 to TID 150 krad(Si). A 300K thermal anneal resulted in an 85% recovery of the pre radiation dark-current. This implies that there is a passivation issue and some mid gap states were introduced by the displacement damage.
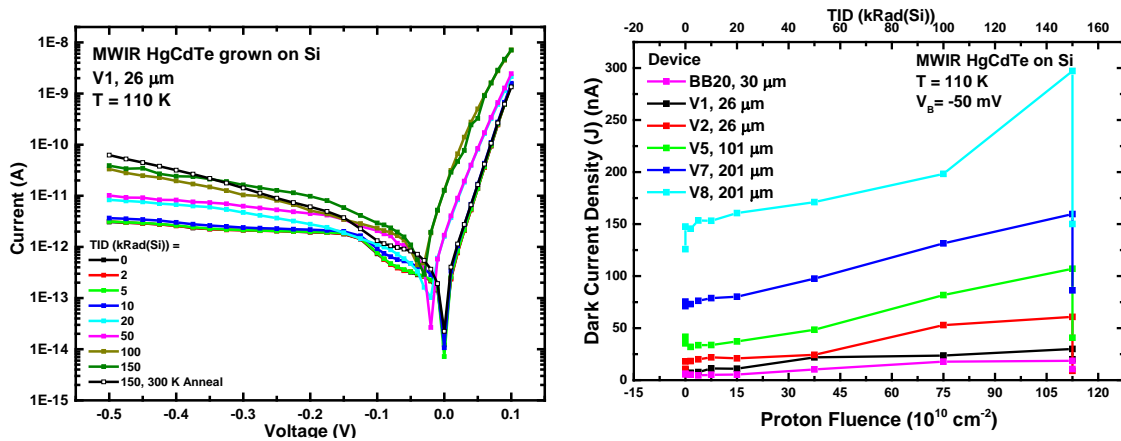
Fig. 3.14: J vs proton fluence for MWIR HgCdTe grown on Si via MBE and associated damage factor.

When investigating the J_D P/A, it was found that the bulk dark-current density pre-rad ~ 1.5E-7 A/cm^2, post-rad ~ 2.9E-7 A/cm^2, and post-300 K anneal ~ 1.5E-7 A/cm^2. The Rule '07 suggested J_D ~8.9E-10 A/cm^2, is two orders of magnitude higher than state of the industry HgCdTe photodiodes operated at the same temperature and like cut-off

wavelength. It is believed all of this is attributed to additional dislocations created from the lattice mis-match between the buffer layer grown on top of the Si substrate.

Completing an Arrhenious-analysis unveiled that the HgCdTe grown on Si was only diffusion limited down to 150 K which was 30 K higher than that of the CdZnTe counterparts. When analyzing Figure 3.15 specifically the slope change at low temperatures, the material appears Shockley-Read-Hall limited as the activation energy (E_A) is ~ ½ the band gap energy (E_G). The change in slope may indicate an additional mechanism, such as tunneling, could be present.
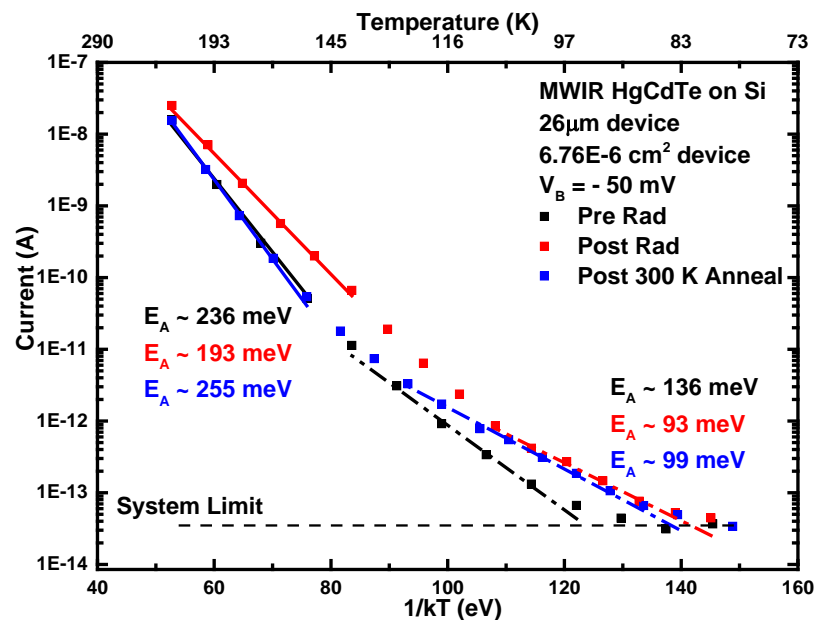
Fig. 3.15: Arrhenius-analysis of 26 µm MWIR HgCdTe photodiode grown on Si via MBE.

Finally, it is prudent to discuss the SNR and specifically the shift in turn-on of photodiodes when irradiated. Figure 3.16 is a plot of the SNR as a function of proton fluence. When one takes the first derivative of this, it quickly becomes apparent that the turn-on voltage

is shifting to the right, something very similar was observed in the characterization of III-V-based nBn detectors. It was prudent to characterize the detector at a reverse bias sufficient to ensure that at higher irradiation one was never operating the detector on the knee of this curve. The SNR for the HgCdTe on Si was found to degrade by nearly 20% when comparing pre-rad to post-rad TID accumulation.
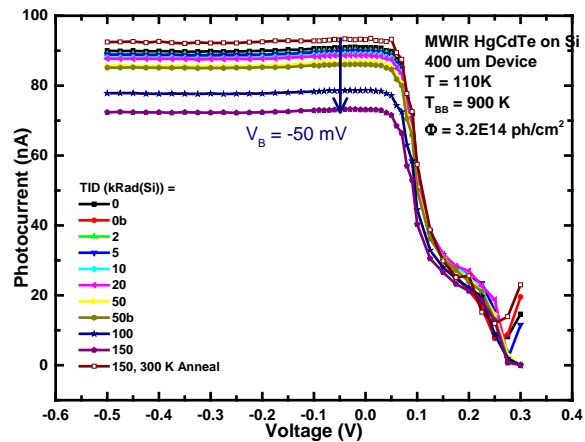
Fig. 3.16: Photocurrent vs dose for 400μm MWIR HgCdTe photodiode grown on Si via MBE.

3.5 Conclusion and Discussions

In conclusion, in-depth characterization of state of the industry HgCdTe IR detectors in both clear and a 63 MeV proton environment was conducted. It was found that both LPE and MBE grown HgCdTe on CdZnTe as well as growth on Si via MBE exhibited characteristic surface charging. This was discerned by the drastic thermal annealing that occurred. The quantum efficiency was found to be degraded significantly due to a reduction in L_D which nearly completely thermally annealed out. The dark-current density of the HgCdTe photodiodes in all cases was found to be 1-2 orders of magnitude higher

than that of which Rule '07 predicts. The dark-current density associated with the HgCdTe grown on Si was higher and it is believed this is an artifact of dislocations as a result of not growing on a lattice-matched substrate. When an in-depth Arrhenius-analysis was performed it was discovered that the diffusion limited regime was truncated due to generation recombination.

From a broader perspective, it should be noted that if an IR detector die greater than 7.5cm on a side is required there are performance penalties moving to HgCdTe on Si. The degradation in L_{OC} is indicative of the minority carrier lifetime degrading which in turn leads to a decrease in the diffusion QE and an increase diffusion and generation-recombination dark currents. Annealing of L_{OC} for HgCdTe regardless of growth method or substrate is evidence that there is a recovery in the minority carrier recombination lifetime. This was later quantified in detail by a colleague at the Air Force Research Laboratory on representative HgCdTe lifetime samples via time resolved photoluminescence. [22] Exploring alternative III-V based nBn and alike IR detectors that employ unipolar barriers has potential merit given the large format substrates that are available for growth. The current radiometric performance will be discussed in the chapter to follow.

4 Systematic Study of Radiation Induced Degradation of T2SLS and Bulk III-V Based Unipolar Barrier Infrared Detectors

In this chapter a systematic study of radiation induced degradation of various unipolar barrier infrared detector designs utilizing both bulk and T2SLS absorbers with various cut-off wavelengths will be presented. It will begin with various radiometric results in a clear environment, followed by a presentation of nBn radiometric results when step-dose in-situ irradiated using a Co-60 source, and select examples of displacement damage experiments that were conducted. This systematic study unveiled a commonality in the radiation degradation across the over 30 III-V based nBn and alike detectors that were characterized. Once again in an attempt to keep reader momentum only highlights will be discussed. If interested in learning more any of the papers tabulated in Chapter one will provide additional context on where assertions are pulled from.

4.1 Deep Cryogenic Radiometric and Noise Current Characterization of InAs/GaSb-based IR Detector

Going back to the beginning of this dissertation research circa 2010 no one at that point had characterized a unipolar barrier IR detector with a T2SLS absorber or for that matter and unipolar barrier detector at temperatures below 77K. This section will discuss the

results from this radiometric characterization. [23] The detector that was characterized with the cross section shown in Figure 4.1 was grown at the Center for High Technology Materials at the University of New Mexico. [14] It was a standard nBn utilizing a InAs/GaSb T2SLS absorber. Radiometric characterization took place from 10 – 300K over a broad range of operating biases.
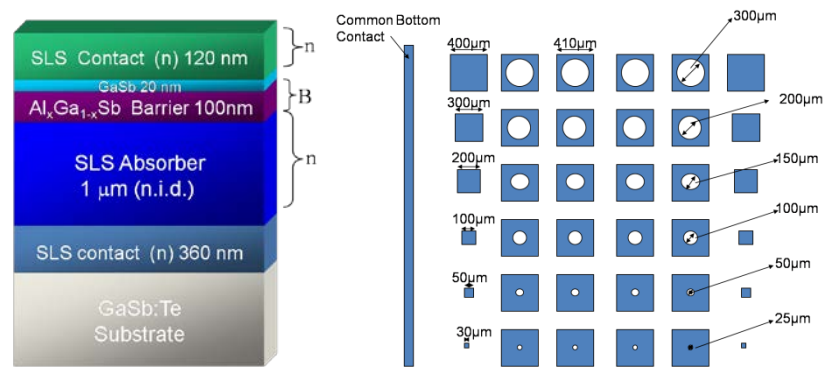
Fig. 4.1: Cross section of nBn material characterized (Left), processed detectors (Right).

It's prudent to point out again that this was circa 2010 and as a result radiometric characterization capabilities were being stood up and refined in parallel, the automation of temperature dependent data collects hadn't taken place yet so the results will very likely be viewed as crude. The dark-current was measured for 400 µm device down to 11K and is shown in Figure 4.2. An Arrhenius analysis was performed and it was found that the nBn detector was diffusion limited down to 128K with 50mV applied bias.
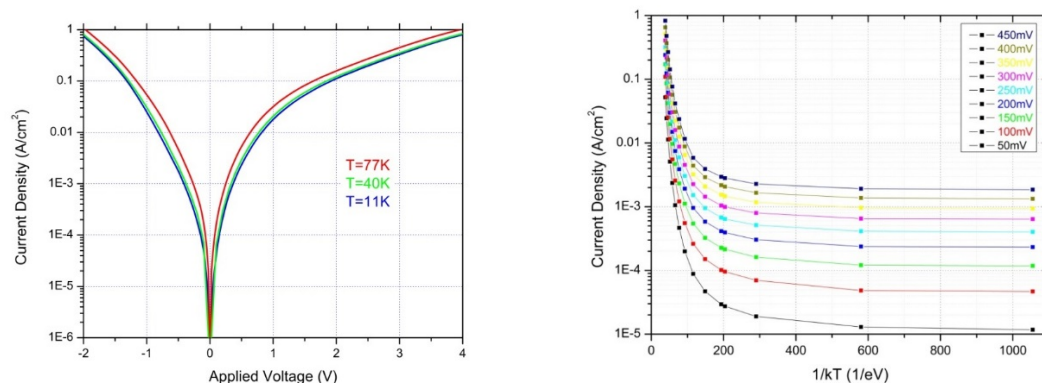
Fig. 4.2: 400µm nBn IVs (Left), J vs 1/kT as a function of reverse bias applied (Right)

That nBn absorption spectrum was measured and ultimately a responsivity that as shown in Figure 4.3 which corresponds to a QE of ~8% for the nBn with a 1µm thick absorber with a single pass geometry.
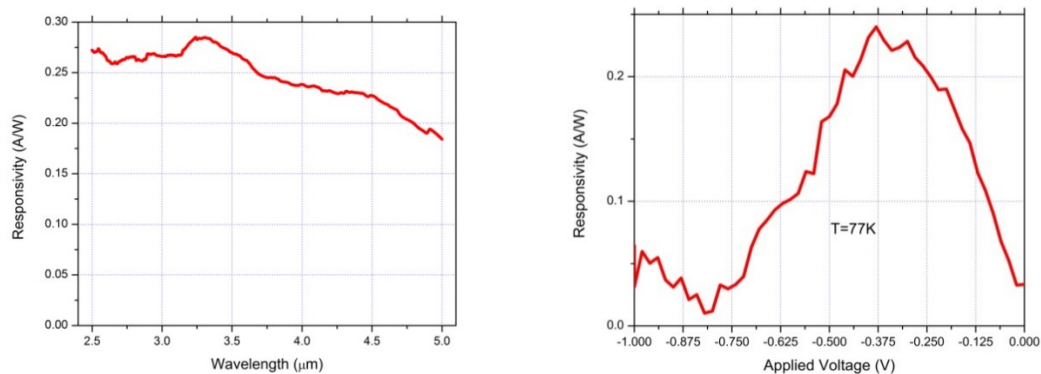
Fig. 4.3: 400µm nBn Spectral Responsivity (Left), Responsivity vs applied bias (Right)

While these experimental results certainly by the standards in place when the dissertation is being assembled it isn't intuitive that they are worthy of including but it is prudent to point out that this was the first ever deep-cryo characterization of an nBn and the data indicated that there wasn't trap assisted tunneling mechanisms present which at the time

boded well for the technology. Additional comprehensive radiometric characterization of state-of-the-industry nBn and alike unipolar barrier infrared detectors will be included as a part of the pre proton radiation characterization in section 4.3.

A similar InAs/GaSb T2SLS based nBn detector grown at the University of New Mexico Center for High Technology Materials was characterized from a noise current perspective. At the time this research was executed the nBn detector community was very interested how noise currents were effected by shallow and trench etches where a trench etch fully reticulates the pixel etching through the barrier of the nBn and the shallow etch only etches to the top of the barrier. A 410µm square shallow and trench etched nBn were characterized and shown in Figure 4.4. It was found that the noise current increased at a faster rate for shallow etched devices in comparison to the trench etch. 1.5 orders of magnitude of change was observed from 10 - 10kHz. The first regime from 1-10 Hz is most likely random telegraph signal, followed by role-off likely introduced from attributes of the amplifier circuit itself. At zero bias the reduction in nose current as a function of frequency is likely introduced from 1/f in the FET.
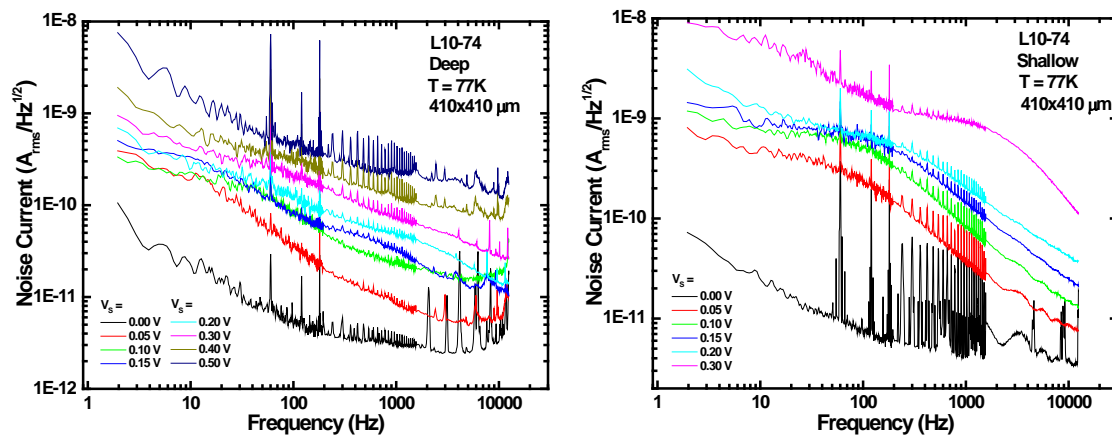
Fig. 4.4: Deep etched InAs/GaSb nBn noise spectrum (Left), Shallow etched InAs/GaSb nBn noise spectrum (Right).

Extracting the noise current as a function of applied bias for both the deep and shallow etch devices and comparing this to the calculated noise using the dynamic resistance is shown in Figure 4.5 which clearly show the performance overvaluation that results. This was reported on to the community in 2011 as this flawed method of estimated noise is prevalent.
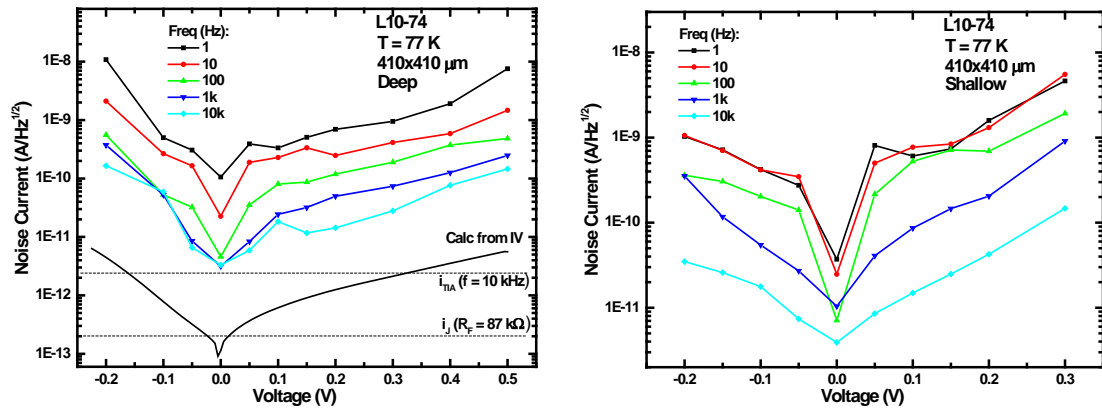
Fig. 4.5: Deep etched InAs/GaSb nBn noise current vs detector bias (Left), Shallow etched InAs/GaSb nBn noise current vs detector bias (Right).

The noise current was found to be 1-2 orders higher than that of which is calculated from the dynamic resistance (second horizontal line in left most plot in Figure 4.5). Fitting the shot noise components for both the deep and shallow etched devices is shown in Figure 4.6. The slope was found not to equal 2q therefore the detectors were not Shot noise limited, instead a multiplicative gain term is present pointing toward multiple random telegraph noise sites and requires additional investigation that is ongoing and more details on this topic are included in one of the many publications on this research. [12]
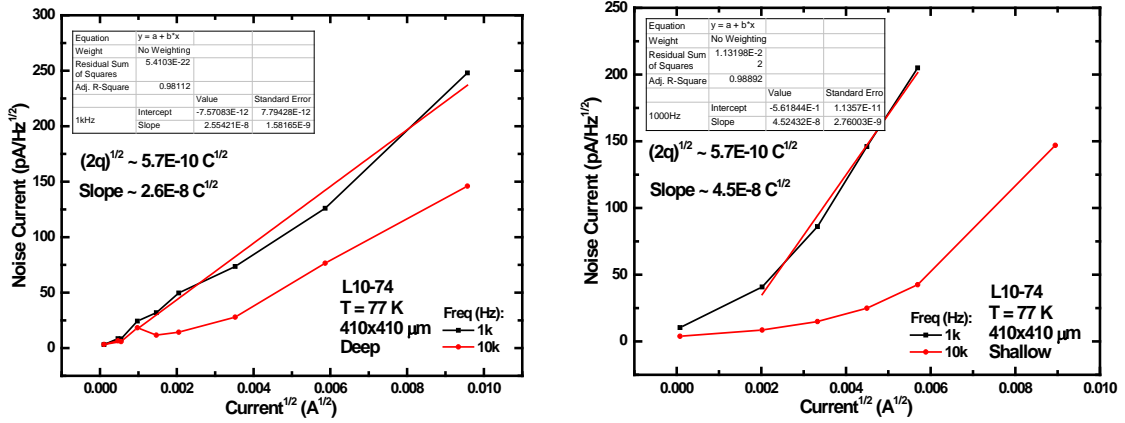
Fig. 4.6: Deep etched InAs/GaSb shot noise fitting (Left), Shallow etched InAs/GaSb nBn shot noise fitting (Right).

With a similar nBn device held at 80K when studying noise currents it was found that at low frequencies shared the same behavior as the P/A analysis of dark-current as shown in Figure 4.7. Pointing towards there being surface current issues in the device. At very high frequencies the noise was found to be very close the shot noise estimate. [24]
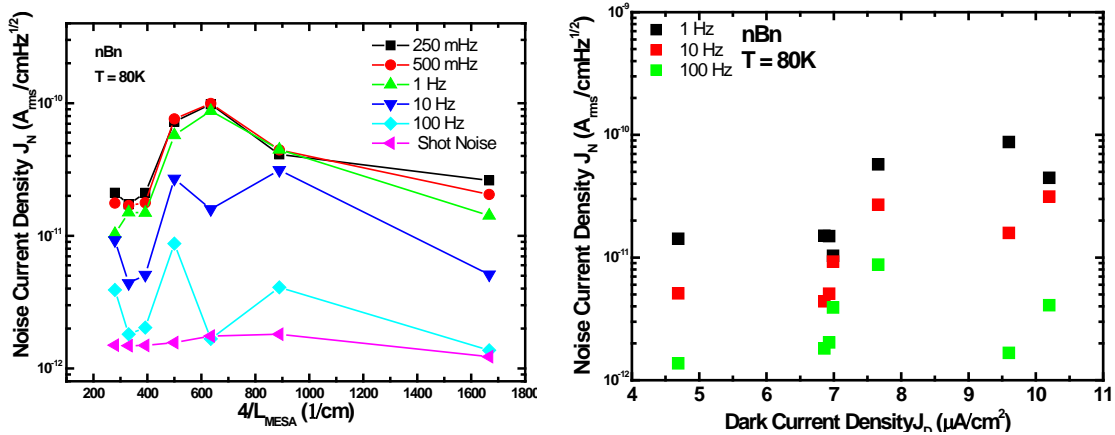
Fig. 4.7: Noise current density and shot noise vs P/A for InAs/GaSb nBn (Left), noise current vs dark-current density for InAs/GaSb nBn (Right).

The discrepancies in noise reporting was clearly reported in this section (1-2 orders discrepancy). This was the first ever reported internal 77k cooled source follower noise spectra measurement for an IR detector that employed a barrier architecture. For both shallow and deep etched devices the noise current is appreciably less at higher frequencies. The noise current increases at a faster rate for deep etched devices as a function of the dark-current density increasing.

4.2 Co-60 Total Ionizing Dose In-situ Stepwise nBn Characterization

Concerning space-based applications, characterizations of type-II SLS detectors operating in an ionizing radiation-filled environment have not been widely reported. At the point this work was completed and published the authors' knowledge, there are no reports of radiation tolerance studies for IR detectors with the nBn architecture. [12] The Naval Research Laboratory has reported that there is little degradation below 1 Mrad(Si) from incremental proton fluences of 1 MeV on first-generation antimony-based type-II SLS samples. [25] This provides a good indication regarding the radiation tolerances of these materials without considering other performance metrics. Further reporting on radiation damage for more advanced SLS architectures operating in the LWIR also shows potential for space applications. [26]

Analysis of the optical and electrical detector degradation in a gamma radiation environment provides indicators of potential space survivability. Degradation from the

gamma irradiation dose can result from the accumulation of trapped electrons that alter the detector's electrical properties and ultimately can lead to functional failure. The nBn IR detector under test, is composed of an InAs/GaSb SLS absorber (*n*) and contacts (*n*) with an $Al_xGa_{1-x}Sb$ barrier (*B*) grown by solid source molecular beam epitaxy (MBE). This particular detector architecture was developed once again by the Center for High Technology Materials (CHTM) at the University of New Mexico.

The scope of this section is to present the results from the first in-situ stepwise characterization of an nBn detector's tolerance to TID. The gamma radiation that was used for this study was produced using the Air Force Research Laboratories (AFRL) Cobalt-60 source located at Kirtland Air Force Base.

4.2.1   Co-60 In-situ Stepwise Electrical Characterization Results

The dark-current density of a 200 μm shallow etched nBn detector operated at 77 K as a function of voltage and TID, is shown in Figure 4.8. One can see that a small, but measurable change on the order of 5 % was observed as the TID was increased up to 200 kRad(Si). Measurement noise, on the order of 0.1 %, was also present as shown in the data below. Similar behavior was observed for the deep etched detector and the variable area diodes. These results suggested that this nBn detector was tolerant of TID and that surface currents, which TID typically enhances due to electron trapping, may have minimal contribution to overall dark-current density. This was later confirmed once again in 2016 on a full Sb-based nBn FPA. [27] In the half decade between this variable area photodiode characterization work being executed and the said FPA study being executed dramatic reductions in dark-current densities occurred and as a result it is prudent to point out that the same result was observed when the Co-60 radiation experiment on an nBn was

executed. It has been found with other IR detector technologies that when the dark-current density is extremely high pre radiation that it is hard to see small changes in dark-current density caused by radiation.
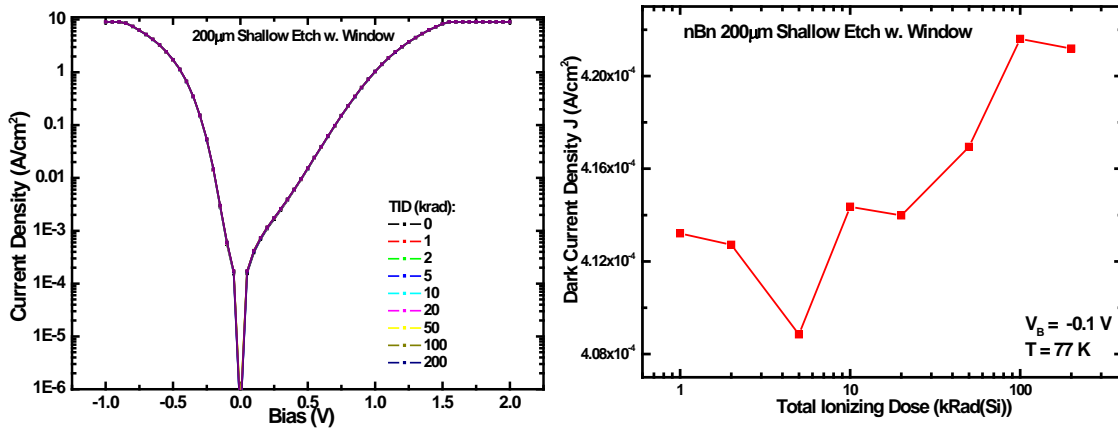
Fig. 4.8: Dark-current densities as a function of bias (Left) and TID with a fixed bias equal to the 100mV (Right) for a 200µm shallow etched device at T=77K.

The dark-current measurements at various biases for the variable area diodes were also compiled as a function of the area-to-perimeter ratios.   This was done for both the deep and shallow etch devices, as shown in Figure 4.9. Examining these results, first and foremost, we see there is again only a small increase in dark-current density, at most bias voltages, for TID up to 200 kRad(Si), suggesting a strong tolerance. Secondly, as expected dark-current density increases with increasing bias for either polarity and with a less rapid increase for positive bias, as is typically observed due to the presence of the barrier.
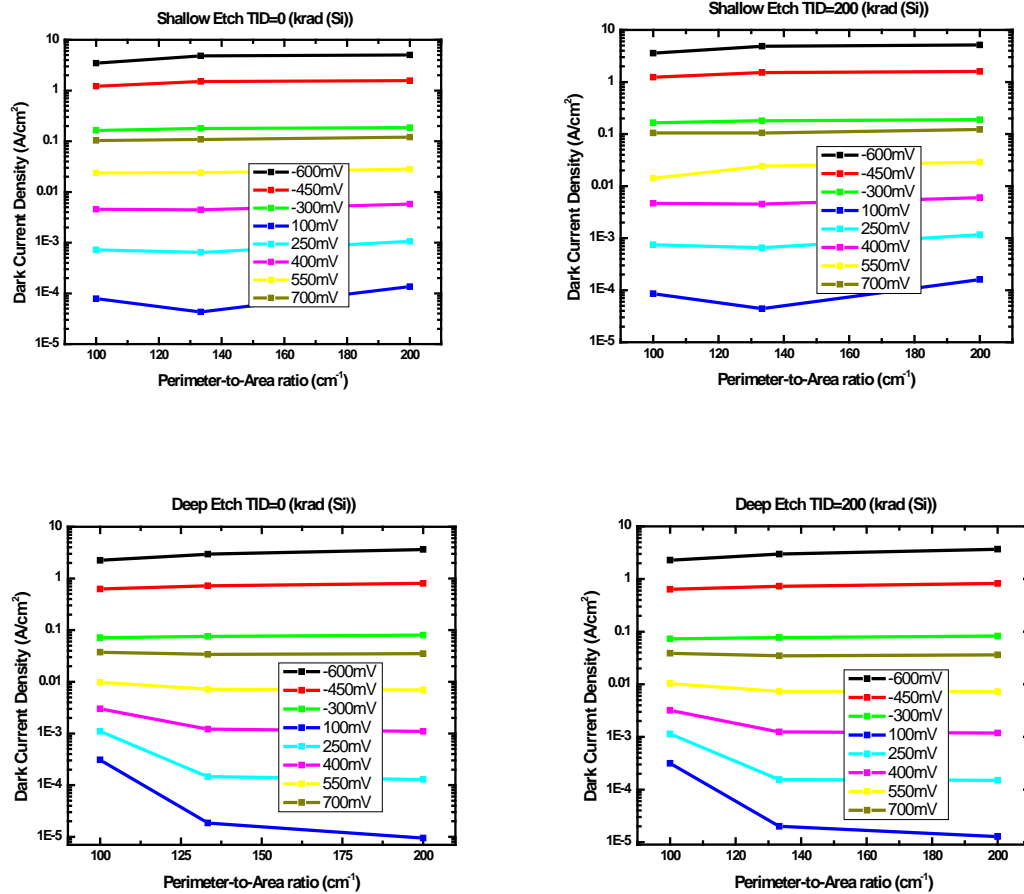
Fig. 4.9: Dark-current densities as a function of perimeter-to-area ratio for shallow (top) and deep (bottom) etched devices at TID = 0 (Left) and TID = 200 krad (Si) (Right).

Finally, these results also suggest that overall this nBn-SLS detector does not appear to suffer from large surface currents that often plague detector technologies, especially at the onset of their development. Rather, a closer look at the plots in Figure 4.9 reveals different behaviors depending on the bias polarity. As bias voltage was made more negative the results begin to show increasing dark-current density as device sized decreased (larger perimeter-to-area ratio) appearing to suggest a small surface current component arises. However, at positive bias voltages the results indicate a decrease in dark-current density

with decreasing device size. The amount of change becomes smaller as the bias is made more positive until the curve has roughly zero slope at V = 700 mV. The source of this unexpected negative slope for positive bias voltages and the overall dependence on polarity is not completely understood. It may reflect a lack of overall device uniformity or not testing large enough perimeter-to-area ratios. However, it may also indicate some kind of built-in surface voltage, due to an n-type surface layer arising in the barrier layer. Further testing would be required to understand fundamentally what is occurring on the sidewalls of the devices.

4.2.2   Co-60 In-situ Step-Wise Optical Characterization Results

This section discusses the optical characteristics of the nBn IR detector. The overall spectral profile of the nBn detector at an operation temperature of 77 K and biased at 100 mV is shown in Figure 4.10. Likewise, the transmission profile of the mid-IR bandpass filter used to measure the responsivity is also shown in Figure 4.10. A bandpass filter with a known spectral response ensures that only a known amount of infrared light is incident on the detector.
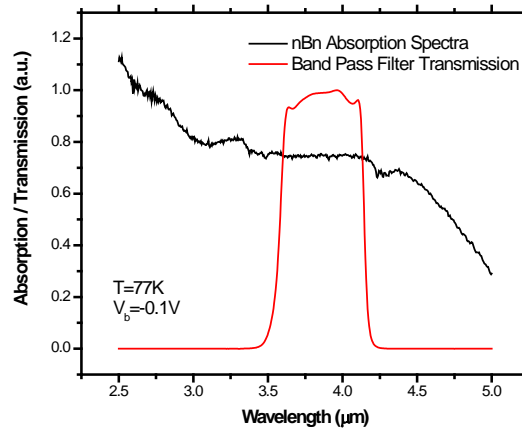
Fig. 4.9: Absorption profile of nBn detector and transmission of band pass filter used for optical measurements.

Using the responsivity equation defined in Chapter 2, the peak responsivity across the 3.6 µm - 4.2µm band of the nBn detector was calculated as a function of the bias applied across the detector. It should be noted that absorption of the nBn detector is very flat over the range of the bandpass filter.

With 100 mV applied across the detector and the peak responsivity was measured to be 296 mA/W. The irradiance light level from the blackbody source that was incident on the detector was estimated to be 9.82×10^{10} photons/sec cm^2. The responsivity of both the shallow and deep etched detectors were measured for each order of magnitude change in TID, namely 0, 1, 10, and 100kRad(Si). As expected, no appreciable change in the responsivity of the detectors was observed as TID increased, as shown in Figure 4.11.
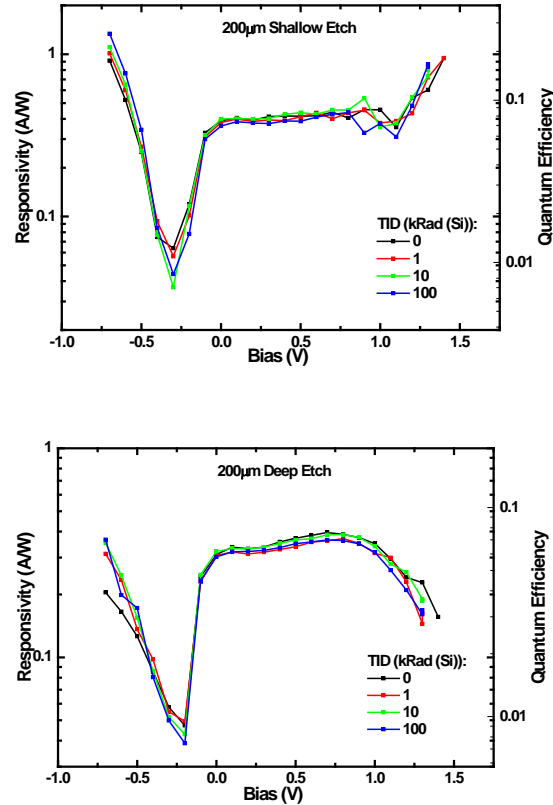
Fig. 4.10: Peak responsivity (3.6µm – 4.2µm range) as a function of bias, shallow etched (left), deep etched (right).

A logical operational bias for this detector occurs at 0.1 V which corresponds to a dark-current density of 420 µA/cm^2 and a responsivity of 296 mA/W across the 3.6 µm - 4.2µm band.

To the best of the authors knowledge this was the first time TID radiation tolerance of a SLS-based nBn architecture infrared detector had been measured. The nBn detector technology was shown to have no significant change in the dark-current density up to a TID of 200 kRad(Si). It was also observed that the dark-current density dependence on perimeter-to-area ratio was a function of bias polarity, although overall surface current effects did not appear significant. Finally, as expected no significant degradation in the

optical responsivity was observed as a function of TID. The next section will focus on effects that proton radiation has on the bulk of the nBn and alike unipolar barrier IR detectors as well as provide additional pre-rad characterization results to help illustrate the state of the technology and potential applicability for strategic applications.

4.3 63 Mev Proton In-Situ Step-wise Irradiation and Characterization of T2SLS and Bulk nBn and alike IR Detectors

In this section, we will discuss the initial finding on the irradiation of a dual band T2SLS based unipolar barrier IR detector specifically focusing on the MWIR. In 2012 this research was published in Applied Physics Letters and was the first refereed publication in this area. [11] Post 2012 exhaustive radiometric and radiation susceptibility characterization of both T2SLS and bulk III-V SWIR, MWIR, detectors has taken place as part of this research portfolio. For the sake of time key research findings that are reflective of the common theme will be included in this dissertation. If the committee or potentially future readers of this Ph.D. dissertation have interest beyond what is included please reference publication identified in chapter one or contact author as there are literally dozens of comprehensive radiometric and radiation tolerance characterization experiments that have been completed as part of this research and can be provided by the Air Force Research Laboratory, Space Vehicles Directorate.

The detectors were held at operating conditions (V_B and T) during proton irradiation. To determine V_B the signal-to-noise ratio (SNR) was estimated by calculating $SNR(V) = I_{ph}(V)/\sqrt{I_{dark}(V)}$, where $I_{ph}(V)$ and $I_{dark}(V)$ are the photo-current and dark-current,

respectively. A V_B was chosen near the maximum SNR, typically in the millivolt range where I_{dark} was diffusion-limited and $I_{ph}(V)$ had plateaued.

The measurements taken before and after each dose step consisted of I_{dark} and I_{ph} measurements from various sized (~ 15 – 800 um) detectors on the same process evaluation chip (PEC). As described in Chapter two $I_{dark}(V)$ was measured with the Dewar aperture shutter held at 77 K using a 2-wire scheme, which was sufficient given the cable series resistances ($\leq$ 5 W) were well below the detector resistances ($\geq$ MW). D.C. source-measure units (SMUs) connected to the top and bottom detector contacts supplied bias voltage and measured equal but opposite currents, confirming the absence of stray leakage paths around each detector.

The I_{ph} measurements were all taken using flood illumination from a well characterized blackbody source passing through an optical chopper, a liquid nitrogen (LN2) cooled narrow band filter (3 – 3.5 μm) well within the linear absorption regime of these detectors and a LN2 cooled 4 mm aperture located inside the dewar and held at 77 K at a fixed distance from the detector (f/# ~ 39). This approach allows for I_{ph} to be accurately measured using an external trans-impedance amplifier (TIA) coupled to a lock-in amplifier referred to the chopper reference signal. Finally, capacitance-voltage measurements were performed on a subset of these detectors during irradiation and confirmed that carrier removal effects were not present. Also, when circumstances permitted, FPAs from the same detector wafers as the PECs measured here were found to have comparable results.

   Flood illumination of the detector has the advantage of allowing for both the bulk quantum efficiency η and a lateral optical collection length L_{oc} to be determined. For a

square, planar-style detector, such as the nBn, whose n-type collector defines the pixel edge length L, I_{ph} can be well estimated by

$$I_{ph} = q\eta E_q A_{Det} = q\eta E_q (L + 2L_{oc})^2, \tag{4.1}$$

where q is the electron charge, E_q is the photon irradiance and A_{Det} is the active detector area.[3] Thus, by measuring I_{ph} of several varyingly-sized pixels, plotting $\sqrt{I_{ph}}$ versus L, and performing a linear fit, both η and L_{oc} can be determined from the fit parameters. L_{oc} should be treated as a phenomenological fitting factor that represents an *effective diffusion length* as other studies have shown L_{oc} is dependent on junction depth, surface recombination velocity and the absorption coefficient, as well as on the real minority carrier diffusion length L_D.[10-11] Judging by the fit qualities of the I_{ph} measurements in these experiments referred to, equation 4.1 appears to be a valid means of assessing the optical response of these detectors even as L_D was expected to decrease below the absorber length L_A with increasing proton fluence Φ_p. Both optical and electrical characterization results for several of the PECs presented in this work were compared to that of companion FPAs and there was strong agreement between those results.

Equation 4.1 should not be misinterpreted to suggest that every electron-hole pair photo-generated within the square detector region of side length $(L + 2L_{oc})$ is simply collected and added to I_{ph}. Rather, collection of photo-generated carriers in detectors is a process typically dependent upon both the drift and diffusion carrier transport mechanisms, although not equally. The latter is ultimately probabilistic and limited by τ_R, as $L_D =$

$\sqrt{D\tau_R}$, where D is the diffusion constant. Thus, 4.1 is only a phenomenological model since some carriers photo-generated from the region beyond the square defined by $(L + 2L_{oc})$ are collected, while some photo-generated well within that region will recombine.

Most relevantly, any reduction in the minority carrier lifetime (τ_R) by proton irradiation means diffusing photo-generated carriers have less probability of being collected. Carriers photo-generated directly within drift regions, however, are still nearly always collected since even after proton irradiation τ_R typically remains $\gg L_A/v_D$, where v_D is drift velocity. This clearly has significant implications on the rad-tolerance of η for different detectors. What's expected and typically observed is that fully-depleted photodiodes show very little degradation of η following proton irradiation as demonstrated in Chapter 3, while detectors, such as the nBn, which rely mainly on diffusion to collect photo-generated carriers from their absorbing layer show much more significant degradation of η.

4.3.1 Radiation Tolerance Characterization of Dual Band InAs/GaSb Type-II Strain-layer Superlattice pBp Detectors using 63MeV Protons

The radiation tolerance characterization of dual band InAs/GaSb Type-II strain-layer superlattice pBp detectors of varying size using 63 MeV proton irradiation are presented. The detectors' mid-wave infrared performance degraded with increasing proton fluence Φ_P up to 3.75 x 10^{12} cm^{-2} or, equivalently, a total ionizing dose = 500 kRad(Si). At this Φ_P, a ~31% drop in quantum efficiency η, ~2 order increase in dark-current density J_D and, consequently, > 1 order drop in calculated detectivity D^* was observed. Proton damage

factors were determined for η and D^*. Arrhenius-analysis of temperature-dependent J_D measurements reflected significant changes in the activation energies following irradiation.

Subjecting this pBp architecture IR detector to proton irradiation is expected to lead to both TID and displacement damage effects, both of which occur on orbit. TID effects occur as incoming protons lose their kinetic energy to ionization of the detector material's constituent atoms and the additional charges become trapped in oxide layers or surface traps. This additional charging may result in flat-band voltage shifts and increased surface leakage currents. Displacement damage effects result from the occasional non-ionizing energy loss of an incoming proton due to elastic or inelastic scattering with an atomic nucleus that is sufficient to knock the atom from its lattice site and generate vacancy-interstitial pair, anti-sites, and defect complexes. [28] These defects may manifest in lower η, due to the consequent reduction in minority carrier lifetime τ, and higher J_D, due to the SRH mechanism. The proton fluence at 63 MeV required to alter the background doping levels such that the fundamental Auger mechanism is enhanced is expected to be order's higher than the fluence levels used here. As with the HgCdTe characterization the first step to characterizing a detector's radiation tolerance was measuring η and J_D as a function of Φ_P, with all irradiation and measurements conducted at the detector's expected operating temperature and bias. The importance of the latter is vividly illustrated in a 1-2 MeV proton irradiation study of Sb-based T2SLS photodiodes where the detectors were unbiased and at 300 K during irradiation, which presumably precluded observing the effects of ionization and lower energy defects due to displacement damage, both of which were are expected to anneal at room temperature. [29, 30] Thermal annealing of radiation effects at 300 K was shown. [30] and was likewise observed during this experiment on the T2SLS detectors.

Using η and J_D to also estimate the detector sensitivity, expressed early in this dissertation by shot-noise-limited D^*, is then done to illustrate which of the two dominates the change in overall performance.

Radiation tolerance can be further characterized by calculating the *damage factor K_X* or the rate of degradation for each performance metric X (e.g. $X = \eta, J_D, D^*$, etc.) from the performance measurements taken versus fluence. For comparison purposes, however, it is worth noting that these K_X-metrics may be a function of a detector's architecture, material composition, growth method, processing, passivation, etc. and are thus entirely specific to that particular detector. K_X's are also specific to the particle type and energy of the irradiation. In fact, with a known energy-dependence $K_X(E)$ predictions of the expected on-orbit degradation ΔX ideally become possible, according to equation 4.1 where $\frac{d\Phi_P}{dE}$ is an expected orbit's differential proton fluence spectrum. [31]

$$\Delta X = \int_{E_1}^{E_2} K_X(E) \frac{d\Phi_P}{dE} dE, \tag{4.1}$$

The dual-band, InAs/GaSb T2SLS pBp detectors used in this study were previously fully described. [32] Summarizing those details, the pBp detectors are grown via molecular beam epitaxy on GaSb substrate material and include two 2 μm, p-type, Be-doped ~1 x 10^{16} cm^{-3}, InAs/GaSb SLS absorbing layers designed for mid-wave and long-wave infrared (MWIR and LWIR) response that are separated by a similarly doped InAs/AlSb barrier layer. Samples with square mesa devices varying in mesa edge length L from 45 - 145 μm and etched through both absorber layers to the bottom contact layer were then fabricated from the material by standard photolithography and wet-etching practices and then

wirebonded to 68 pin leadless chip carriers for cryogenic testing purposes. FTIR absorption measurements at forward- and reverse-bias showed the zero-response cutoff wavelength λ_c in the MWIR and LWIR were 7.8 and 12 µm at 80 K, respectively. However, only the MWIR optical results are discussed in this dissertation as the low LWIR signal level prevented a completely reliable radiation tolerance characterization for that band.

The proton irradiation was once again performed at the Crocker Nuclear Laboratory at the University of California, Davis, using their 76" isochronous cyclotron, which can provide protons with energies up to 68 MeV. [20] The detectors were at their nominal operating conditions, biased at $V_B = +.1$ V and $T = 80$ K, during proton irradiation. Photocurrent and dark-current measurements were performed on $L = 45$, 65, 85 and 145 µm mesa devices at TID = 0, 2, 5, 10, 20, 50, 100, 200, and 500 kRad(Si), as well as following a post-rad, 2 day, 300 K thermal anneal.

Photocurrent measurements were taken with the detectors held at the MWIR operating bias, $V_B = +.1$ V applied to the top of each mesa, using standard a.c. lock-in technique at $f/\# \sim$ 40 and a blackbody source at $T_{BB} = 900$ K. The blackbody output was passed through a room-temperature 3.5 - 4.2 µm IR band-pass filter and a KRS5 dewar window, followed by a 4 mm pinhole held at 77 K within the dewar, leading to an incident photon flux $E_Q =$ 3.1 x 10^{14} ph/sec-cm^2 at peak wavelength $\lambda_p \sim 3.9$ µm.

Dark-current measurements were then performed using a standard d.c. source-measurement unit with a 77 K shutter blocking the pinhole as previously described.

Finally, temperature-dependent measurements of J_D were performed from $T = 77$ K to 300 K at the MWIR operating bias $V_B = +.1$ V and an Arrhenius-analysis was performed to determine E_A and thus, gain some insight regarding the dark-current limiting mechanism.

Measurements of the detector's η at $\lambda_p \sim 3.9$ μm, derived from the I_p-measurements, as function of Φ_P and post-anneal are shown in Fig. 1. In the pre-rad condition, as Figure 4.10 shows, $\eta \sim 29\%$, which roughly matches others reported results. [32] The η was then observed to degrade roughly linearly with increasing Φ_P down to $\sim 21\%$ at 3.75 x 10^{12} cm^{-2} or, equivalently, TID = 500 kRad(Si), a 28% change in η. From the slope of the data in Fig. 1, the MWIR η damage factor was found to be $K_\eta = -2.14$ x 10^{-14} e-cm^2 /ph-H$^+$. Following irradiation the detector temperature was raised to 290 K for ~ 48 hrs and then re-measured, whereby η recovered to $\sim 28\%$. As proton irradiation is known to generate bulk defects, and thereby reduce τ and diffusion length $L_D \propto \sqrt{\tau}$, the drop in η in Figure 10 suggests $\eta \propto 1 - e^{-\alpha L_D}$, where α is the absorption coefficient and $L_D < 2$ μm, the thickness of the MWIR absorbing layer, since α is not expected to change with fluence. A perimeter-to-area (P/A) analysis of these results, which suggests some surface-related recombination is also occurring, will be discussed in a forthcoming publication. [33]
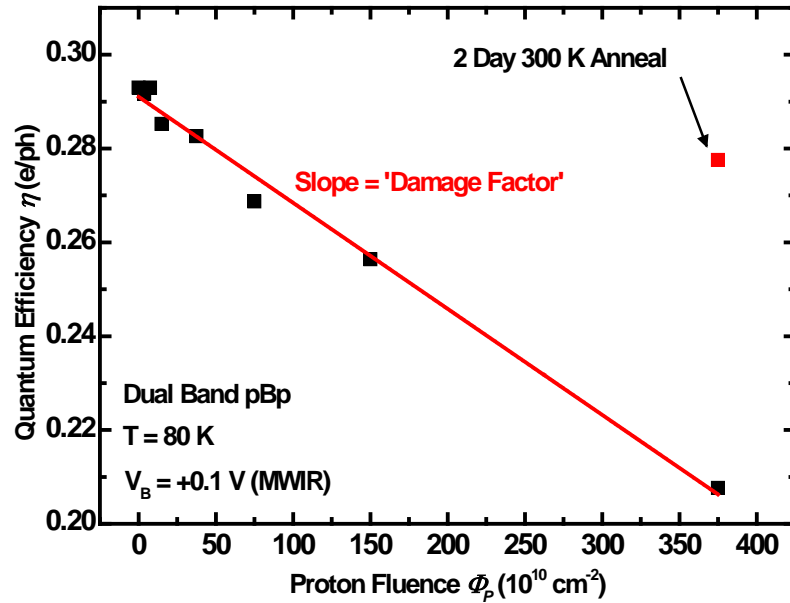
Fig. 4.10: η at $\lambda_p \sim 3.9$ μm plotted as a function of Φ_P ranging from 0 to 3.75 x 10^{12} cm^{-2} and post-anneal. A $K_\eta = -2.26$ x 10^{-14} e-cm^2 /ph-H$^+$ was calculated from the linear fitting of the measured data.

Measurements of J_D at $V_B = +.1$ V as a function of F_P and post-anneal for each detector are shown in Fig. 2, while the inset shows the measured I-V relationship for the 45 μm device under similar conditions. These results all show a monotonic increase in J_D with increasing F_P, up to 3.75 x 10^{12} cm^{-2}, at which point a roughly two order increase in J_D was observed. For $F_P < 10^{12}$ cm^{-2}, however, the rate of increase of J_D appears to depend on L, which is indicative of surface currents. A perimeter-to-area analysis of J_D to investigate the surface current effect will also be discussed in the other forthcoming publication. [33] For $F_P > 10^{12}$ cm^{-2} the change in J_D appears to saturate slightly; however, this effect requires more investigation and may be transient. Following irradiation, two consecutive thermal anneals, at 240 K for 2 hrs and at 300 K for 48 hrs, were conducted. Following each a ~ 25% and ~ 50% reduction in irradiation induced J_D were observed.
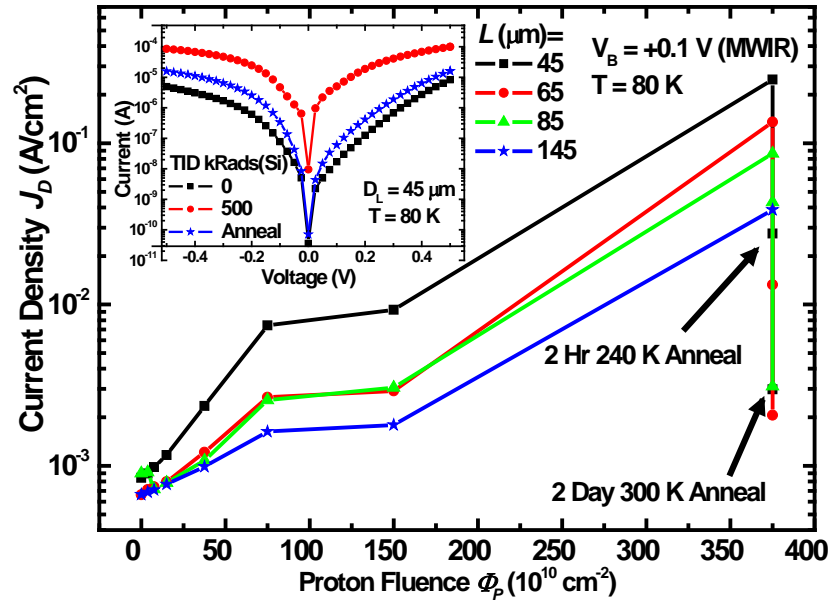
Fig. 4.11: J_D measured for the L = 45, 65, 85, and 145 µm detectors at F_P ranging from 0 to 3.75 x 10^{12} cm^{-2} and post-anneal. Inset: I-V relationship for 45 µm detector in pre-rad, post-rad and post-anneal conditions.

To approximate the expected reduction in sensitivity with increasing Φ_P, the shot-noise limited D^* for the 45 µm detector was then calculated from the results in Figure 4.11 and Figure 4.12 using the expression $D^* = R/\sqrt{(2qJ + (4k_BT)/R_dA_d)}$, where $R = \eta q/(hc/\lambda_p)$ is the detector responsivity, k_B is Boltzmann's constant, R_d is differential resistance, A_d is the detector area, h is Planck's constant and c is the speed of light. While this method of calculating D^* was discussed early in this chapter to often be of limited utility in accurately describing the detector's sensitivity, due to the omission of additional noise sources as described in Reference [24], as it is used here it serves as a good means of estimating the sensitivity's dependence on Φ_P. A plot of D^*, again as function of Φ_P and post-anneal, is given in Figure 4.12. Here, D^* is predicted to degrade over an order of magnitude from its pre-rad value of 4.86 x 10^{10} cm Hz$^{1/2}$/W down to 2.12 x 10^9 cm Hz$^{1/2}$/W in post-rad. Figure 4.12 also includes plots of D^* calculated with either η or J_D held fixed

at its pre-rad value. These two plots show the dependence of D^* on Φ_P is completely dominated by changes in J_D. Post-anneal, only a 49% drop in D^* is calculated compared to the pre-rad condition. For $\Phi_P < 100 \times 10^{10}$ cm^{-2}, a D^* damage factor $K_{D*} \sim 4.53 \times 10^{-2}$ cm^3-Hz$^{1/2}$/W-H$^+$ was determined.
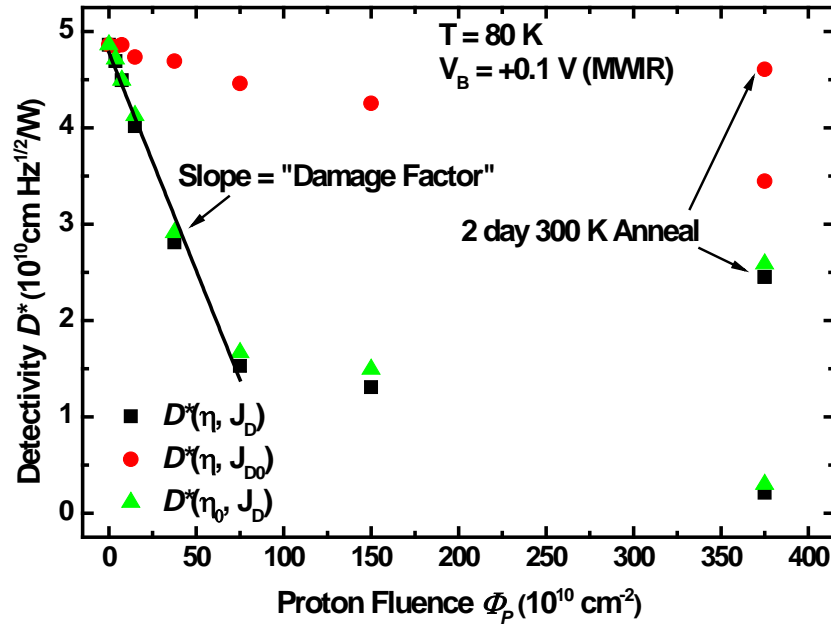
Fig. 4.12: Shot-noise limited D^* (black squares) for 45µm mesa detector with F_P ranging from 0 to 3.75 x 10^{12} cm^{-2} and post-anneal and with h (red circles) and J_D (green triangles) fixed to its pre-rad values. The linear fitting had a slope of $K_{D*} \sim 4.53 \times 10^{-2}$ (cm^3 Hz$^{1/2}$/W H$^+$).

Three sets of temperature-dependent J_D-measurements, reflecting the pre-rad, post-rad and post-anneal conditions, for the 45 µm mesa detector at $V_B = +.1$ V are shown in Figure 4.13. Here the pre-rad and post-anneal results clearly show two distinct regions of T-dependence, with crossovers at $T = 115$ K and 93 K, respectively, while for the post-rad data this is much less clear. From the Arrhenius-analysis of the pre-rad and post-anneal plots in Fig. 4 an $E_A \sim 155$ meV was extracted for the high-T region, which directly corresponds to the measured $\lambda_c \sim 8.1$ µm for this device and indicates diffusion-limited J_D

in this region. In the low-T region, slightly different $E_A < E_{gap}/2$ and amplitudes were determined for the pre-rad and post-anneal data. These differences suggest J_D is SRH-limited with additional irradiation-induced defects that remained non-annealed affecting the post-anneal data. The post-rad J_D data had an E_A as low as 20 meV up to $T \sim 115$ K and slowly increasing until $T \sim 175$ K, when it begins to show a similar high-T dependence as the other traces, presumably due to the combined effects of thermal annealing and enhancement of the diffusion-limited J_D with T. The low E_A and high amplitude for the post-rad J_D at $T < 175$ K, in comparison with the other traces, most likely reflects surface-limited behavior stemming from TID effects as the dark-current nearly recovers to its pre-rad value following the 300 K thermal anneal.
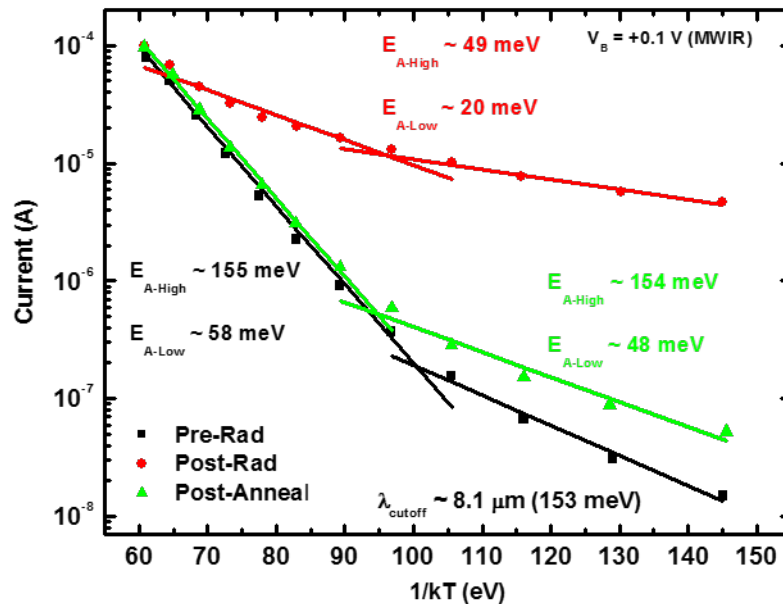
Fig. 4.13: Temperature-dependent J_D measurements on the 45µm detector in the pre-rad, post-rad and post-anneal conditions illustrating changes in E_A that reflect an increase (decrease) in near mid-gap defect density post-rad (post-anneal).

This was the first time a radiation experiment had been performed on a pBp detector employing a T2SLS absorber was performed using 63 MeV proton irradiation. Measurements of η and J_D reflected a degradation of the detector performance with increasing Φ_P that would necessarily result in > 1 order drop in the calculated D^* at $\Phi_P =$ 3.75 x 10^{12} cm^{-2}, mostly from the increase of J_D with Φ_P. Post-anneal, both η and J_D recovered to a large degree to their near pre-rad values. An Arrhenius-analysis of temperature-dependent J_D-measurements reflected significant changes in E_A and amplitudes following irradiation, which suggested a large increase in the surface current, most of which recovered following a 48 hr, 300 K thermal anneal, and a smaller increase in bulk dark-current, which did not anneal out, following irradiation.

4.3.2 Radiation Tolerance Characterization of Unipolar Barrier Architecture Detectors with Type-II Strain-layer Superlattice & Bulk III-V Absorbers Using 63MeV Protons

This section of the dissertation is going to provide key results from radiometric characterization results of several nBn and alike unipolar barrier MWIR detectors that utilize T2SLS and bulk absorbers. This by no means is meant to represent all of the data that was collected but is an attempt to clearly illustrate the underlying radiometric results that were common across unipolar detector architecture and III-V absorber employed.

A MWIR nBn detector using MBE growth and processing techniques reflective of the state of the IR industry was in-situ step-dosed with 63MeV protons up to a equivalent Total Ionizing Dose of 100 krads(Si). This particular test article had a large range of variable area photodiodes such that in-depth exploration of dark and photocurrent aspects could be explored. The degradation of QE as function of proton Fluence is shown in Figure 4.14. The optical flux on the part was 2.13 x 10^{14} ph/s and a band pass filter centered at 3.7µm was used. The K_{QE} was found to be 1.15 E-13 cm^2 after a 300K thermal anneal the QE returned to TID 50 levels.
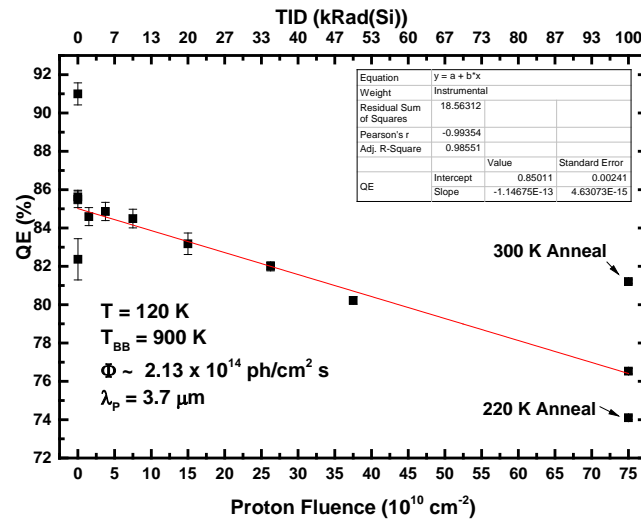
Fig. 4.14: QE vs proton fluence for a MWIR nBn detector and fit to extract K_{QE}

The lateral optical collection length was likewise measured as a function of proton fluence and a fit of $1/L_D^2$ that resulted in K_{LC} ~ 1.3 x 10^{-13}. Once again after a 300K thermal anneal the L_D returned to near TID 50 levels as shown in Figure 4.15
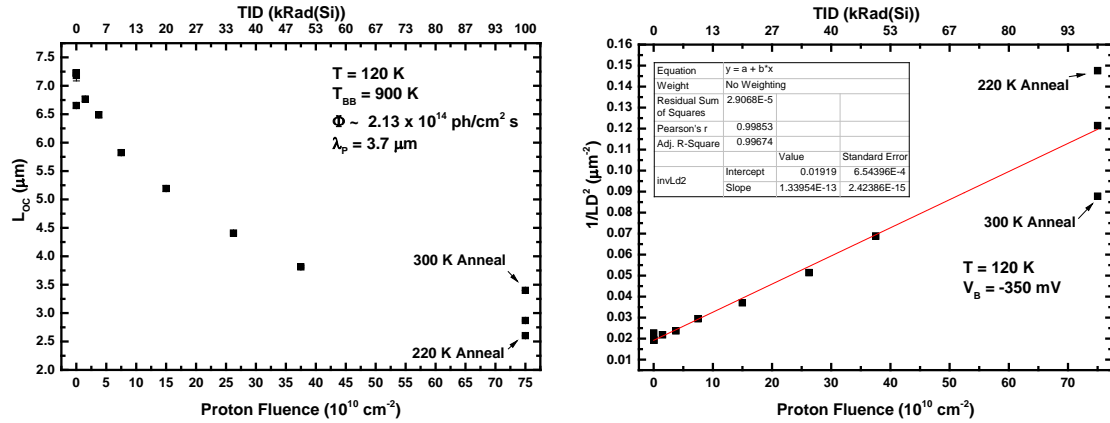
Fig. 4.15: L_D vs proton fluence for a MWIR nBn detector and fit to extract K_{LD}

IVs were taken as a function of proton fluence as shown in Figure 4.16 and a break down was observed at ~500mV and appears that diffusion limited, Generation Recombination, and tunneling limited regimes were all present. There was an increase in dark-current with proton dose and the dark-current was found to of decreased with both a 220K and 300K thermal anneal. Plotting the J_D as a function of proton fluence for four different photodiodes it was found that the dark-current density increased nearly 30X pre tad to TID 100 krad(Si). Fitting as described previously K_{Jdark} was found to be 3.97E-18 A/proton. After a 300K thermal anneal the dark current density was found to cover 43%. It should be noted that at 120K operating temperature and 4.9µm cut-off material the Rule '07 indicates that the dark-current density should be ~3.7nA/cm^2. J_D for the nBn detector under test was found to be ~3 orders of magnitude higher.
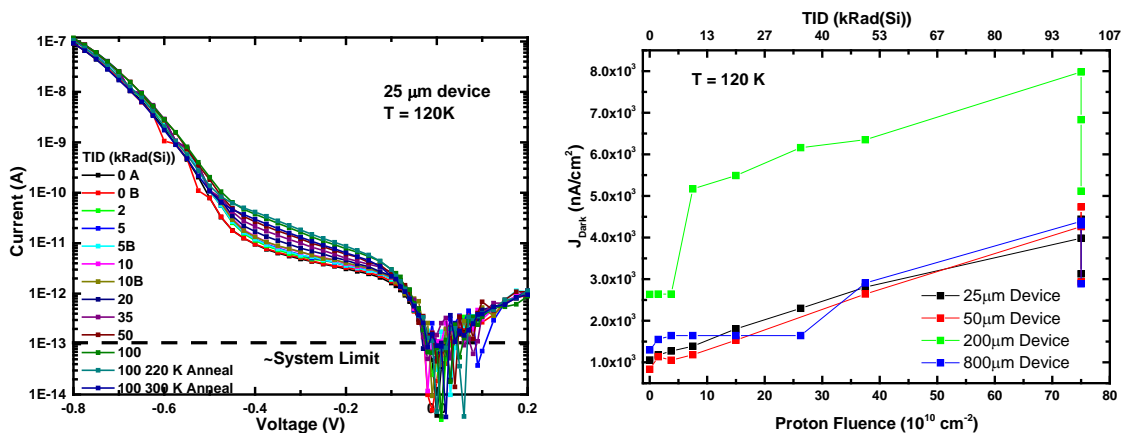
Fig. 4.16: IVs and dark-current density vs proton fluence for a MWIR nBn detector

The IVs as a function of temperature were taken for 25 and 100µm square photodiodes pre-rad, post-rad, and post anneal and are shown in Figure 4.17. Generation-recombination currents were evident below 160K and tunneling was present at detector biases below -400mV.
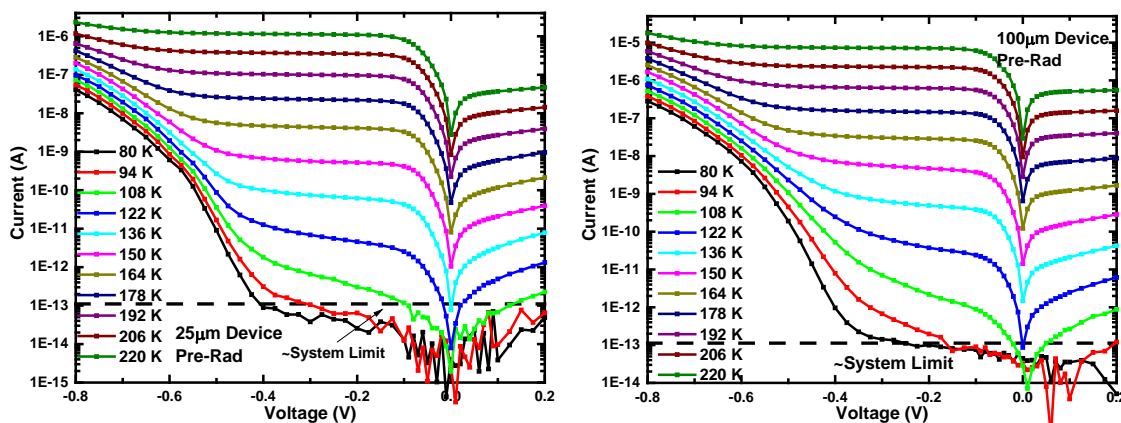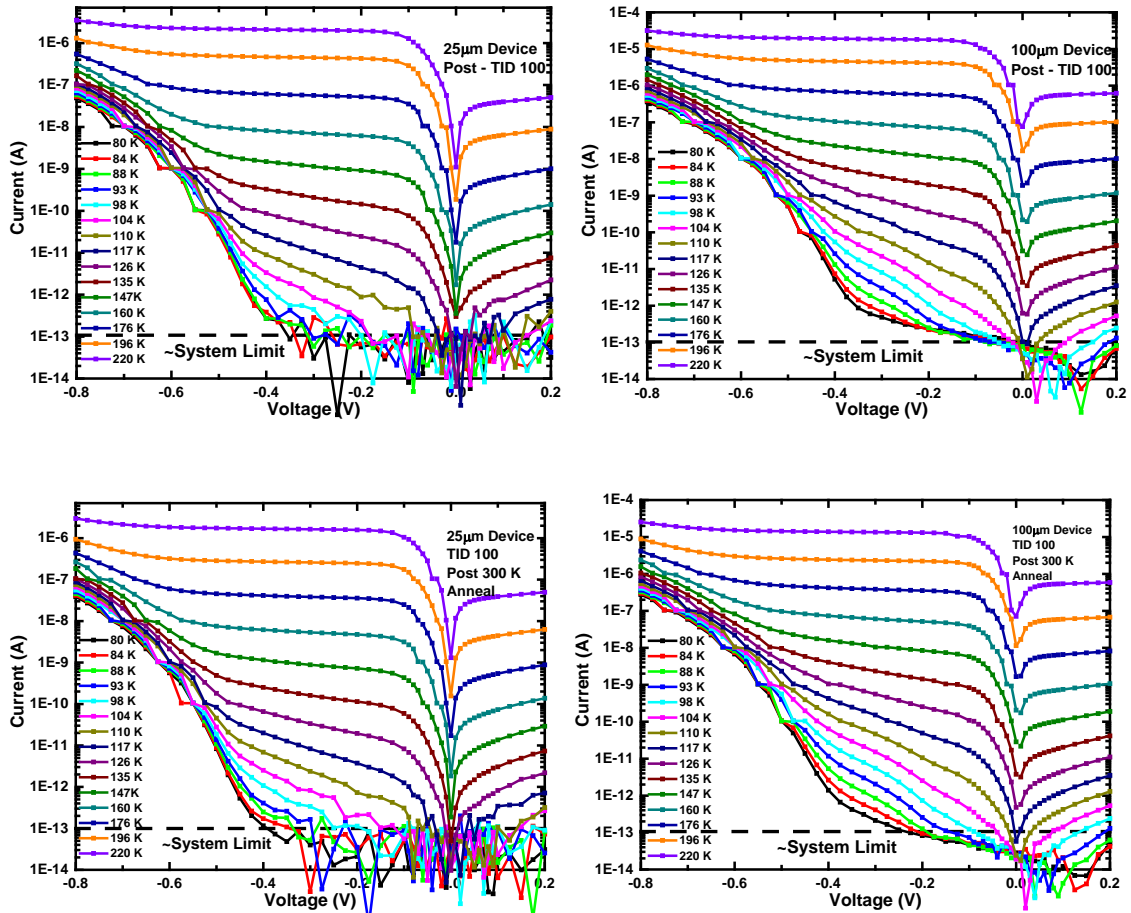
Fig. 4.17: IVs pre-rad, post 100 krad(Si), post 300K anneal for 25µm and 100 µm MWIR nBn detector.

Pulling the dark-current density from the IVs at the operating bias an Arrhenious-analysis was performed on a 25, and a 100 µm nBn photodiode as shown in Figure 4.18. An average activation energy pre rad was found to be 245meV (λ_A=5.07µm), post 100 krad(Si) dose equal to 227meV (λ_A=5.47µm), and post a 300K anneal equal to 221meV (λ_A=5.62µm). The diffusion limited regime wasn't found to change appreciably with dose.
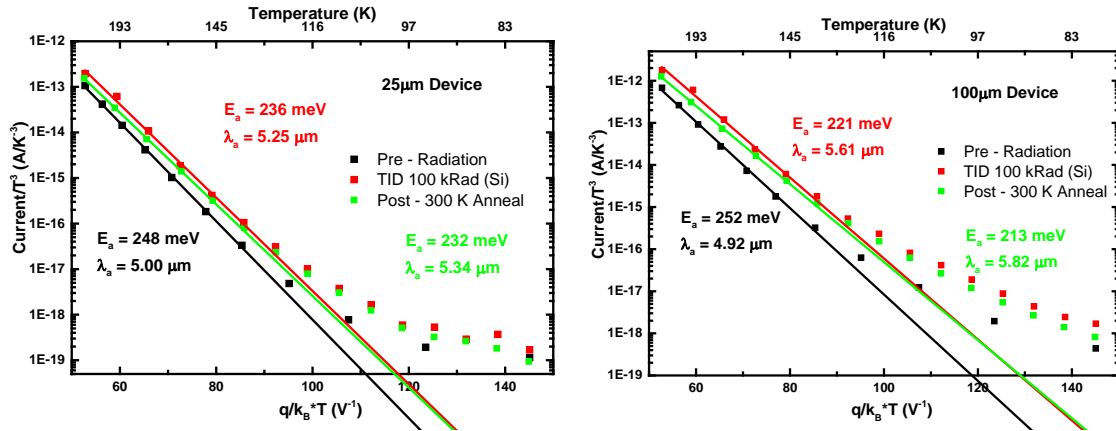
Fig. 4.18: Arrhenius-analysis of a 25 and 100µm MWIR nBn detector pre-rad, post 100 krad(Si) TID, and post 300K anneal

The SNR as defined previously was plotted for the 25 and 50 µm detectors as a function of TID and is shown in Figure 4.19. The peak SNR degraded by 341% and 306% for the 25 and 50 µm devices respectively. No difference in the peak SNR was observed with different device sizes.
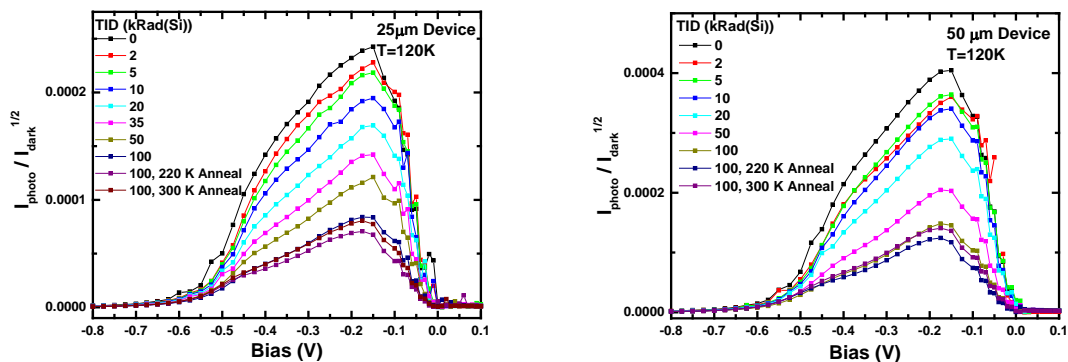
Fig. 4.19: SNR plot for 25 and 50µm MWIR nBn detector as a function of dose and 300K anneal.

During all of the radiation experiments a capacitance voltage plot was collected for the largest available device as a function of dose and is shown in Figure 4.20. There was no change in the profile of the CV in this experiment or any of the radiation experiment performed on the unipolar barrier IR detectors using III-V T2SLS and bulk absorbers. The slope was constant for all of the CV curves indicating no sign of carrier removal being introduced.
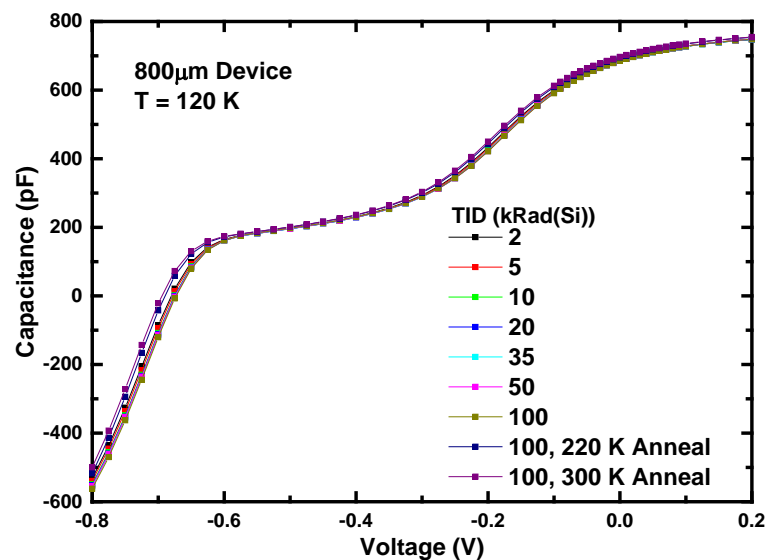
Fig. 4.20: CV for 800µm MWIR nBn detector as a function of dose and 300K anneal.

The characterization suite that was illustrated in 4.3.2 was executed 19 times during the executing of the underlying research presented in this dissertation and continues at the present date and undoubtedly will continue in the future. Given the technology shortfalls demonstrated in terms of performance degradation when irradiated it was naturally desired to iterate on detector designs to attempt to build a III-V based unipolar barrier detector where the QE and J_D rate of degradation was less than what was observed and previously

just shown. During the development of these unipolar barrier IR detectors it was observed that every 100nm that the cut-off wavelength was pushed to the right that nearly an order of magnitude higher J_D was produced, with time J_D was attenuated. Given the fluctuation in cut-off wavelength and operating temperature it was extremely difficult to determine if progress improving the radiation tolerance of the material was being made.

5 Aggregate Unipolar Barrier IR Detector Damage Factor Analysis & Interpretation

In chapter 3 and 4 we discussed results for both HgCdTe and T2SLS/bulk Sb based nBn and alike unipolar detectors performance in clear, gamma, and proton environments. Building from this in this chapter will include an examination of the collective results from all of these experiments quantifying the performance degradation rates of III-V-based, unipolar barrier infrared detectors with various designs, cutoff wavelengths and operating conditions due to 63 MeV proton irradiation is presented. Empirical relationships were established between the radiation damage factors for dark current density, lateral optical collection length, and quantum efficiency and the detectors' cutoff wavelength and operating temperature. Fitting the dark current density damage factor's empirical relationship reflected these detectors' tendency to remain diffusion-limited during irradiation, which was previously established using Arrhenius-analysis of the post-irradiation, temperature-dependent dark current measurements on each. Collectively, the results affirmed the performance degradation stemmed from a reduction of the minority carrier recombination lifetime via generation of additional defects by proton-induced displacement damage. For comparing detector's rad-tolerance, the results indicated that damage factors alone are not ideal, but their empirical relationships may serve as heuristics in this role.

5.1 Introduction

Two distinct damage mechanisms, ionization damage and displacement damage, account for the performance degradation due to proton irradiation of a detector array. Ionization damage, or so-called total ionizing dose (TID) effects, occurs as incoming rad-particles, incident on the FPA, give up their energy to ionizing additional electron-hole pairs. Some of these excess carriers can become trapped in surface states and defect levels of the dielectric materials used for passivation and as gate oxide layers. This excess trapped charge typically manifests as excess surface-currents in the detector pixels. TID effects are thus primarily affected by the surface passivation and changes to passivation thickness, quality or type can reduce or eliminate TID effects.

Displacement damage results when incoming irradiation particles' energy is lost to Coulomb scattering of lattice atoms off their lattice sites. This generates additional vacancy-interstitial pairs in the detector's absorbing layers that can act as electrically active defects where electron-hole recombination can occur. The additional defect generation shortens the detector material's minority carrier recombination lifetime τ_R, which in turn leads to increased dark current, decreased responsivity and degraded uniformity. [34] Unlike TID effects, displacement damage is expected to be entirely fundamental to the detector's bulk material and design; it cannot be mitigated by an external means such as better passivation. A material's defect introduction rate due to irradiation, which is a measure of displacement damage, is expected to be a function of the detector's material parameters, as well as temperature, irradiation species and energy. Detector design (i.e. pn-junction versus nBn, # of layers, etc.) may also impact the defect introduction rate, as defects may diffuse after their formation to layer interfaces and generate larger complexes.

HgCdTe photodiodes are still the incumbent detector for space-based imaging due to their high performance. The radiation tolerance of HgCdTe-based FPAs and detectors has been the subject of previous study. [31, 35] As their radiometric performance has improved, newer infrared detector materials and designs, such as III-V-based, type II superlattices (T2SLS) photodiodes and unipolar barrier detectors have also received significant attention. Most of these studies, however up until this dissertation resarch, focus only on a single FPA or detector. They are also performed with different irradiation species and energies. This variation makes it very difficult to really draw any broad conclusions about the state of III-V detector technology in terms of rad-hardness for space imaging.

In this chapter an examination of the aggregate damage factor results from rad-tolerance experiments on several different III-V-based detectors is presented. The detectors all incorporated various unipolar barrier architectures (nBn, C-BIRD, pCBn, etc.) with bulk InAs, InAlAs/InAs T2SLS, etc. absorbing layers as described further below. The aggregate results indicated the following: (1) robust trends in the detectors' dark current, lateral optical collection length and quantum efficiency radiation damage factors with cutoff wavelength and operating temperature sufficient for empirical relationships to be established for them; (2) as was previously established using Arrhenius analysis of post-irradiation, temperature-dependent dark current measurements, the dark current of these detectors remained diffusion-limited following irradiation, according to a fitting of the semi-log plot of their dark current damage factors, which thereby provided more evidence that the performance degradation resulted from the additional defects generated by proton-induced displacement damage and the consequent reduction of τ_R; and (3) for comparing these detectors' rad-tolerance, damage factors on their own are not ideal, but their empirical

relationships can still serve as heuristics. These empirical relationships are thus sufficient to discern whether any one specific detector design far exceeds another's and, most importantly, allow for comparisons with future detector designs or detectors based on alternative material systems such as HgCdTe and InSb. This approach is thus vaguely similar to the establishment of "Rule '07" as a heuristic for comparing the dark current densities of state-of-the-industry HgCdTe detectors. [21]

5.2 Overarching Experiment

With the relatively recent introduction of two key technologies, the unipolar barrier detector architecture, or nBn, in and Ga-free T2SLS in, the performance of III-V-based, infrared detectors has reached new levels and they are once again being considered as an alternative to HgCdTe for space-imaging.[6, 36] These developments had thus prompted rad-tolerance studies of the new III-V-based, Ga-free unipolar barrier detectors as presented in Chapter 4. This chapter is based on the product of comparing all the results in Chapter 4 with the original goal of identifying the most rad-tolerant detector materials and designs. The detectors used for the rad-tolerance experiments discussed herein were provided by various manufacturers, government labs, and academic intuitions including the University of New Mexico. The only defining characteristics of these detectors were their use of one or more barrier layers that block carriers in only one band (e.g. an electron barrier in conduction band with a zero valence band offset) and a Ga-free absorbing region. Otherwise, they had various cutoff wavelengths ($\lambda_c \cong 4 \leftrightarrow 5.6$ mm), operating temperatures ($T \cong 100 \leftrightarrow 150$ K) and operating reverse bias voltages ($V_B \cong |-0.5| \leftrightarrow |-0.3|$ V). In all cases, the actual design specifics (i.e. layer widths, alloy concentrations,

etc.) for these detectors were not made available to the authors, which is common practice in the infrared detector community. While this precludes comparisons of the experiment results as a function of varying detector designs, it still allows for empirical relationships to be determined between the measured rad-tolerance parameters and with $(\lambda_c T)^{-1}$

5.3 Theory Degradation Rates and Damage Factors

As previously introduced in Chapters 3 and 4 degradation rates of each measured parameter of the detector's performance (J_d, L_{oc}, η) are determined by plotting them as a function of Φ_p and characterizing the changes. When the change in parameter X appears roughly linear with Φ_p, which may be true only on average or for only a certain fluence range, then a so-called damage factor K_X can be defined such that

$$X = X_0 \pm K_X \Phi_p , \tag{5.1}$$

where X_0 is the un-irradiated value of the performance aspect and the $\pm$ is determined by the expected change (e.g. $+$ for J_D, $-$ for η). Damage factors are assumed to be related only to changes due to the effects of displacement damage, not ionization damage, and are dependent on the proton energy E. The main intent for finding the damage factor is to predict the on-orbit change in X; [31, 37, 38] however, measuring K_X as a function of E is prohibitively difficult. Rather, if K_X measured at a few proton energies (e.g. $E_1, E_2,..$) can be shown to be proportional to the calculated energy dependence of the non-ionizing energy loss $NIEL(E)$ for the detector's material then $R = K_X(E_1)/NIEL(E_1)$ and $NIEL(E)$ can be used to estimate the expected on-orbit change in X due to protons

according to

$$\Delta X = R \int_{E_1}^{E_2} NIEL(E) \frac{d\Phi_p(E)}{dE} dE \tag{5.2}$$

where $d\Phi_p(E)/dE$ is the predicted on-orbit differential proton spectrum. [39]

Examining whether K_X of different detectors may also be used to compare their rad-tolerance was also part of this investigation. First, this would only be strictly true if several other conditions that may impact damage formation were kept constant. Here, the differences between rad-tolerance experiments were minimized to the maximum extent possible to meet this objective, with an equivalent 63 MeV proton energy used in every experiment and constant operating conditions (V_B and T) during the course of each experiment. A connection between K_X and the level of displacement damage can be established by assuming a linear increase in the defect concentration N_T with Φ_p, which the data from these experiments supports. Recall that when dominated by SRH recombination and assuming a single active recombination level, τ_R is related to N_T according to

$$\frac{1}{\tau_R} = N_T(\Phi)\sigma v_{th}, \tag{5.3}$$

where σ is the minority carrier capture cross-section, v_{th} is the carrier thermal velocity equal to $\sqrt{3k_B T/m^*}$, k_B is Boltzmann's constant and m^* is effective mass. With these assumptions then, τ_R depends on Φ_p according to [37, 38]

$$\frac{1}{\tau_R} = \frac{1}{\tau_{R0}} + K_{1/\tau_R}\Phi_p \tag{5.4}$$

where $1/\tau_{R0} = N_T(0)\sigma v_{th}$ and K_{1/τ_R} is related to the material's defect introduction rate $dN_T/d\Phi_p$ by

$$K_{1/\tau_R} = \sigma v_{th} \frac{dN_T}{d\Phi_p}. \tag{5.5}$$

The σv_{th} term in equation 5.5 is expected to be constant for the fluence ranges of interest and thus K_{1/τ_R} is proportional to the material's fundamental rad-tolerance, defined by $dN_T/d\Phi_p$. As the other performance parameters directly relate to τ_R, their expected dependence on $dN_T/d\Phi_p$ can and will be detailed.

5.4 Dark Current Density Damage Factor

J_D's relationship with Φ_p is complicated by the different mechanisms that can contribute to J_d at the same time (e.g. shunt currents may potentially arise from ionization damage and lateral collection may play a role depending on the size of the detector). Thus, only some ideal limiting cases for bulk J_d are considered below, which illustrate several of the observed trends in the rad-tolerance experiments on unipolar barrier detectors.

An ideal nBn detector with a completely field-free, narrow-gap absorption layer is considered first. Here, J_D will be diffusion-limited, but τ_R is dominated by SRH-recombination, according to equation 5.3, and thus J_D is still limited by N_T. In the $L_D \gg L_A$ regime, which is expected for unipolar barrier detectors at lower Φ_p, where N_T is expected to its lowest, the diffusion-limited, dark current density J_{Diff} is given by

$$J_{Diff} = \frac{q n_i^2 L_A}{N_D \tau_R} = \frac{q n_i^2 L_A N_T(\Phi) \sigma v_{th}}{N_D}, \tag{5.6}$$

where L_A is the absorber thickness, n_i is the intrinsic carrier concentration and N_D is the

doping concentration. In this limiting case, a linear increase in J_{Diff} with increasing Φ_p is expected, similar to equation 5.4, where $K_{J_{Diff}}$ is related to $dN_T/d\Phi_p$ according to:

$$K_{J_{Diff}} = \frac{qn_i^2 L_A}{N_D}\sigma v_{th}\frac{dN_T}{d\Phi_p}. \tag{5.7}$$

When $L_D \ll L_A$, a regime to which the unipolar barrier detector is ultimately expected to transition to as N_T increases with increasing Φ_p, the diffusion-limited J_D is now expected to follow the infinite substrate width solution, given by

$$J_{Diff} = \frac{qn_i^2}{N_D}\sqrt{\frac{D}{\tau_R}}, \tag{5.8}$$

where D is the diffusion constant given by $D = k_B T\mu/q$ and μ is the minority carrier mobility. J_{Diff} would now have a $\sqrt{\Phi_p}$-dependence since a linear increase in $1/\tau_R$ with increasing Φ_p is still expected. Formally, damage factor analysis typically only considers linear changes with Φ_p and thus, formally-speaking, it is $\left(J_{Diff}\right)^2$ that should be examined for $L_D \ll L_A$, where $K_{(J_{Diff})^2}$ related to $dN_T/d\Phi_p$ by

$$K_{(J_{Diff})^2} = \left(\frac{qn_i^2}{N_D}\sqrt{D}\right)^2 \sigma v_{th}\frac{dN_T}{d\Phi_p}. \tag{5.9}$$

J_D of a non-ideal nBn is considered next. If a depletion width W exists in the detector's narrow gap layer, due either to the detector's design or from operating at a slightly higher than intended reverse bias voltage, then a generation-limited dark current density component J_G, given by

$$J_G = \frac{qn_i W}{\tau_G}, \tag{5.10}$$

will also be present. [37] For J_G, changes to the generation time τ_G with Φ_p must now be considered. To first approximation, for a single active trap level, τ_G is related to τ_R

according to

$$\frac{\tau_G}{\tau_R} = \exp\left(\frac{|E_T - E_i|}{k_B T}\right), \tag{5.11}$$

where E_T is the trap energy level, E_i is the intrinsic Fermi level, k_B is the Boltzmann's constant and T is the temperature. Equation 5.11 expresses how $\tau_G \geq \tau_R$, depending on the trap level position, and that the generation process is most efficient for mid-gap trap levels ($\tau_G = \tau_R$). From equation 5.10 and 5.11, the dark current density damage factor K_{J_G} is now related to $dN_T/d\Phi_p$ by

$$K_{J_G} = qn_i W \exp\left(-\frac{|E_T - E_i|}{k_B T}\right) \sigma v_{th} \frac{dN_T}{d\Phi_p}. \tag{5.12}$$

Depending on the detector design, trap-assisted tunneling dark current J_{TAT} may also play some role, although it tends to really manifest at even higher reverse V_B than where J_G becomes prominent, well beyond the typically normal operating V_B of the detector. J_{TAT} is directly dependent on N_T so it would also be expected to increase linearly with Φ_p, while band-to-band tunneling current J_{BTB} is expected to remain independent of N_T. Thus, any changes in the tunneling-dominated region of the dark-current I-V relationship may be indicative of increasing J_{TAT}.

Comparing expressions 5.7, 5.9, and 5.12 indicates that K_J is related to the fundamental rad-tolerance of the detectors' material and design via the $dN_T/d\Phi_p$ term in each. However, these expressions also indicate that the coefficients of $dN_T/d\Phi_p$ (i.e. $qn_i^2 L_A/N_D$ in equation 5.7) are also defined by the detectors' materials and design and thus will vary too. An inspection of these expressions suggests that by finding the empirical

relationship between K_J and $(\lambda_c T)^{-1}$ one might begin to account for the presence of n_i in the coefficients of $d\mathrm{N}_T/d\Phi_p$ in each, which otherwise would simply make detectors with shorter λ_c or lower T appear more rad-tolerant since $n_i \propto \exp(-E_{gap}/2kT)$, where the bandgap $E_{gap} \cong 1.24/\lambda_c$. Additionally, if the empirical relationship holds strongly enough then it will be possible for the dark current limiting-mechanism during irradiation to be identified due to the different n_i-dependencies in (8) and (13). An analysis based on this was performed for these detectors' K_J's, as detailed in section IV below.

Finally, while J_D versus Φ_p while examined by others, these reports neglected to describe K_J's dependence on V_B. [38, 40] The expressions above qualitatively predict this behavior. K_J's dependence on V_B results from the different mechanisms becoming more or less dominant of J_D as V_B increases. For ideal detector operation at smaller V_B, $J_D \sim J_{Diff}$ and should thus increase linearly with Φ_p, roll-over as L_D becomes smaller than L_A and then follow a $\sqrt{\Phi_p}$-dependence, based on equation 5.7 and 5.9. As reverse bias increases the role of J_G will become larger, making J_D more linearly-dependent on Φ_p across the entire fluence range, based on equation 5.12 and the discussion on J_{TAT}.

This transition from $L_D \gg L_A$ to $L_D \ll L_A$ regimes at lower V_B regime was observed (see Fig. 5 in [5J]), but never routinely during the course of these experiments. Often, the authors here observed that only one or the other behavior was present or that J_D had slightly weaker dependence than $\sqrt{\Phi_p}$, the source of which is unknown. As the expressions above are strictly for the bulk 1-D case and for ideal limits, the differences in the expected and

observed behavior may be in part attributable to a reduction of 3-D collection volume and to different dark-current mechanisms manifesting simultaneously. Ionization damage was not suspected to have played a role, however, as during each of the experiments the detectors were held at 300 K for several days following proton irradiation and their I-V relationships after this multi-day anneal were still very similar to the I-V relationships taken directly post-irradiation. Ionization damage is expected to fully anneal so if it had occurred then a much larger difference would likely have been observed.

5.5   Lateral Optical Collection Length Damage Factor

As described in [42], L_{oc} is expected to be roughly proportional to L_D, however, their relationship is not specifically linear. L_{oc} is also known to be dependent on the absorption coefficient, device geometry, and surface recombination velocity. However, a closed form analytic expression for L_{oc}, that reflects all these dependencies, does not exist, which limits the possible analysis of $dL_{oc}/d\Phi_p$. Intuitively, of all the possible dependencies it is likely that only $dL_D/d\Phi_p$ is non-zero and an analysis of L_D's Φ_p-dependence follows below. However, it is also likely the other dependencies will still influence the value of the lateral optical collection length damage factor K_{1/L_{oc}^2} by factoring into the would-be coefficients of $dN_T/d\Phi_p$, similar to what occurs in equations 5.7, 5.9, and 5.12 for K_J.

L_D is related to τ_R again according to $L_D = \sqrt{D\tau_R}$. The mobility is assumed not to change significantly for the proton fluence ranges examined here ($\Phi_p < 10^{12} \, cm^{-2}$), given that the transport is typically dominated by ionized impurity scattering and the doping

concentrations will be significantly higher than the expected defect concentrations. Considering these assumptions and based on equation 5.4, L_D's dependence on Φ_p is expected to be given by

$$\frac{1}{L_D^2} = \frac{1}{L_{D0}^2} + K_{1/L_D^2}\Phi_p, \tag{5.13}$$

where K_{1/L_D^2} is the lateral diffusion length damage factor. [38] Comparing equation 5.13 to 5.4, it follows that

$$K_{1/L_D^2} = \frac{\sigma v_{th}}{D}\frac{dN_T}{d\Phi_p} = \frac{q\sigma}{\mu}\sqrt{\frac{3}{k_B T m^*}}\frac{dN_T}{d\Phi_p}. \tag{5.14}$$

Thus, K_{1/L_D^2} will be dependent on each material's $dN_T/d\Phi_p$ as well as several coefficients, all with varying dependencies.

Regarding K_{1/L_{oc}^2}, a similar expression to equation 5.13 can be applied since a linear dependence between $1/L_{oc}^2$ and Φ_p was routinely observed in the rad-tolerance experiments referred to herein. The question that remained was how closely does K_{1/L_{oc}^2} resembles K_{1/L_D^2}. Intuitively this depends on how closely L_{oc} resembles L_D relative to the other factors (i.e. absorption, device geometry, etc.) which determine it. If K_{1/L_{oc}^2} were completely dominated by changes in K_{1/L_D^2} for different devices and assuming $L_D \propto CL_{oc}$, which is roughly true based on the data in [41], then $K_{1/L_{oc}^2} = C^2 K_{1/L_D^2}$. Comparing this with equation 5.14 implies that K_{1/L_{oc}^2} should also have some kind of T-dependence due solely to the coefficients of $dN_T/d\Phi_p$. As T varies so too will λ_C vary, and thus, analogous to K_J, it is worthwhile to find the empirical relationship between

K_{1/L_{oc}^2} and $(\lambda_c T)^{-1}$. Furthermore, the empirical relationship between K_J and K_{1/L_{oc}^2} may also be of value since the previous discussion implied they may be related to each other. For example, if K_J is given by equation 5.7 then

$$K_J = \frac{q n_i^2 L_A D}{N_D C^2} \; K_{1/L_{oc}^2}. \tag{5.15}$$

5.6   Quantum Efficiency Damage Factor

The degradation rate for η also does not lend itself to a strictly analytical solution for the damage factor, even in the limiting cases. A reasonable equation for η of an ideal unipolar barrier detector, where absorption occurs in the quasi-neutral region and photo-generated carriers are collected by diffusion, is given by

$$\eta = \left(\frac{\alpha L_D}{\alpha^2 L_D{}^2 - 1}\right) \times \left[\frac{\alpha L_D - \exp(-\alpha L_A)\sinh(L_A/L_D)}{\cosh(L_A/L_D)} - \alpha L_D \exp(-\alpha L_A)\right], \tag{5.16}$$

where α is the absorption coefficient of the narrowband layer. [40] Since this expression does not easily reduce to a function of $1/\tau_R$, like J_D, some modeling was performed to examine the expected behavior.
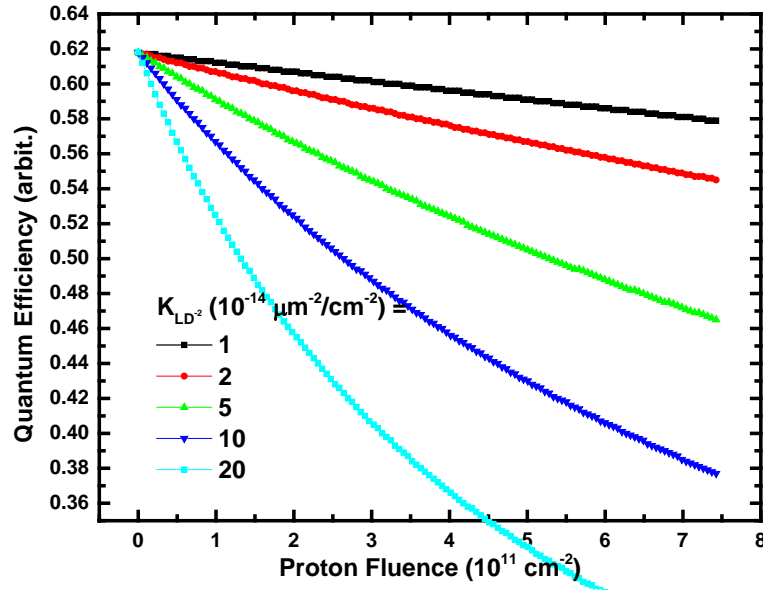
Fig. 5.1: Example plots of η using equation 5.15 as a function of Φ_p while varying $K_{L_D^{-2}}$ and arbitrarily setting $\alpha = 2 \times 10^3 \text{cm}^{-3}$. The range and values for L_D, and L_A were then chosen to roughly approximate the degradation observed in the experiments reviewed herein.

The results of the modeling are shown in Figure 5.1 where equation 5.15 is plotted for

varying K_{1/L_D^2} and nominal values of the other parameters which nearly approximate the

experimental results. The main apparent trend is the nearly-exponential decay of η with

increasing Φ_p, which appears roughly linear for smaller K_{1/L_D^2} and Φ_p. The plots show

less exponential-like decay of η as K_{1/L_D^2} decreases and the rate of decay, for linear

regions, appears to increase with increasing K_{1/L_D^2}. Plots of equation 5.15 for varying α

(not shown) did not show significant changes in the rates of decay compared with similar

changes in K_{1/L_D^2}.

Based on this modeling, and the experimental data which showed similar results, clearly

care must be taken when attempting to apply the standard damage factor analysis routine

to measurements of η such that the decay remains fairly linear across the fitting range. In

the experiments referred to herein a roughly linear, negative dependence of η on Φ_p was always observed over some range. Thus, analogous to [39], η is assumed to linearly decrease with Φ_p according to

$$\eta = \eta_0 - K_\eta \Phi_p \tag{5.17}$$

where K_η is the damage factor that is assumed to be positive.

Given K_η's expected direct proportionality to K_{1/L_D^2}, which is apparent in Figure 5.1, and K_{1/L_D^2}'s dependence on $dN_T/d\Phi_p$, given in equation 5.14, it is clear that K_η must also have a direct proportionality with $dN_T/d\Phi_p$. It will also thus likely have a dependence on similar coefficients of $dN_T/d\Phi_p$ as in 5.14. Therefore, an analogous argument to the one for determining the empirical relationship between K_{1/L_{oc}^2} and $(\lambda_c T)^{-1}$ can be made here for K_η and $(\lambda_c T)^{-1}$. Additionally, it was also expected that $K_\eta \propto K_J$ since both are expected to be proportional to $dN_T/d\Phi_p$. Demonstrating this proportionality is significant since it indicates that faster degradation of the signal for these detectors would always be accompanied by a faster increase in noise source for these detectors.

5.7 Aggregate Damage Factor Results and Analysis

In this section, data from all the rad-tolerance experiments performed on III-V-based, Ga-free, unipolar barrier detectors is plotted and analyzed based on the theory and modeling described in the previous sections. First, K_J's at low bias from each rad-tolerance experiment were semi-log plotted in Figure 5.3 versus $(\lambda_c T)^{-1}$ to determine their empirical relationship, as suggested in section 5.1.4. The results showed a robust exponential decay of K_J, over 5 orders of magnitude, with increasing $(\lambda_c T)^{-1}$. The

relationship is tight enough that a linear fit could be performed to determine the exponential decay constant, which ideally determines the n_i-dependence of K_J. According to equations 5.7 and 5.12 from section III.B above, this is either $n_i{}^2$ or n_i, respectively. The solid, least-squares fitting line, from which a slope $\sim 1.24/k_B$ was determined, indicated that K_J was proportional to $n_i{}^2 \sim E_{gap}/kT$. The dotted line with slope $E_{gap}/2kT$ was added for comparison.
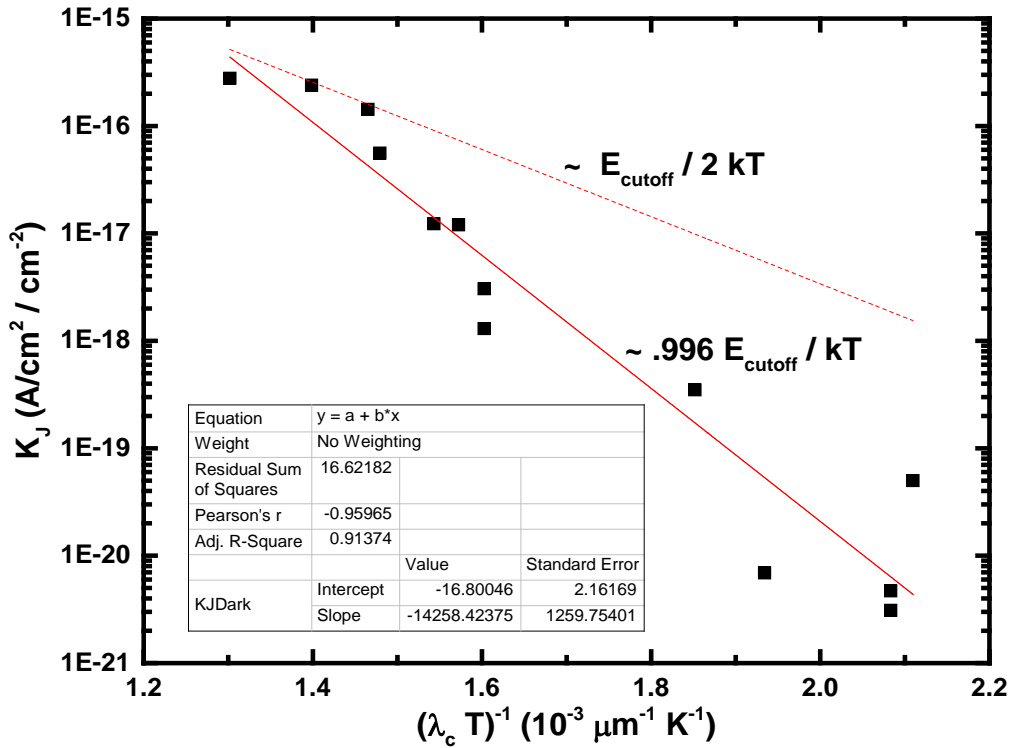
Fig. 5.2: Plot of K_J versus $(\lambda_c T)^{-1}$ taken from several rad-tolerance experiments on III-V unipolar barrier detectors. Solid line indicates an $n_i{}^2 \sim E_{cutoff}/kT$- dependence, while dotted line reflects n_i-dependence. Inset details the fit parameters and quality.

These results thus indicate K_J's behavior is well described by equation 5.7 for unipolar barrier detectors. This supports two immediate conclusions: (1) the measured increase in J_D with increasing Φ_p can be well explained by a reduction in τ_R due to displacement

damage; and (2), J_D remained diffusion-limited during proton irradiation. The latter was also concluded from the activation energies E_A determined by Arrhenius-analysis of temperature-dependent I-Vs taken on the detectors directly following irradiation, where in all cases $E_A \sim E_{gap}$ was found (e.g. see [39]). Thus, there was agreement between two different experiments that confirmed that unipolar barrier detectors remain diffusion-limited with proton irradiation despite showing an overall increase in J_D.

Figure 5.2 and equation 5.7 also indicate that detectors' rad-tolerance cannot be simply compared using their K_J's alone as detectors with larger $(\lambda_c T)^{-1}$ will automatically appear more rad-tolerant. However, the empirical relationship here (see Fig. 2 inset) can serve as heuristic for rad-tolerance comparisons. Finally, the data does not indicate $dN_T/d\Phi_p$ is constant for these detectors, only that its influence is much smaller than the n_i-dependence and that it does not depend directly on n_i itself. The scatter in the data above may equally reflect differences in $dN_T/d\Phi_p$ or its coefficients in equation 5.7 (e.g. N_D, L_A, etc.).
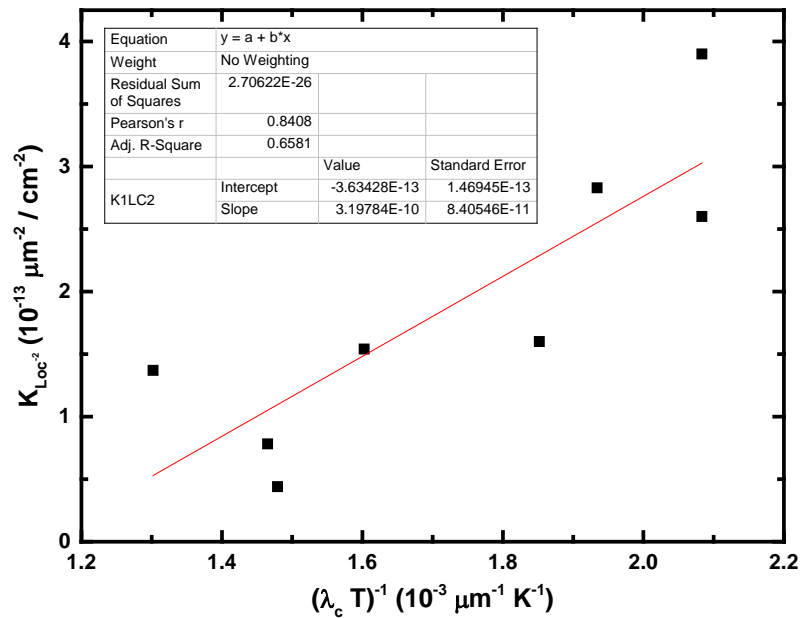
Fig. 5.3: Plot of $K_{L_{oc}^{-2}}$ versus $(\lambda_c T)^{-1}$ from the same rad-tolerance experiments as Fig. 1. Inset details the fit parameters and quality.

A plot of K_{1/L_{oc}^2} versus $(\lambda_c T)^{-1}$, which was suggested by arguments previously covered, is shown in Figure 5.3. The dataset here is slightly smaller as some detectors did not have measurable L_{oc} by design; equation (1) remains valid for these detectors despite this. The results in Figure 5.3 indicated that empirically K_{1/L_{oc}^2} had a roughly linear dependence on $(\lambda_c T)^{-1}$. The relationship implies that detectors were effectively less rad-tolerant at higher $(\lambda_c T)^{-1}$, which was opposite of what was observed for K_J in Figure 5.2. This was also opposite of the behavior found for K_{1/L_D^2} in III-V solar cells by [42], which predicts it increases with increasing $(\lambda_c T)^{-1}$. This difference can only be explained by the influence of the coefficients of $dN_T/d\Phi_p$ in its relationships with K_J and K_{1/L_{oc}^2}, which must dominate any variation of it due to materials and designs. This conclusion is also buoyed by the observation of a linear change in $1/L_{oc}^2$ with increasing Φ_p for every detector characterized with a measurable L_{oc}. This strictly linear behavior, predicted in 5.1.5, clearly indicated a reduction in τ_R occurred with proton irradiation, which is the same mechanism the increase in J_D with increasing Φ_p was attributed to. [39] Finally, Figure 5.3 again shows that while K_{1/L_{oc}^2}'s alone are not effective for comparing rad-tolerances, the empirical relationship serves as another heuristic for comparisons.
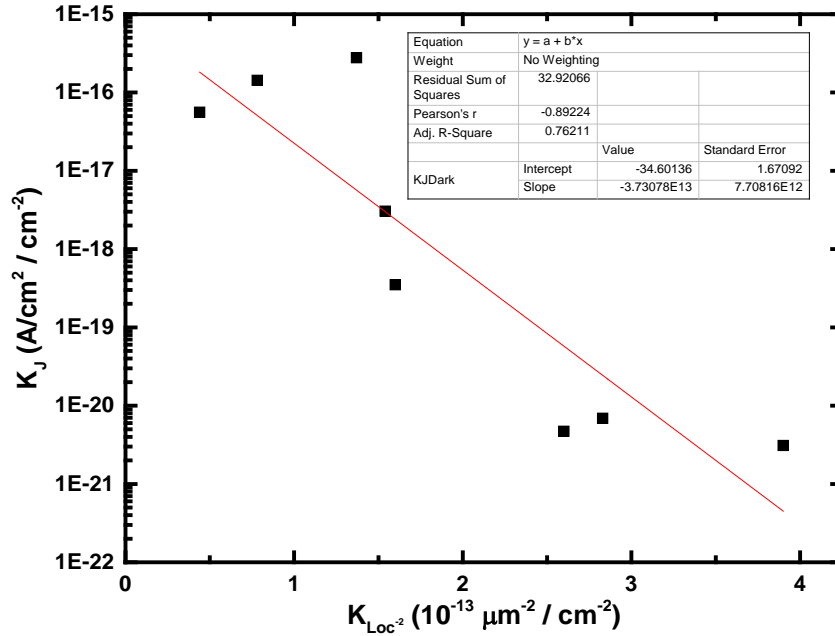
Fig. 5.4: Plot of K_J vs. $K_{L_{oc}^{-2}}$ from the same rad-tolerance experiments as Figure 5.1. Inset details the fit parameters and quality.

Directly plotting the empirical relationship between K_J and K_{1/L_{oc}^2}, shown in Figure 5.4, naturally demonstrates a negative, exponential dependence. This relationship was expected based on the results in Figure 5.2, the linear relationship between K_J and K_{1/L_{oc}^2} given in equation 5.15, and Figure 5.3, which showed K_{1/L_{oc}^2} was roughly linearly related to $(\lambda_c T)^{-1}$. The fit quality here is diminished now compared with Figure 5.2 (see insets), which reflects the additional measurement uncertainty.

In Figure 5.5 K_η's from these experiments are all plotted versus $(\lambda_c T)^{-1}$, as suggested in section 5.1.6. Here, a robust trend was again observed, while a linear fitting with a negative slope demonstrated the best fit quality overall. Similar and opposite of the result in Figures 5.2 and 5.3, respectively, the empirical relationship between K_η and $(\lambda_c T)^{-1}$ indicates

detectors with larger $(\lambda_c T)^{-1}$ will always appear more rad-tolerant in comparisons of K_η's alone, rendering those comparisons invalid. The fitting parameters in the inset of Figure 5.5, however, provide another heuristic with which valid comparisons of the rad-tolerance of detector's η can actually be made. Plotting the measured K_η versus K_{1/L_{oc}^2} (not shown) did not shed much additional light here as Figures 5.3 and 5.5 show they are both linearly related to $(\lambda_c T)^{-1}$.

The appearance of positive and negative slopes in K_η's and K_{1/L_{oc}^2}'s empirical relationships with $(\lambda_c T)^{-1}$ in Figs. 3 and 5, respectively, is striking considering the modeling results from Figure 5.1, which clearly predicted a faster degradation rate for η with larger K_{1/L_D^2}, and the strong likelihood that K_{1/L_{oc}^2} was linearly related to K_{1/L_D^2} discussed in section 5.1.5. This difference thus further implies both K_η and K_{1/L_{oc}^2}'s dependence on $dN_T/d\Phi_p$ must be dominated by other dependencies. This adds further weight to the argument that K_η and K_{1/L_{oc}^2} cannot be used independent of the heuristics provided by the empirical relationships to compare the rad-tolerance of unipolar barrier detectors. Plotting K_η versus K_J (not shown) demonstrated a clear proportionality existed between them, which was expected given the direct proportionality of both K_η and K_J with $(\lambda_c T)^{-1}$ in Figures 5.5 and 5.2, respectively.
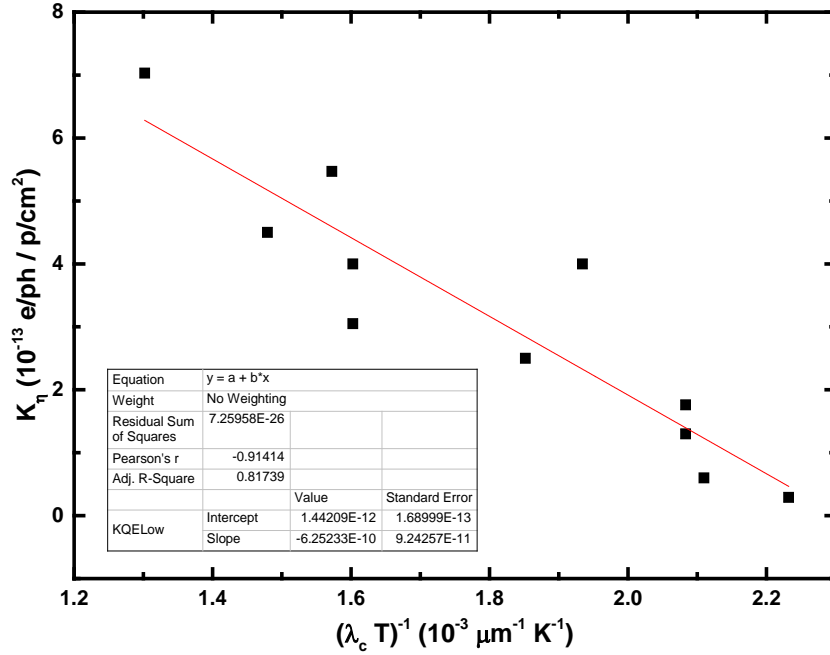
Fig. 5.5: Plot of K_η versus $(\lambda_c T)^{-1}$ for the same rad-tolerance experiments as Figure 5.1. Inset details the fit parameters and quality.

5.8　　Conclusions Aggregate Damage Factor Results and Analysis

The results from a series of radiation tolerance experiments on III-V unipolar barrier infrared detectors of various designs, λ_c's, and operating T's were examined. The results led to empirical relationships between the measured radiation damage factors, $K_{L_{oc}^{-2}}$, K_J, and K_{QE}, and $(\lambda_c T)^{-1}$. Fitting K_J's empirical relationship indicated displacement damage and subsequent reduction in τ_R was the source of increasing dark current with 63 MeV proton irradiation and that J_D remained diffusion-limited during irradiation. This was confirmed by an Arrhenius-analysis of temperature-dependent, post-irradiation IV measurements of all the detectors as shown in Chapter 4. The existence of these empirical

relationships disqualifies comparisons of detector rad-tolerance based on their damage factors alone. Rather, the empirical relationships provide new heuristics, with which rad-tolerance comparisons may be performed. The empirical relationships, especially the difference between the sign of the slope in Figures 5.3 and 5.5, also collectively indicated that the damage factors' dependence on $dN_T/d\Phi_p$ was likely dominated by its dependence on other factors. This does not imply $dN_T/d\Phi_p$ was constant for all these detectors, only that it exerts a weaker influence on the radiation damage factors than other dependencies. Future work is planned to directly measure τ_R using time resolved photoluminescence as a function of Φ_p, which may mitigate the coefficient's effects and allow for $dN_T/d\Phi_p$ of each detector to be more closely examined.

6 Discussion, Conclusions, and Future Direction of Research

In this research it was found that rate of degradation in quantum efficiency when irradiated with 63 MeV protons for a family of Sb-based MWIR detectors that employed unipolar barrier architectures was >x3 than that of conventional p-on-n HgCdTe photodiodes with similar cut-off wavelengths. Likewise it was found that the rate of degradation in the lateral optical collection length for these same devices was >x20 than equivalent MWIR HgCdTe photodiodes. The impact of passivation or lack thereof for Sb-based nBn detectors was found to be a minimal issue. The surfaces tend to be pinned such that they are n-type and the barrier in the nBn or alike unipolar barrier architecture detector bocks the majority surface current to a very large degree. This was confirmed in the Co-60 characterization that was performed as part of this research and other characterization that author is aware of. [12] Changes in the P/A behavior for the dark current are likely indicating an increase in the lateral diffusion dark current. The said diffusion current increases as L_D decreases with proton irradiation. This is because L_D is really a measure of how fast the minority carrier density concentration varies over distance. For Sb-based unipolar barrier devices with small initial L_D pre-radiation exposure it was found that the minority carrier density concentration decreases quickly and diffusion current increases.

In comparison, the amount of L_{oc} will decrease with proton irradiation such that the lateral photo-currents are also decreasing. The drop in L_D is directly contributing to a drop in photo-current because even though there are diffusion currents too they reflect a non-equilibrium condition. Specifically, there are excess electron hole pares present due to the optical excitation, whereas the dark current increase is related to an equilibrium condition.

6.1 Path Forward for Sb-based nBn and Alike MWIR Unipolar Barrier IR Detectors

In chapter 4 and 5, details on the 63 MeV proton degradation of Sb-based unipolar barrier IR detectors were discussed in detail. The degradation in QE was found to be substantial in comparison to that of the incumbent technology HgCdTe. Our research group at the Air Force Research Laboratory has been focused on mitigating these effects. Forms of mitigation include deliberately grading the absorber such that carrier are swept out and increasing the minority carrier lifetime. It has been found that while the end-of-life QE has increased J_D has drastically increased. Recently several novel designs with graded absorbers were grown, processed, and then characterized and it was found that K_{QE} and K_{LOC} were actually appreciably lower than the aggregate data and associated empirical fit as shown in Figure 6.1 and Figure 6.2 respectively. Unfortunately it was likewise found that the K_J was higher than that of other rates of degradation and aggregate value as shown in Figure 6.3.

Equation	y = a + b*x	
Weight	No Weighting	
Residual Sum of Squares	7.25958E-26	
Pearson's r	-0.91414	
Adj. R-Square	0.81739	
	Value	Standard Error
KQELow	Intercept	1.44209E-12	1.68999E-13
	Slope	-6.25233E-10	9.24257E-11

Fig. 6.1: Plot of K_η versus $(\lambda_c T)^{-1}$ for Sb-based MWIR unipolar barrier detector with graded absorber.

Slope = 3.20 □ .84 × 10^{-10} cm^2 K / μm
Intercept = -3.63 □ 1.50 × 10^{-13} μm^{-2} / cm^{-2}
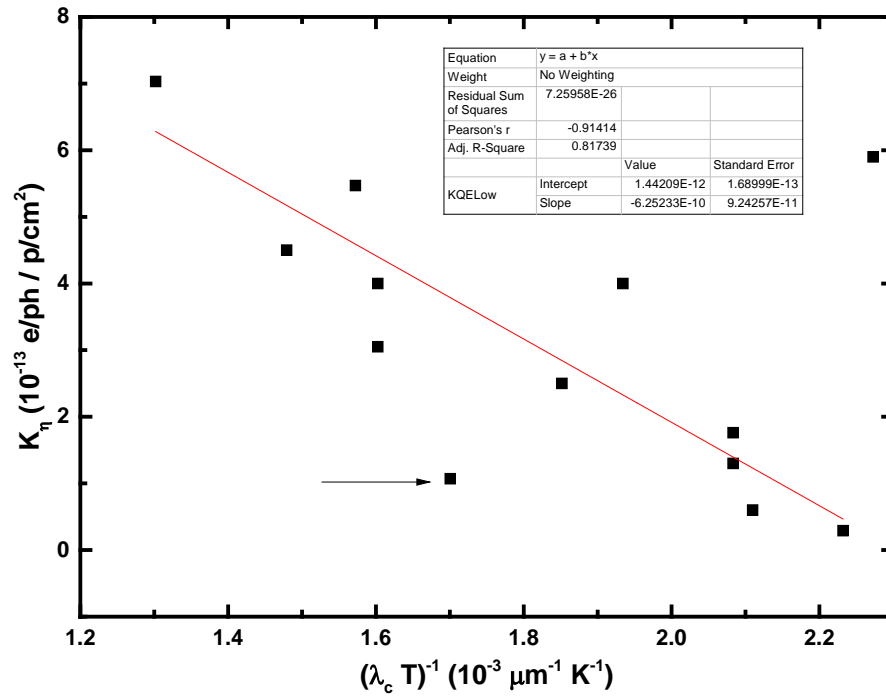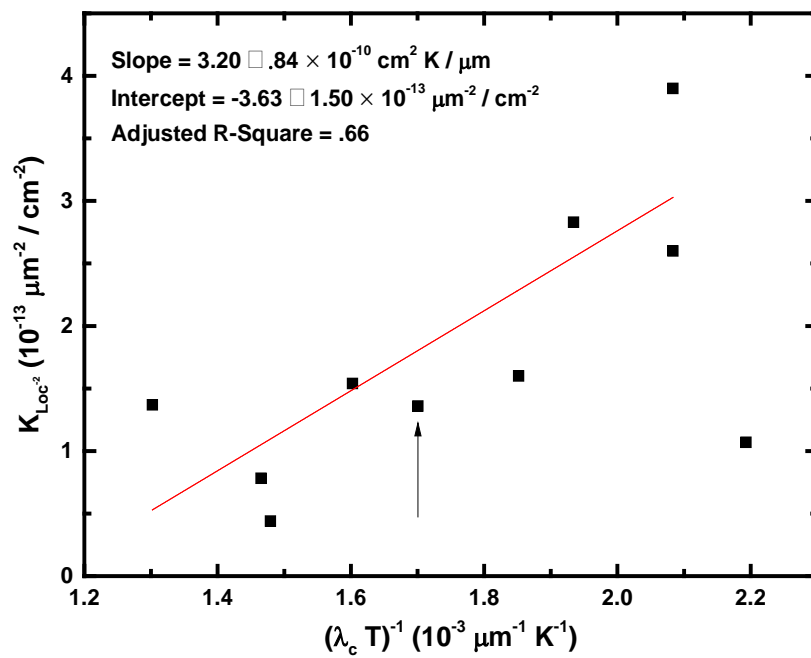Adjusted R-Square = .66

Fig. 6.2: Plot of K_{LOC} versus $(\lambda_c T)^{-1}$ for Sb-based MWIR unipolar barrier detector with graded absorber.
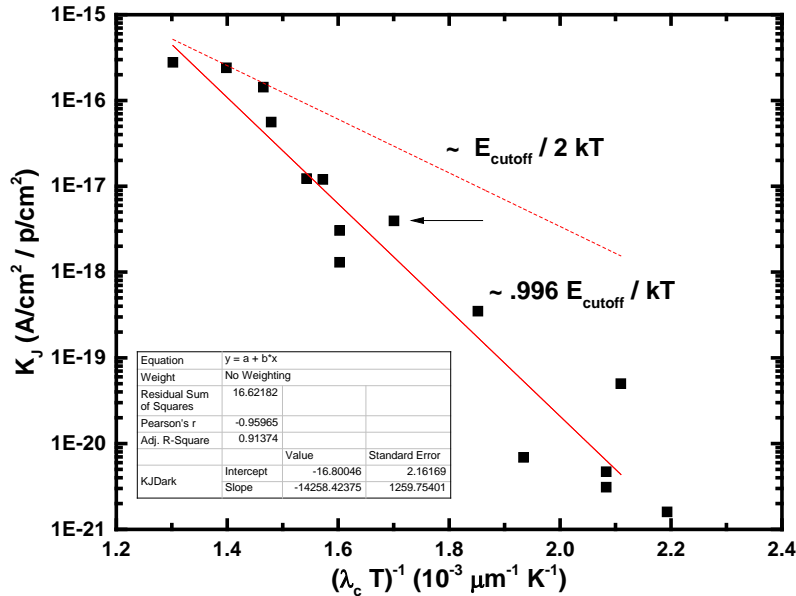
Fig. 6.3: Plot of K_J versus $(\lambda_c T)^{-1}$ for Sb-based MWIR unipolar barrier detector with graded absorber.

6.2 Future Direction

In general our research group at the Air Force Research Laboratory has access to a very unique knob namely radiation which is capable of systematically changing defect concentrations. It seems imperative given the current state of performance of Sb-based unipolar barrier IR detector technology to leverage this knob to further understand how Shockley-Read-Hall centers are changing with concentration. To date several means to try to engineer around the SRH problem have taken place while the fundamental material issue hasn't been resolved, the future of the technology is

very likely dependent on solving this problem and it will need to be addressed in future research endeavors. Additional radiometric and radiation tolerance growth-characterization campaigns will take place in hopes of driving J_D down while maintaining and potentially improving spectral QE. Improving transport within the material itself is of high interest. Time resolved photoluminescence measurements in quantity varying Sb concentrations amongst other parameters to find root cause and/or optimal recipe are already underway as this dissertation is being written. Many more studies along these lines are planned to be executed.

Now that a metric and baseline of damage factors has been established for the Sb-based unipolar barriers it will be easier for IR detector laboratories to determine if improvement in the radiation susceptibility are indeed being made. Prior to this research being completed this wouldn't of been possible

References

[1]   E. L. Dereniak and G. D. Boreman, Infrared detectors and systems: Wiley, 1996.

[2]   A. Rogalski, "Infrared detectors: an overview," Infrared Physics & Technology, vol. 43, pp. 187-210, Jun-Oct 2002.

[3]   A. Rogalski, "Infrared detectors: status and trends," Progress in Quantum Electronics, vol. 27, pp. 59-210, 2003 2003.

[4]   A. W. Hoffman, "Infrared Detectors & Systems," UCSB short course notes, 2009.

[5]   D. L. Smith and C. Mailhiot, "Proposal for strained type II superlattice infrared detectors," Journal of Applied Physics, vol. 62, pp. 2545-2548, 1987.

[6]   S. Maimon and G.W. Wicks, Applied Physics Letters, Volume 89, 151109, 2006.

[7]   E. Plis, J. B. Rodriguez, H. S. Kim, G. Bishop, Y. D. Sharma, L. R. Dawson, S. Krishna, S. J. Lee, C. E. Jones, and V. Gopal, "Type II InAs/GaSb strain layer superlattice detectors with p-on-n polarity," Applied Physics Letters, vol. 91, pp. 133512-3, 2007.

[8]   B.-M. Nguyen, D. Hoffman, Y. Wei, P.-Y. Delaunay, A. Hood, and M. Razeghi, "Very high quantum efficiency in type-II InAs/GaSb superlattice photodiode with cutoff of 12 mu m," Applied Physics Letters, vol. 90, pp. 231108-3, 2007. [8]

[9]   A. Rogalski, "Third-generation infrared photon detectors," Optical Engineering, vol. 42, pp. 3498-3516, 2003.

[10]   N. Gautam, H. S. Kim, M. N. Kutty, E. Plis, L. R. Dawson, and S. Krishna, "Performance improvement of longwave infrared photodetector based on type-II InAs/GaSb superlattices using unipolar current blocking layers," Applied Physics Letters, vol. 96, pp. 231107-3, 2010.

[11]   V. M. Cowan, C. P. Morath, J. E. Hubbs, S. Myers, E. Plis, and S. Krishna, "Radiation tolerance characterization of dual band InAs/GaSb type-II strain-

layer superlattice pBp detectors using 63 MeV protons," Appl. Phys. Lett., vol. 101, pp. 251108–251112, 2012.

[12] V. M. Cowan, C. P. Morath, S. Myers, N. Gautam, and S. Krishna, Proc. SPIE 8012, 801210 (2011).

[13] C. P. Morath, V. M. Cowan, L. A. Treider, G. D. Jenkins, and J. E. Hubbs, "Proton Irradiation Effects on the Performance of III-V-Based Unipolar Barrier Infrared Detectors, IEEE TNS., VOL. 62, NO. 2, April 2015.

[14] E. Plis, S. Annamalai, K. T. Posani, S. Krishna, R. A. Rupani, and S. Ghosh, J. Appl. Phys. 100, 014510 (2006).

[15] B.-M. Nguyen, S. Bogdanov, S. Abdollahi Pour, and M. Razeghi, Appl. Phys. Lett. 95, 183502 (2009).

[16] A. Soibel, D. Ting, C. Hill, M. Lee, J. Nguyen, S. Keo, J. Mumolo and S. Gunapala, Appl. Phys. Lett. 96, 111102 (2010).

[17] J. E. Hubbs, D. C. Arrington, M. E. Grammer, and G. A. Dole, Opt. Eng. (Bellingham) 39, 2660 (2000).

[18] B. J. Klemme, C. P. Morath and D. T. Le, "Low-temperature noise measurements on quantum well infrared photodetectors", Proc. SPIE 5111, 162 (2003).

[19] V. M. Cowan, C. P. Morath, S. Myers, N. Gautam, and S. Krishna Low-temperature noise measurements of an InAs/GaSb-based nBn MWIR detector", Proc. SPIE 8012, Infrared Technology and Applications XXXVII, 801210 (May 20, 2011)

[20] C. M. Castaneda, "Crocker nuclear laboratory (CNL) radiation effects measurement and test facility," in Proc. IEEE Radiation Effects Data Workshop, 2001, pp. 77–81.

[21] W. E. Tennant, D. Lee, M. Zandian, E. Piquette, and M. Carmody, J. Electron. Matter. 37, 1406 (2008).

[22] G. P. Jenkins, C. P. Morath and V. M. Cowan, "An Empirical Study of the Disparity in Rad-tolerance of the Minority Carrier Lifetime between II-VI and III-V Space-Detector Technologies in the MWIR" (to be published, Journal of electronic materials).

[23] V. M Cowan, C. M. Morath, S. M. Swift, P. D. LeVan ; S. Myers, et al. "Electrical and optical characterization of InAs/GaSb-based nBn IR detector", Proc. SPIE 7780, Detectors and Imaging Devices: Infrared, Focal Plane, Single Photon, 778006 (August 26, 2010).

[24] V. M Cowan, C. M. Morath, InAs/GaSb-based nBn MWIR Detector Noise Measurements, 2012 International workshop on II-VI materials, Novemeber 2012

[25]   B. D. Weaver, E. H. Aifer, "Radiation Effects in Type-Two Antimonide Superlattice Infrared Detectors," IEEE Transactions on Nuclear Science, Vol. 56, No. 6, 6, December (2009).

[26]   E.M. Jackson,   E.H. Aifer,   C.L. Candy,   J.A. Nolde,   C.D. Cress, B.D. Weaver, I. Vurgaftman, J.H. Warner, J.R. Meyer, J.G. Tischler, S.A. Shaw, and C.R. Dedianous, "Radiation damage in type-II superlattice infrared detectors," Journal of Electronic Materials, Vol. 39, No. 7, (2010).

[27]   J. H. Hubbs, V. M. Cowan personal communication April 2015 - October 2016.

[28]   C. Claeys, and E. Simoen, Radiation Effects in Advanced Semiconductor Materials and Devices, New York: NY (Springer) 2002, pp. 9-35.
[29]   B. D. Weaver, and E. H. Aifer, IEEE Trans. on Nucl. Sci 56, 3307-3309, Dec. 2009.
[30]   E. M. Jackson, and E. H. Aifer, C. L. Candy, J. A. Nolde, C. D. Cress, B. D. Weaver, I. Vurgaftman, J. Warner. J. R. Meyer, J. G. Tishchler, S. A. Shar, and C. R. Dedianous, Jour. Electon Mater. 39, 7 (2010).

[31]   J. E. Hubbs P. W. Marshall, C. J. Marshall, M. E. Gramer. D. Maestas, J. P. Garcia, G. A. Dole, and A. A. Anderson, IEEE Trans. Nucl. Sci. 54, No. 6, (2007).

[32]   E. A. Plis, S. S. Krishna, N. Gautam, S. Myers, and S. Krishna, IEEE Photonics J. 3, 234-240, April 2011.

[33]   V. M. Cowan, and C. P. Morath (unpublished).

[34]   J. Loferski and P. Rappaport, "Radiation Damage in Ge and Si Detected by Carrier Lifetime Changes: Damage Thresholds," Phys. Rev.,vol.111, no. 2, pp 432 – 439, Jul. 1958.
[35]   P. W. Marshall, J. E. Hubbs, D. C. Arrington, C. J. Marshall, R. A. Reed, G. Gee, J. C. Pickel, and R. A. Ramos, "Proton-induced transients and charge collection measurements in a LWIR HgCdTe focal plane array," IEEE Trans. Nucl. Sci., vol. 50, no. 6, pp. 1968-1973, Dec. 2003.
[36]   E. H. Steenbergen, B. C. Connelly, G. D. Metcalfe, H. Shen, W. Wraback, D. Lubyshev, Y. Qiu, J. M. Fastenau, A. W. K. Liu, S. Elhamri, O. O. Cellek, and Y. H. Zhang, "Significantly improved minority carrier lifetime observed in a long-wavelength infrared III-V type-II superlattice comprised of InAs/InAsSb," Appl. Phys. Lett., vol. 99, pp. 251110-251113, 2011.
[37]   C. Claeys and E. Simoen, Radiation Effects in Advanced Semiconductor Materials and Devices. New York: Springer, 2002.
[38]   J.J. Loferski and P. Rappaport, "Radiation Damage in Ge and Si Detected by Carrier Lifetime Changes: Damage Thresholds," Phys. Rev.,vol.111, no. 2, pp 432 – 439, Jul. 1958.
[39]   R. N. Hall, "Electron-hole recombination in Ge," Phys. Rev., vol. 87, p. 387, 1952.

[40] G. R. Savich, D. E. Sidor, X. Du, M. Jain, C. P. Morath, V. M. Cowan, J. K. Kim, J. F. Klem, D. Leonhardt, S. D. Hawkins, T. R. Fortune, A. Tauke-Pedretti, and G. W. Wicks, "Defect related dark currents in III-V MWIR nBn detectors," in Proc. SPIE, 2014, p. 907011.

[41] M. H. Weiler and G. J. Tranowski, "Characterization of HgCdTe p-on-n heterojunction photodiodes and their defects using variable area test structures," J. Electron. Mater., vol. 26, pp. 635–642, 1997.

[42] F. Van de Wiele, "Photodiode quantum efficiency," in Proc. NATO Advanced Study Institute on Solid State Imaging, Louvain-la-Neuve, Belgium, 1975, pp. 47–90.

[43] J. E. Hubbs, C. P. Morath, and V. M. Cowan, "Comparison of the proton radiation response of HgCdTe focal plane array technologies to a III-V nBn MWIR focal plane array," in Proc. MSS, 2014.

[44] C. P. Morath, E. A. Garduno, V. M. Cowan, G. D. Jenkins, "More Accurate Quantum Efficiency Damage Factor for 63 MeV Proton-Irradiated III-V Unipolar Barrier Infrared Detectors", IEEE TNS (2016)